VOLUME 3 ISSUE 1
25 JULY 2024

PHYSICS RESEARCH REPORTS

A Yearly Publication Of Project Reports

PG DEPARTMENT OF PHYSICS
SULLAMUSSALAM SCIENCE COLLEGE
AREEKODE

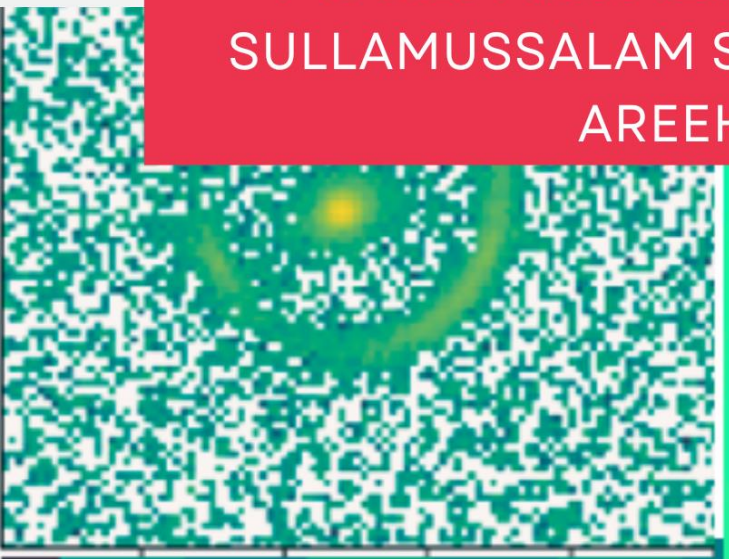

PHYSICS
RESEARCH REPORTS

A Yearly Publication of Project Reports

Editor In Chief:

Dr. Sharafali A

Editors:

Dr. Mohammed Rasi U P

Sabeel P K

PG DEPARTMENT OF PHYSICS

SULLAMUSSALAM SCIENCE COLLEGE

AREEKODE

PHYSICS RESEARCH REPORTS

A Yearly Publication of Project Reports

© **Publication Division**

Sullamussalam Science College
Ugrapuram P.O, Areekode, Malappuram,
Kerala, India – 673639
Email: mail@sscollege.ac.in

Layout: Dr. Mohammed Rasi U P

PREFACE

It is with great pleasure that I present the latest edition of *Physics Research Reports*, the annual compilation of outstanding M.Sc. physics projects. This publication is a testament to the dedication, ingenuity, and intellectual curiosity of our students, who have ventured into diverse realms of physics to explore, experiment, and contribute to the scientific community.

The projects featured in this volume reflect the breadth and depth of contemporary physics research. From theoretical investigations to experimental breakthroughs, each report encapsulates a unique journey of scientific discovery. These endeavours not only demonstrate the students' mastery of complex concepts and methodologies but also highlight their ability to tackle real-world problems through innovative solutions.

This year's edition includes an impressive array of topics, ranging from condensed matter physics and non-linear optics to astrophysics and applied material science. Notably, there is a growing interest in interdisciplinary research, where students have skilfully integrated principles from various scientific domains to address multifaceted challenges. This trend underscores the dynamic nature of modern physics and the importance of collaborative efforts in advancing our understanding of the universe.

The compilation of these research reports is a collaborative effort. I extend my heartfelt gratitude to the faculty members who have mentored and guided the students throughout their research journeys. Their unwavering support and expertise have been instrumental in shaping the scientific rigor and quality of these projects. Additionally, I acknowledge the invaluable contributions of the reviewers and editorial team, whose meticulous work has ensured the high standards of this publication.

As you delve into the pages of *Physics Research Reports*, I hope you find inspiration in the innovative ideas and discoveries presented by our talented students. These reports are not just academic exercises; they are the seeds of future advancements in science and technology. It is my firm belief that the insights and knowledge shared in this volume will pave the way for new avenues of research and ignite the spark of curiosity in the next generation of physicists.

Finally, I encourage our readers to engage with these projects, provide feedback, and foster a vibrant scientific discourse. The pursuit of knowledge is a continuous journey, and through collaborative efforts, we can collectively push the boundaries of what is known and achieve new milestones in the fascinating world of physics.

Thank you for your continued support and interest in our annual publication.

Sincerely,

Dr. Sharafali A
Editor, *Physics Research Reports*

Table of Contents

Physics Research Reports (2024), **3–1**

PHYSICAL SCIENCE RESEARCH RESULTS

V-parameter and confinement loss in Void-filled photonic crystal fiber

Ashfina CT[1] and Sharafali A[*,2]

[1]Department of Physics, Sullamussalam Science College, Areekode, Kerala, India 673639
[2]Department of Physics, Sullamussalam Science College, Areekode, Kerala, India 673639
[*]Corresponding author. Email: sharaf.saj@sscollege.ac.in

Abstract

The specialized nature and potential applications of Photonic Crystal Fibers (PCFs) have led to extensive research in the past decade. PCFs possess a variety of distinctive capabilities which are achieved by modifying the structure of the PCF, allowing for easy manipulation of the optical properties of the guided modes.In this project we introduced a new design of soild core hexagonal PCF called as Void-Filled Photonic Crystal Fiber(VFPCF) and it's characteristics confinement loss and V-parameter are studied. Through confinement loss study we determined improved design of VFPCF and V-parameter characteristics study determined suitable Λ/λ ratio for single mode VFPCF of fixed air hole diameter and pitch for different void air hole diameters. Proposed model can propagating pulses with minimum powerloss and it is suitable for communication purpose.

Keywords: Photonic crystal fiber,Confinement loss,V-parameter,Void filled photonic crystal fiber,COMSOL,Modelling

Introduction

Fiber optics has become an indispensable aspect of our daily lives, in communication systems, possess diverse applications in fields such as medicine, engineering, robotics, and sensing. These slender and transparent strands, composed of either glass or plastic, efficiently guide light through the principle of total internal reflection, a phenomenon initially demonstrated by John Tyndall. The contributions of Charles K. Kao and George Hockham led to significant advancements in reducing fiber attenuation to 20 dB/km, thereby enhancing their utilization in the realm of communications[1]

In 1996, Philip Russell introduced photonic crystal fibers (PCFs), which exhibit distinct structural and property disparities when compared to conventional fibers. Initially consisting of a solid core, PCFs have evolved to encompass hollow-core variants as well as other types such as single-mode and multimode fibers. These PCFs find applications in mode filtering, sensors, interferometry, and fiber lasers. Noteworthy properties of PCFs include the V-parameter, dispersion, numerical aperture, confinement loss, and spot size. Here study focuses on a hexagonal silica-based PCF, specifically examining the effects of different air hole diameters on confinement loss and the V-parameter.

Optical fiber

In 1966, Charles Kao and George Hockham introduced fiber optics for data transmission using light pulses[2].These flexible glass or plastic cables, used in communication, illumination, imaging, sensors, and lasers, consist of a light-guiding core surrounded by cladding for efficient transmission through total internal reflection, and a protective jacket.

Optical fibers are categorized by modes (single-mode for long distances, multimode for short distances) and refractive index (step-index with constant refractive index, graded-index with decreasing refractive index). Glass fibers are preferred for their durability. Fiber optics have revolutionized many fields.

Photonic cryatal fiber

Photonic Crystal Fibers (PCFs), introduced in 1995, are specialized optical fibers with a periodic arrangement of low-index materials (typically air holes) in a high-index background [3]. Pioneered by Russell and colleagues, PCFs offer superior performance over traditional optical fibers, with low confinement loss, high sensitivity, and customizable dispersion. Advances in fabrication have led to various PCF structures, such as hexagonal, triangular, circular, square, octagonal, hybrid, decagonal, and honeycomb designs, each optimized for specific applications by adjusting lattice pitch and hole diameter[4]

PCFs use two guiding mechanisms: index-guiding (modified total internal reflection within a solid core) and photonic bandgap guidance (light confinement within a low-index core using cladding with different refractive indices). This dual capability provides PCFs with enhanced versatility, greater design flexibility, and superior nonlinear properties. PCFs are used in high-power delivery, ultra-wideband transmission, sensing, and more.

Confinement loss in photonic crystal fibers (PCFs) is a result of the fiber's imperfect construction and the leaky nature of the modes, which is influenced by the arrangement of air holes within the fiber. The reduction of this loss occurs when the core size is small and surrounded by a minimum of six rings of air holes. The

confinement loss can be calculated using the equation[5]

$$\text{Confinement loss} = \left(\frac{2\pi}{\lambda}\right) \cdot 8.686 \cdot Im(n_{\text{eff}}), \tag{1}$$

where (λ) represents the wavelength and $Im(n_{\text{eff}})$ denotes the imaginary part of the effective mode index.

The V-parameter, also known as the normalized frequency parameter, plays a crucial role in determining the number of modes that a fiber can support. In the case of PCFs, this parameter is adjusted due to their unique structure and can be expressed as shown in equation2,

$$V = 2\pi \left(\frac{\Lambda}{\lambda}\right) \sqrt{n_{\text{FM}}^2 - n_{\text{FSM}}^2}. \tag{2}$$

Here, Λ represents the pitch, λ denotes the wavelength, n_{FM} signifies the effective refractive index of the fundamental mode, and n_{FSM} represents the refractive index of the fundamental space filling mode. This parameter is instrumental in verifying the continuous operation of a single mode in PCFs and estimating the cut-off frequency for the second-order mode. It provides a single-mode cut-off value of π[5]

Void filled photonic crystal fiber

To design and model photonic crystal fibers (PCFs) using COMSOL Multiphysics version 5.5, the process starts by creating the geometry of the fiber with air holes by defining circles with the necessary parameters such as radius and pitch. The material properties, specifically the refractive indices of silica and air, are then assigned to the model. Using the Finite Element Method (FEM)[6], the fiber's modes are analyzed by solving Maxwell's equations with appropriate boundary conditions. The fundamental mode is identified based on the highest effective mode index, and the confinement loss is calculated by considering the imaginary part of the effective refractive index. The V-parameter, essential for understanding mode confinement and guiding properties, is also calculated by determining the effective refractive indices of the fundamental mode and the fundamental space-filling mode. This comprehensive modeling approach ensures accurate simulation and analysis of PCF characteristics such as confinement loss and mode distribution.

In order to minimize the loss of confinement in photonic crystal fibers (PCFs), the voids between the circular air holes in the solid core H-PCF are substituted with "void air holes." Initially, a single layer of these void air holes is introduced between the first and second layers of air holes that surround the silica solid core, as illustrated in Figure 1b. This particular arrangement is examined to assess its confinement

loss and V-parameter, and the results are graphed against the wavelength for a comprehensive analysis. To further enhance the performance, multiple layers of void air holes are added until all the voids between the air holes are filled, as depicted in Figure 1c. This multi-layered structure is also investigated for its confinement loss and V-parameter using MATLAB, ensuring a meticulous analysis and an optimized design for the fiber.

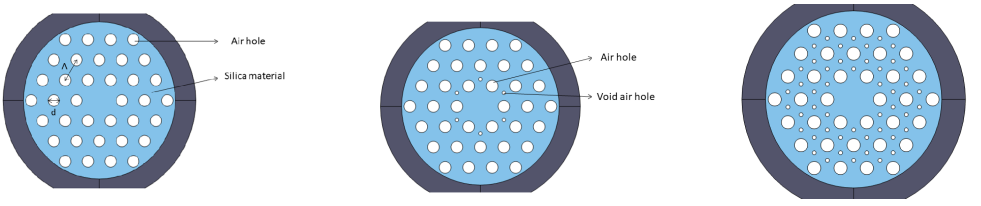

(a) Solid core hexagonal PCF **(b)** Single layer of void air holes in PCF **(c)** Void-Filled Photonic Crystal Fiber

Figure 1. Different stages of designing VFPCF

Result

The study of Void-Filled Photonic Crystal Fiber (VFPCF) shows significant reductions in confinement loss with the introduction of void air holes. Initially, confinement losses were high across various wavelengths without void air holes. Integrating a single layer of void air holes between regular air holes around the solid silica core (as shown in Figure 2a) substantially decreased confinement loss. Adding more layers of void air holes further reduced losses, reaching as low as 10^{-6} dB/m in some cases. Additionally, larger void air hole diameters generally resulted in lower losses, emphasizing the importance of design optimization. These results highlight VFPCF's potential to enhance light propagation efficiency for optical communication and sensing applications.

(a) Confinement loss variation with Void air hole layer

(b) Confinement loss with different Void air hole diameter of Air hole diameter $0.8\,\mu$m VFPCF

Figure 2. Confinement loss variation of VFPCF

In this study,We have also focused on Void-Filled Photonic Crystal Fiber (VFPCF), the V-parameter's behavior was thoroughly investigated with respect to void

air hole diameter and wavelength, maintaining a fixed pitch and air hole diameter of 0.8μm and 1.2μm respectively. The study investigated the single-mode cutoff for VFPCF, focusing on the Λ/λ ratio. Figure 3a shows the influence of different void air hole diameters (0.2μm, 0.3μm, and 0.4μm) on the single-mode cutoff point(V_{cutoff}) for VFPCF with d/Λ ratios of 0.4μm and 0.6μm. Notably, in figure 3b at a void air hole diameter of 0.4μm and d/Λ = 0.6μm, the VFPCF achieves a single-mode cutoff just above a Λ/λ ratio of 1.2, underscoring the need for precise design to optimize single-mode propagation for optical communication and sensing.

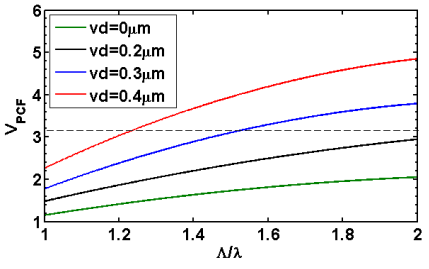

(a) V-parameter variation with d and V_{cutoff}

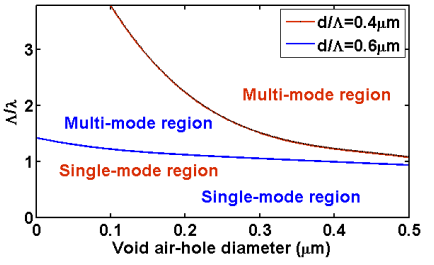

(b) Single mode and multimode Cutoff region

Figure 3. V-parameter values for VFPCF

Additionally, the study compared pulse propagation through single-mode VF-PCF and conventional single-mode PCF, demonstrating a significant reduction in power loss in VFPCF.Specifically, conventional PCF exhibited a loss of 11.5 dB/m, whereas VFPCF showed only 0.46 dB/m loss over the same distance. Figures 4a and 4b provide three-dimensional visualizations, highlighting VFPCF's superior ability to minimize pulse intensity loss compared to conventional PCF.

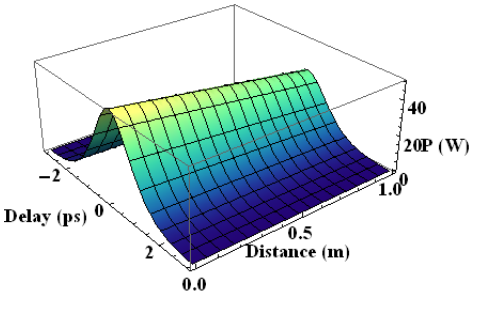

(a) Pulse propagation through single mode PCF shows in 3D

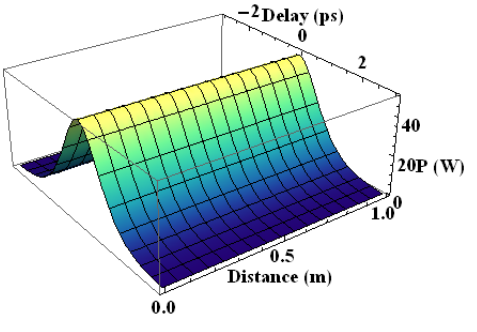

(b) Pulse propagation through single mode VFPCF shows in 3D

Figure 4. V-parameter values for VFPCF

Conclusion

In this project we designed a Photonic Crystal Fiber,called Void-Filled Photonic Crystal Fiber(VFPCF) and studied it's Confinement loss and V-parameter .Confinement loss of VFPCF is very less as compared to that of conventional photonic crystal fiber. V-Parameter results proved VFPCF can enroll in single mode PCF which have a major role in communication application. Cofinement loss decreased with increasing air hole diameter. The lowest confinement loss is obtained for void filled hexagonal PCFs with fixed 2 μm lattice pitch and 1.2μm diameter. The value of the V-parameter increases as the void air hole size expands, and it also rises with the increasing ratio of Λ/λ. VFPCF with void air hole diameter shows endlessly single mode in wide range of wavelength.Each VFPCFs can be performed as single mode when made with suitable pitch and diameter of air holes with respect to propagation wavelength.

Acknowledgement

We grategully thank the COMSOL multiphysics software for the simulation and analysis presented in this work.

References

[1] Gamst, M. (2014). Exact and heuristic solution approaches for the integrated job scheduling and constrained network routing problem. Discrete Applied Mathematics, 164, 121-137.

[2] Hecht, J. (2004). City of light: the story of fiber optics. Oxford University Press, USA.

[3] Poli, F., Cucinotta, A., Selleri, S. (2007). Photonic crystal fibers: properties and applications (Vol. 102). Springer Science Business Media.

[4] Khalid, M., Arshad, I., Zafarullah, M. (2014). Design and simulation of photonic crystal fibers to evaluate dispersion and confinement loss for wavelength division multiplexing systems. The Nucleus, 51(2), 249-258.

[5] Mortensen, N. A., Folkenberg, J. R., Nielsen, M. D., Hansen, K. P. (2003). Modal cutoff and the V parameter in photonic crystal fibers. Optics letters, 28(20), 1879-1881.

[6] Penjweini, R., Weber, M., Sondermann, M., Boyd, R. W., Leuchs, G. (2019). Nonlinear optics with full three-dimensional illumination. Optica, 6(7), 878-883.

Physics Research Reports (2024), **3–1**

PHYSICAL SCIENCE RESEARCH RESULTS

Study of Optical Properties of Aerosols using Incoherent Broadband Cavity Enhanced Extinction Spectroscopy and Theoretical Calculation using Computational Methods

Lulu Parveen C,[1] Dr. M.K Ravi Varma,[*,2] and Salma Jose[2]

[1]Department of Physics, Sullamussalam Science College, Areekode, Kerala, India 673639
[2]Proffesor,Department of Physics, NIT calicut
[*]Corresponding author. Email: r.varma@nitc.ac.in

Abstract

Aerosol influence earth atmospheric radiative forcing equilibrium by scattering and absorption incoming solar radiation. The optical properties of aerosol such as extinction coefficient, Single Scattering Albedo(SSA),aerosol optical depth(AOD), defines the direct aerosol- radiation interaction. In this work SSA of NaCl aerosol was found by Broadband cavity enhanced extinction spectroscopy and its theoretical calculation was done using Mie theory based computational analysis. Experimentally,IBBCEES measures extinction by evaluating the attenuation of light beam transmitted through a cavity. While aethalometer measures absorption by analysing attenuation of a light beam transmitted through a filter paper that continuously collects aerosol sample. By combining extinction and absorption measurements, the scattering coefficient of various aerosols is calculated. The single scattering albedo (SSA), determined from scattering and extinction measurements, indicates the relative contributions of scattering and absorption in the atmosphere. Inorder to theoretically find the Mie scattering and absorption efficiencies, a Python code was written based on Mie theory and the SSA was calculated. The value of single scattering albedo was found to be closely matching with the experimental results and this validates the application of IBBCEES for studying aerosol properties.

PG Department of Physics, S.S. College - Areekode

Keywords: IBBCEES, Aethalometer, Aerosol, SSA, Mie scattering

Introduction

Atmospheric aerosols[3] have significant local, regional and global impacts. Word Aerosol is used to describe mixture of small liquid and or solid particles dispersed in a gaseous system such as air[1].Study of Optical Properties of Aerosols using Incoherent Broadband Cavity Enhanced Extinction Spectroscopy and Theoretical Calculation using Computational Methods Aerosols vary in their disparity. Radiative forcing[2] is a concept to describe how various factors affect the balance of energy in the Earth's atmosphere.Any change in this balance between incoming and outgoing energy described by Radiative forcing. Mainly two types- Positive radiative forcing and Negative radiative forcing[2].Single scattering albedo (SSA)[4] is a optical property of aerosol which measure used in atmospheric science and optics to characterize the interaction of electromagnetic radiation with particles suspended in the atmosphere, such as aerosols or cloud droplets. It represents the ratio of scattering efficiency to extinction efficiency for a single scattering event. SSA values range from 0 to 1 , where: SSA = 0 indicates complete absorption of incident light and SSA = 1 indicates complete scattering of incident light[5].Scattering can be described as When electromagnetic radiation interacts with this particle, the dipoles within it begin to oscillate at the same frequency as the incident radiation. As a consequence, the electromagnetic radiation scatters in various directions.

IBBCEES is a instrument used to measure the extinction coefficient of aerosol material. By using the equation for minimum absorption coefficient $(\alpha)_{min}$ can be calculated[6].

$$\alpha_{\min} = \frac{1}{d}\frac{\Delta I_{\min}}{I_o}(1-R) \tag{1}$$

Theoretical Method

When light interacts with small particles, it can be scattered in various directions. The amount and direction of scattering depend on the size of the particles relative to the wavelength of the light. There are mainly three types of scattering.Rayleigh scattering, Mie scattering[7], Non-selective Scattering.In Mie theory, the electromagnetic concept and Maxwell's equations are used to derive the incident and scattered fields. Vector spherical harmonics are employed to calculate the cross sections, efficiency factors, and intensity distributions of the scattering particle under consideration.By solving Mie Coefficients are[7]:

$$a_n = \frac{\psi_n^t(y)\psi_n^t(x) - \psi_n(y)\chi_n^t(x)}{m\psi_n(y)\xi_n^t(x) - \psi_n(y)\chi_n(x)}$$

$$b_n = \frac{m\psi_n^t(y)\psi_n^t(x) - \psi_n(y)\xi_n^t(x)}{m\psi_n(y)\xi_n^t(x) - \psi_n(y)\chi_n(x)}$$

$$c_n = \frac{m\psi_n^t(x)\xi_n(x) - \psi_n(x)\chi_n(x)}{\psi_n(y)\xi_n(x) - \psi_n(y)\chi_n(x)}.$$

$$d_n = \frac{m\psi_n^t(x)\xi_n(x) - \psi_n(x)\chi_n(x)}{m\psi_n(y)\xi_n(x) - \psi_n(y)\chi_n(x)}.$$

By using Python code for finding Mie Coefficient, Mie efficiencies, from there fining value of SSA.

Instrumentation and Experimental procedure

Inchorent Broadband Cavity Enhanced Extinction Spectrometer(IBBCEES)[8] which measures the transmission of light intensity through a stable optical cavity consisting of high reflectance mirrors (typically exceeding 99.9% reflectance). Here we detect the Aerosol extinction coefficient This technique utilizes incoherent radiation sources such as Xenon arc lamps, LEDs, or Laser-driven light sources (LDLS). Calibration of the IBBCEES system in laboratory settings often involves the use of a lowloss optical window.IBBCEES allows for the direct retrieval of the imaginary part of the refractive index based on the measured wavelength-dependent aerosol extinction cross-section. Typically, wavelength selection of transmitted light occurs post-cavity through dispersive interferometric means. Transmission signal strength in IBBCEES, akin to other cavity-enhanced spectroscopic techniques, is assessed with and without the absorber present within the cavity. From the ratio of wavelength-dependent transmitted intensities samples extinction coefficient can be measured by[8]

$$\alpha = \left(\frac{I_0\lambda}{I(\lambda)} - 1\right)\frac{1 - Reff(\lambda)}{d} \tag{2}$$

Sensitivity in IBBCEES is optimized with larger mirror reflectivities and cavity path lengths, with maximal efficiency achieved when the sample path length matches the cavity length. IBBCEES can be employed in either open or closed path configurations. In closed path setups, the sample passes through the cavity enclosed by two highly reflective mirrors. Conversely, open path configurations, as utilized in outdoor measurements, mitigate wall losses but face challenges in measuring trace gas concentrations accurately, especially in the presence of high aerosol concentrations. Additionally, the lack of a clean air reference spectrum poses difficulties

for mirror reflectivity calibration and concentration measurements in open path setups.IBBCEES setuo is shown in figure1a

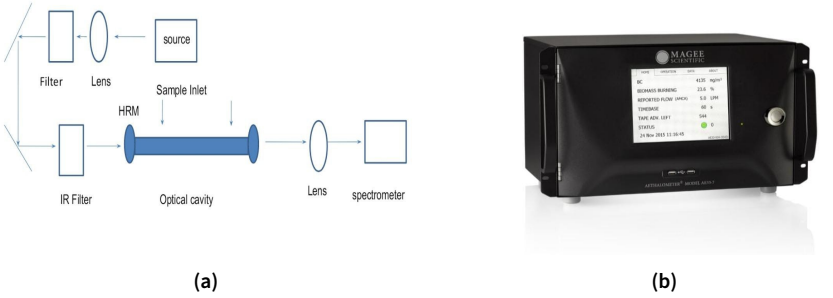

(a) (b)

Figure 1. (a)IBBCEES setup (b) Aethalometer

Aethalometer-The Aethalometer model AE33[9] continuously collects aerosol particles by drawing air through a filter tape. It analyzes these particles by measuring light transmission through a sample portion of the tape compared to an unloaded reference area. This analysis spans seven optical wavelengths from near-infrared to near-ultraviolet. By calculating the rate of light attenuation through the particle-laden filter, the Aethalometer determines the instantaneous concentration of optically-absorbing aerosols. In the new AE33 model, two measurements are simultaneously obtained from sample spots with different accumulation rates, allowing for compensation of particle light absorption and black carbon mass concentration. The instrument provides continuous real-time data without operator intervention, correcting for filter loading effects. figure of Aethalometer model AE33 is shown in 1b The experimental procedure for determining the aerosol extinction coefficient using Incoherent Broad Band Cavity Enhanced Extinction Spectroscopy (IBBCEES) consists of four main steps:

1. Cavity Alignment
2. Calibration of Mirror Reflectivity
3. Aerosol Preparation
4. Determine the Aerosol Extinction Coefficient

Observations and Results

Experimental result

Before determine the light extinction coefficient, calibrate the IBBCEES. To calibrate IBBCEES determine the mirror reflectivity. It is done by passing dry air through optical cavity followed by NO_2 gas. The reflectivity curve is given in figure2a.From the graph we can see that reflectivity of mirror is calibrated to approximately value of 0.9975.

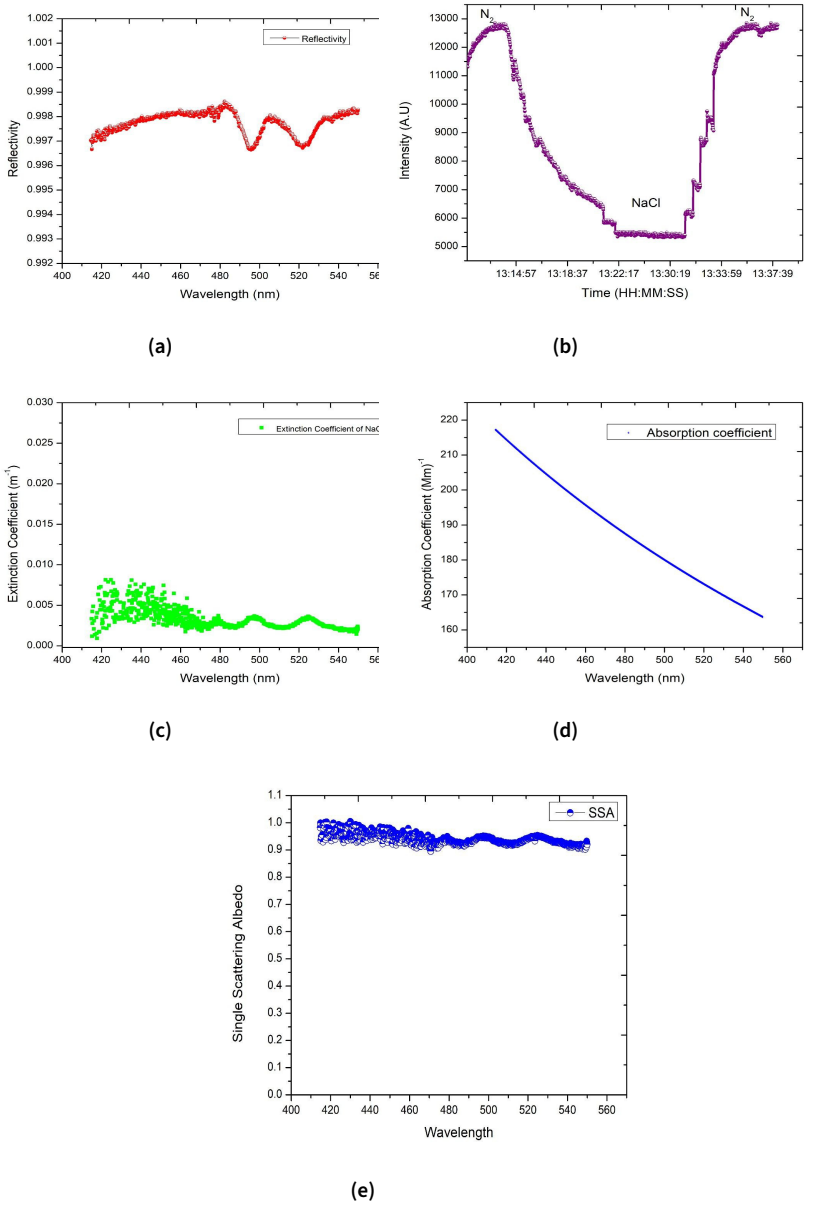

Figure 2. (a)Mirror Reflectivity Calibration,(b)Intensity vs Time(530.469),(c)Extinction Coefficient of NaCl aerosol,(d)Absorption Coefficient, (e)SSA of NaCl

The light extinction coefficient of NaCl aerosol is determined by passing NaCl aerosol through cavity enhanced extinction spectrometer.The experiment was conducted in using aerosols generated by NaCl in ambient laboratory conditions.

SL. NO.	TIME	TYPE OF GAS OR AEROSOL
1.	13:10-13:14	NITROGEN GAS
2.	13:15-13:32	NaCl
3.	13.32-13.36	NITROGEN GAS

The intensity Vs time curve of light at wave length 530. 469 nm is given in figure2b.While analysing the curve it is found that the intensity decreases suddenly at NaCl enters to the cavity. Since NaCl have high absorption capacity.

Determine the aerosol extinction coefficient by passing N2 gas then NaCl aerosol through optical cavity.. Using the theory of IBBCEES, the extinction coefficient is calculated and plotted against the wavelength. It is seen that intensity decreases when aerosol passing through the cavity, because light easily scattered in the presence of aerosol.From figure 2cAerosol extinction coefficient approximately $4.35x10^{-}3$ m in 522.19 nm.

The aethalometer provides absorption coefficients at seven discrete wavelengths(370 nm, 470 nm, 520 nm, 590 nm, 660 nm, 880 nm, 950 nm). In this study the spectral region of interest ranges from 400nm to 550 nm.The scattering coefficient is found by subtracting absorption coefficient from extinction coefficient. Which is shown in figure 2d

Theoretical result

Here the Mie efficiencies was calculated for 500 nm wavelength.

Mie Coefficients

Coefficients of extinction

a_n=[4.06298457e-02-1.97424932e-01j 1.20275476e-04-1.09611667e-02j 8.57414278e-08-2.88005583e-04j 6.13214987e-11-4.42035526e-06j 4.10813009e-13-4.38572574e-08j 2.80368820e-15-3.03301296e-10j 1.41856757e-17-1.54369379e-12j]

Coefficients of scattering

b_n=[1.00370763e-03-3.16564405e-02j 7.16081427e-07-8.38187808e-04j 3.78021663e-10-1.31445422e-05j 2.06236360e-12-1.32795539e-07j 1.42342256e-14-9.31314795e-10j 7.29111603e-17-4.79221119e-12j 2.86029088e-19-1.88549330e-14j]

Coefficients of back-scattering

c_n=[8.58111344e-01+2.71921804e-02j 4.88530324e-01+4.06347941e-04j 3.02528080e-01+4.98329026e-07j 1.91710867e-01-3.08249118e-06j 1.22601668e-01-2.54790176e-06j 7.87717992e-02-1.99151429e-06j 5.07490453e-02-1.50925203e-06j]

Coefficients of absorption

d_n=[9.07699961e-01+1.86791525e-01j 4.94818661e-01+5.42074658e-03j 2.93668696e-01+8.08059097e-05j 1.83100347e-01-2.42431081e-06j 1.16068499e-01-2.58169139e-06j 7.41483085e-02-1.98883763e-06j 4.75757978e-02-1.48947337e-06j]

Mie Efficiencies

Input:[np.real(m), np.imag(m), x, qext, qsca, qabs]
output: [1.541, 6.7e-06, 12.566, 0.00269875675183762, 0.00269679691469581 3, 1.9598371418069922e-06]

SSA Of NaCl

scattering coefficient=0.00269679691469581 3
extinction coefficient=0.00269875675183762

$$SSA = \frac{0.00269679691469581 3}{0.00269875675183762} = 0.99 \quad (3)$$

Conclusion

The IBBCEES experiment was conducted using NaCl in ambient laboratory conditions. The extinction coeff icient was found to be decreasing with increasing wavelength. The amount of light absorbed by aerosols from sample was observed to be less than the amount of light scattered. The single scattering albedo (SSA) was determined from the scattering and extinction measurements. The SSA of aerosols determines the relative contribution of scattering and absorption in the atmosphere. NaCl have value of SSA near to 1 which predominantly scatter solar radiation back to space, leading to a cooling effect on the climate. This technique is a powerful tool to understand the effect of different aerosols on climate. The understanding and quantification of aerosol effects on climate are active areas of research and involve complex interactions that are challenging to model and predict accurately. By using Python code for solving Mie efficiencies,absorption efficiencies, scattering efficiencies, SSA is found, which is exactly matching with the experimental result. The instrument can be extended to ambient atmosphere, so it is a powerful tool for obtaining the concentration of different particles present in the atmosphere. Aerosol play an important role is earth's climate. NaCl salt aerosol are most widely seeing natural aerosol. Due to the increasing anthropogenic emission of aerosol since the industrial revolution, they effect the global climate change. Also they play

an important role in radiation budget of the earth.

Acknowledgement

This work was under the intense supervision of Dr.Ravi Varma, professor,National Institute of Technology Calicut and Miss Salma Jose PhD student,National Institute of Technology Calicut.

References

[1] Satheesh, S. K., Moorthy, K. K. (2005). Radiative effects of natural aerosols: A review. Atmospheric Environment, 39(11), 2089-2110.

[2] Seinfeld, J. H., Pandis, S. N. (2016). Atmospheric chemistry and physics: from air pollution to climate change. John Wiley Sons.

[3] Hinds, W. C., Zhu, Y. (2022). Aerosol technology: properties, behavior, and measurement of airborne particles. John Wiley Sons.

[4] Parungo, F., Nagamoto, C., Maddl, R. (1987). A study of the mechanisms of acid rain formation. Journal of Atmospheric Sciences, 44(21), 3162-3174.

[5] Thomas, S., Thomas, R., Zachariah, A. K., Kumar, R. (Eds.). (2017). Thermal and rheological measurement techniques for nanomaterials characterization (Vol. 3). Elsevier.

[6] Fiedler, S. E., Hese, A., Ruth, A. A. (2003). Incoherent broad-band cavity-enhanced absorption spectroscopy. Chemical physics letters, 371(3-4), 284-294.

[7] Kerker, M. (2016). The scattering of light and other electromagnetic radiation. Elsevier.

[8] Fang, B., Zhao, W., Xu, X., Zhou, J., Ma, X., Wang, S., ... Chen, W. (2017). Portable broadband cavity-enhanced spectrometer utilizing Kalman filtering: application to real-time, in situ monitoring of glyoxal and nitrogen dioxide. Optics Express, 25(22), 26910-26922.

[9] Dutt, U., Jiang, N., Ross, G., Gunaratnam, G. (2018). Application of the aethalometer for black carbon source analysis. Air Quality and Climate Change, 52(3), 6-10.

Physics Research Reports (2024), **3–1**

PHYSICAL SCIENCE RESEARCH RESULTS

Investigation Of Structural Properties of Ionic Liquids and Toxicity Prediction Using DFT

M.C Fathima Naja and Abdul Rahoof K.A

Department of Physics, Sullamussalam Science College, Areekode, Kerala, India 673639

Abstract

This study investigates the structural properties of specific ionic liquids (ILs) and predicts their toxicity using density functional theory (DFT) calculations. The study focuses on examining the influence of size, symmetry, and electronegativity of anion and cation on the structural properties and toxicity of ILs. A methodical investigation of ILs is conducted by considering various combinations of cations and anions. Structural features, including the highest occupied molecular orbital (HOMO), lowest unoccupied molecular orbital (LUMO), and electronic descriptive parameters, are examined using DFT calculations by Gaussian software. The analysis provides insights into the electronic structure, stability, and reactivity of the ILs, with a particular emphasis on understanding the impact of anion and cation properties. Subsequently, toxicity prediction models for the ILs are developed based on the structural information obtained from DFT calculations. Computational methods are employed to predict toxicity, with a notable observation that toxicity effects are more pronounced when altering the anion component compared to the cation component. By correlating electronic structure descriptors with experimental toxicity data or established toxicity prediction methodologies, the toxicity of the investigated ILs is predicted. Additionally, reactivity orders are determined using these descriptors to further elucidate the relationship between IL structure and toxicity.

Keywords: Anion Toxicity,Ionic Liquid,Daphnia Magna,Guassian Software,DFT

PG Department of Physics, S.S. College - Areekode

Introduction

Ionic liquids (ILs) are materials composed of large organic or inorganic cations (e.g., imidazolium, pyridinium) and small anions (e.g., nitrate, tetrafluoroborate, dicyanamide), which are liquid at or below 100°C. They possess unique properties such as negligible vapor pressure, low flammability, high ionic conductivity, and excellent thermal and chemical stability, making them suitable for various applications, including fuel cells, batteries, sensors, and pharmaceutical drug discovery [1] [2] A critical application of ILs in pharmaceuticals is improving the solubility of poorly soluble drugs, which is essential for their efficacy at target sites.[3]

Despite being considered green, some ILs can cause environmental pollution and toxicity to organisms like fish, bacteria, and humans. Toxicity measurements are crucial for ensuring safety, assessing environmental and health risks, and developing greener ILs[4]While experimental toxicity tests involve living organisms and provide EC_{50} values indicating toxicity levels, computational methods, such as density functional theory, are preferred for their cost-effectiveness and efficiency.

Imidazolium and pyridinium-based ILs are particularly notable for their thermal stability, high ionic conductivity, tunability, wide electrochemical window, and amphoteric behavior. These properties make them suitable for a wide range of applications, and their toxicity can be assessed computationally to support safer and more sustainable use.

1. Theoretical Studies

1.1 Toxicity Representation

1.1.1 EC_{50} VALUE:

The EC50 value, or "Effective Concentration 50%", indicates the concentration of a substance needed to produce a specific effect in 50% of a test population. This measure is crucial in toxicology, pharmacology, environmental science, and risk assessment. The log [EC50], obtained by taking the base-10 logarithm of the EC50, compresses a wide range of concentration values for easier analysis. For ionic liquids, the log [EC50] value is an important indicator of toxicity, especially to aquatic organisms like Daphnia magna, a common model organism in ecological and toxicological research due to its sensitivity to contaminants. A lower log [EC50] value signifies higher toxicity, indicating that a lower concentration of the substance adversely affects 50% of the test organisms. This value helps quantify the acute toxicity of ionic liquids to Daphnia magna and allows comparison with other substances to assess relative hazards. The log [EC50] is also used in modeling equations for toxicity prediction.

1.2 Modelling of Equation

In this work, we used a model equation developed by Nu'Aim and Bustam to determine the toxicity of selected ionic liquids (ILs). This model, based on multiple linear regression (MLR) analysis, predicts toxicity (log [EC50]) by correlating it with significant molecular descriptors. The descriptors analyzed were the highest occupied molecular orbital energy (E*HOMO*), lowest unoccupied molecular orbital energy (E*LUMO*), hardness (η), chemical potential (μ), electrophilicity index (ω), energy gap (ΔE), and electronegativity (χ). The analysis identified E*HOMO* and E_{LUMO} for both cation and anion, and the cation's electrophilicity index (ω) as significant descriptors. This approach helps in predicting the toxicity of ILs to Daphnia magna based on these molecular properties. .

The correlation is a linear equation as shown below

$$\log[EC_{50}] = -1.1263 - 0.00991(E_{HOMO}, \text{cation}) + 0.0039995(E_{LUMO}, \text{cation}) + 0.00005(\omega, \text{cation}) + 0.00535(E_{HOMO}, \text{anion}) - 0.004511(E_{LUMO}, \text{anion})$$

In the model equation for predicting the toxicity (log [EC50]) of ionic liquids to Daphnia magna, five significant descriptors were identified: the electrophilicity index of the cation, and the HOMO and LUMO energies of both the cation and anion. These descriptors are estimated using density functional theory (DFT) in Gaussian software. The structures of the chosen ionic liquids are drawn and optimized using the DFT technique in Gaussian. The E*HOMO* and E_{LUMO} values for both cations and anions are obtained from their optimized structures. Additionally, other descriptors such as the energy gap, chemical potential, electronegativity, and hardness are calculated using formulas involving the HOMO and LUMO values[4].

:

Table 1. Descriptors Calculation

Descriptors	Formula
Energy Gap (ΔE)	$\Delta E = E_{LUMO} - E_{HOMO}$
Chemical Potential (μ)	$\mu = (E_{HOMO} + E_{LUMO}) / 2$
Hardness (η)	$\eta = (E_{LUMO} - E_{HOMO}) / 2$ $\eta = (\Delta E) / 2$
Electrophilicity Index (ω)	$\omega = (\mu 2) / (2\eta)$
Electronegativity (χ)	$\chi = (- E_{HOMO} - E_{LUMO}) / 2$

By obtaining the descriptor values, we can determine log [EC_{50}] values of the ionic liquid and determine its toxicity.

2. Result and Discussion

2.1 Calculated Descriptors of ILs

Table 2. Calculated Descriptors of Pyridinium ILs

pyridinium cation	E_{HOMO}	E_{LUMO}	Energy gap	Chemical potential	Hardness	Electro philicity index	Electro negativity
1.1-n-ethyl pyridinium	-0.46855	-0.24952	0.21903	0.35904	0.109515	0.588532	-0.359035
2.1-n-butyl pyridinium	-0.45502	-0.24562	0.2094	0.35032	0.1047	0.586075	-0.35032
3.1-butyl-3-methyl pyridinium	-0.44416	-0.23843	0.20573	0.3413	0.102865	0.56619	-0.341295
4.1-butyl-4-methyl pyridinium	-0.45079	-0.23336	0.21743	0.34208	0.108715	0.538175	-0.342075
5.1(carboxymethyl) pyridinium	-0.45128	-0.25369	0.19759	0.35249	0.098795	0.628805	-0.352485

2.2 Reactivity Order of Imidazolium and Pyridinium Cation

• lower hardness and higher electrophilicity indicate higher reactivity.(Islam et al., n.d.)

• Imidazolium cation reactivity order:

1-ethyl-2,3-dimethyl imidazolium > 1,3-dimethyl imidazolium > 1-butyl-3-methyl
imidazolium > 1-butyl- 2,3-dimethyl imidazolium > 1-ethyl-3-methyl imidazolium

• Pyridinium cation reactivity order:

1(carboxymethyl) pyridinium > 1-n-ethyl pyridinium > 1-n-butyl pyridinium > 1-butyl-3-methyl
pyridinium > 1-butyl-4-methyl pyridinium

• In drug discovery, understanding the reactivity of drug molecules is essential for optimizing their efficacy, safety. It helps in drug stability, to predict toxic formations.

2.3 Analysing Toxicity Effect of Anion and Cation Part

Table 3. Anion Toxicity on Pyridinium based ILs

Pyridinium IL	Log [EC_{50}] values	Pyridinium IL with different anion	Log [EC_{50}] values	Δlog[EC_{50}] values
1. 1-butyl-3-methyl pyridinium bromide	-1.1238	1-butyl-3-methyl pyridinium dicyanamide	-1.1238	0.00032
		1-butyl-3-methyl pyridinium tetrafluoroborate	-1.1241	0.00014
		1-butyl-3-methyl pyridinium diethyl phosphate	-1.1236	0.0001
		1-butyl-3-methyl pyridinium thiocyanate	-1.1237	0.00001
		1-butyl-3-methyl pyridinium hexafluorophosphate	-1.1247	0.00093
2. 1-butyl-3-methyl pyridinium dicyanamide	-1.1238	1-butyl-3-methyl pyridinium tetrafluoroborate	-1.1241	0.00046
		1-butyl-3-methyl pyridinium diethyl phosphate	-1.1236	0.00042
		1-butyl-3-methyl pyridinium thiocyanate	-1.1237	0.00031
3. 1-butyl-3-methyl pyridinium tetrafluoroborate	-1.12412	1-butyl-3-methyl pyridinium diethyl phosphate	-1.12366	0.00004
		1-butyl-3-methyl pyridinium thiocyanate	-1.1237	0.00015
		1-butyl-3-methyl pyridinium hexafluorophosphate	-1.12473	0.00107
4. 1-butyl-3-methyl pyridinium diethyl phosphate	-1.1236	1-butyl-3-methyl pyridinium thiocyanate	-1.1237	0.000111
		1-butyl-3-methyl pyridinium hexafluorophosphate	-1.1247	0.00103
5. 1-butyl-3-methyl pyridinium thiocyanate	-1.1237	1-butyl-3-methyl pyridinium hexafluorophosphate	-1.1247	0.00092
Average				0.000564

Table 4. Cation Toxicity Effect on Pyridinium based ILs

Pyridinium IL	Log [EC_{50}] values	Pyridinium IL with different cation	Log [EC_{50}] values	Δlog[EC_{50}] values
1. 1-butyl-3-methyl pyridinium bromide	-1.1238	1-ethyl pyridinium bromide	-1.12361	0.0002
		1-butyl pyridinium bromide	-1.1237	0.00008
		1-butyl-4-methyl pyridinium bromide	-1.12372	0.00009
		1 carboxymethyl pyridinium bromide	-1.1237	0.00002

2.1-ethyl pyridinium bromide	-1.12361	1-butyl pyridinium bromide	-1.1237	0.00012
		1-butyl-4-methyl pyridinium bromide	-1.1237	0.00011
		1 carboxymethyl pyridinium bromide	-1.1237	0.00018
3.1-butyl pyridinium bromide	-1.12373	1-butyl-4-methyl pyridinium bromide	-1.1237	0.00001
		1 carboxymethyl pyridinium bromide	-1.1237	0.00006
4.-butyl-4-methyl pyridinium bromide	-1.1237	1 carboxymethyl pyridinium bromide	-1.12379	0.00007
Average				0.000094

When substituting anions (dicyanamide, diethyl phosphate, thiocyanate, tetrafluoroborate, hexafluorophosphate) while keeping the cation constant (1-butyl-3-methyl pyridinium), the average toxicity difference was 0.000564. Conversely, when varying the cation (substituting 1-ethyl pyridinium, 1-butyl pyridinium, 1-butyl-4-methyl pyridinium, 1-carboxymethyl pyridinium) while keeping the anion constant (bromide), the average toxicity difference was 0.000094. This indicates that changes in the anion component have a greater impact on IL toxicity compared to changes in the cation component.

3. Conclusion

In conclusion, this study conducted a detailed investigation into the structural properties and toxicity prediction of certain ionic liquids (ILs) using density functional theory (DFT) calculations. The analysis focused on the properties of cations and anions, their toxicity representations, and reactivity orders. Key findings include insights into the electronic structure and reactivity of ILs, highlighting their potential toxicity and environmental and health risks. The study identified the reactivity order of pyridinium and imidazolium cations, aiding in the selection of safer cations for pharmaceutical applications. Notably, altering the anion component was found to have a more significant impact on toxicity than changing the cation. These findings offer valuable insights for designing safer ILs and have broader implications for fields like environmental science, toxicology, and materials chemistry. Future research should further investigate the mechanisms behind these toxicity differences and explore the relationship between IL structure, toxicity, and environmental impact to develop predictive models and guidelines for creating environmentally benign ILs.

Acknowledgement

This work was supported by Department of Physics, University of Calicut for providing the computational work.

References

[1] Shukla, M. K., Tiwari, H., Verma, R., Dong, W. L., Azizov, S.,Kumar, B., ... Kumar, D. (2023). Role and recent advancements of ionic liquids in drug delivery systems. Pharmaceutics, 15(2), 702.

[2] Kianfar, E., Mafi, S. (2021). Ionic liquids: properties, application, and synthesis. Fine Chemical Engineering, 21-29.

[3] Gonçalves, A. R., Paredes, X., Cristino, A. F., Santos, F. J. V., Queirós, C. S. (2021). Ionic liquids—A review of their toxicity to living organisms. International Journal of Molecular Sciences, 22(11), 5612.

[4] Nu'aim, M. N., Bustam, M. A. (2018, April). Toxicity prediction of ionic liquids based on Daphnia magna by using density functional theory. In IOP Conference Series: Materials Science and Engineering (Vol. 344, No. 1, p. 012017). IOP Publishing.

Physics Research Reports (2024), **3–1**

PHYSICAL SCIENCE RESEARCH RESULTS

Synthesis, characterisation and antibacterial activity of copper oxide nanoparticles

Fathima Diya E[1] and Mohemmed Shanid N A[*,2]

[1]Department of Physics, Sullamussalam Science College, Areekode, Kerala, India 673639
[2]Department of Physics, Sullamussalam Science College, Areekode, Kerala, India 673639
[*]Corresponding author. Email: namshanid@sscollege.ac.in

Abstract

Copper oxide is a promising material with potential applications in electronics, catalysis, and energy storage. Its unique size-dependent physical and chemical properties make it ideal for its applications. This study investigates the structural properties of copper oxide using hydrothermal route synthesis and X-ray diffraction and Raman spectroscopy. The results show a monoclinic crystal structure with lattice parameter values comparable to standard ones, with highly crystalline crystals. This method can be used to obtain crystalline and well-formed CuO crystals with a slightly smaller lattice parameter than conventional methods. Raman spectroscopy reveals characteristic active peaks, which can help identify different crystal phases and defects within CuO. The study also investigates the antibacterial activity of nanostructured polycrystalline CuO, finding higher inhibition rates in E. coli (Gram positive) than Staphylococcus aureus (Gram negative). This suggests CuO as a promising material for antimicrobial applications. The extension of this study could lead to smart materials for specific applications in healthcare and biotechnology.

Keywords: Copper oxide,X-ray diifraction, Raman spectroscopy, High resolution transmission electron microscope, Antibacterial activity

PG Department of Physics, S.S. College - Areekode

1. Introduction

Nanostructures of transition metal oxides are pivotal in catalysis, sensing, and biomedical applications . Copper oxide (CuO), a p-type semiconductor with high thermal conductivity and antimicrobial activity, shows promise in various fields including catalysis, sensors, and healthcare . Synthesis techniques such as microwave-assisted, co-precipitation, and hydrothermal methods are discussed for their role in tailoring CuO nanoparticle properties, crucial for optimizing performance in various technological applications. This study focuses on synthesizing CuO nanoparticles via hydrothermal treatment, known for producing well-defined nanostructures with controlled size and crystallinity. The 9-hour hydrothermal reaction yielded small-sized CuO crystals in the monoclinic phase . Structural characterization using X-ray diffraction (XRD), Raman spectroscopy, and high-resolution transmission electron microscopy (HRTEM) confirmed the nanoparticles' crystallinity, phase purity, and morphology suitable for advanced applications . Antibacterial activity of CuO nanoparticles was evaluated against Gram-positive (e.g., Staphylococcus aureus) and Gram-negative bacteria (e.g., Escherichia coli) using agar diffusion methods, showing significant inhibition of bacterial growth. The study aims to elucidate the mechanism of interaction between CuO nanoparticles and bacteria.

2. Experimental techniques

2.1 Hydrothermal synthesis of copper oxide nanoparticles

Copper oxide nanoparticles were synthesized via hydrothermal treatment. CTAB (7.52 g) and $CuCl_2 2H_2O$ (7.0 g) were dissolved in 80.0 ml of deionized water. NaOH (39.96 ml) and AH_2 (7.04 ml) in 400 ml of deionized water were added dropwise. The solution was stirred for 9 hours, followed by settling and washing to isolate Cu_2O particles, which were annealed at 300^oC and 250^oC to obtain CuO nanoparticles[1]

2.2 Antibacterial Study

a)Agar Well Diffusion

0.1% CuO nanoparticle solution was tested for antibacterial activity using agar well diffusion on Muller Hinton agar plates. Escherichia coli and Staphylococcus aureus cultures were spread on plates, and 6 mm wells were made. After incubation at 37^oC for 24 hours, inhibition zone diameters were measured to assess effectivenesss[2]

b)Agar Disc Diffusion

Antibacterial efficacy was further evaluated using the agar disc diffusion method with Ampicillin discs as controls. Test organisms were cultured on Muller Hinton agar plates, and antibiotic discs were placed. After 24-hour incubation at 37^oC, inhibition zones around discs were measured for comparison.

3. Result and Discussion

X-ray diffraction (XRD) analysis of CuO nanoparticles annealed at 250^oC and 300^oC confirms a monoclinic crystal structure, evidenced by characteristic peaks at 2θ values of 35.5^o, 38.8^o, and 48.8^o corresponding to (-111), (111), and (-202) planes. The crystallite sizes were determined to be 22.1 nm and 23.5 nm for the samples annealed at 250^oC and 300^oC, respectively, using the Scherrer equation [3]Interplanar spacings closely align with theoretical values, indicating the persistence of the monoclinic phase.

Raman spectra of the samples exhibit characteristic peaks at $279cm^-1$, 313 cm^-1, and 612 cm^-1 for the 250^oC annealed CuO, and 285 cm^-1, 333 cm^-1, and 621 cm^-1 for the 300^oC annealed CuO, corresponding toA_g, B_{1g}, and B_{2g}modes [4]Minor Cu_2O peaks suggest the presence of phase impurities, while shifts in Raman modes indicate structural modifications influenced by annealing temperature.

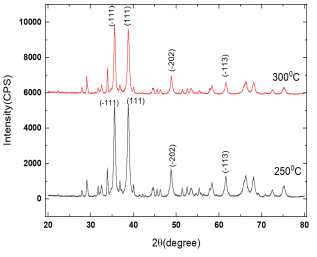

Figure 1. XRD plot of CuO annealed at 250^oC and 300^oC temperatures

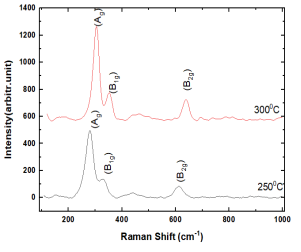

Figure 2. Raman spectra of CuO annealed at 250^oC and 300^oC

High-resolution transmission electron microscopy (HRTEM) analysis of CuO samples annealed at 250 °C and 300 °C revealed significant differences in crystal sizes compared to X-ray diffraction (XRD). Specifically, HRTEM demonstrated larger crystal sizes for the sample annealed at 250 °C, indicating the presence of larger particles or clusters that XRD, with its sensitivity to smaller crystals, could not effectively resolve. Moreover, the detection of Cu_2O phase in this sample suggested incomplete oxidation and a less crystalline structure, contributing to the observed differences in crystal size measurements between HRTEM and XRD.

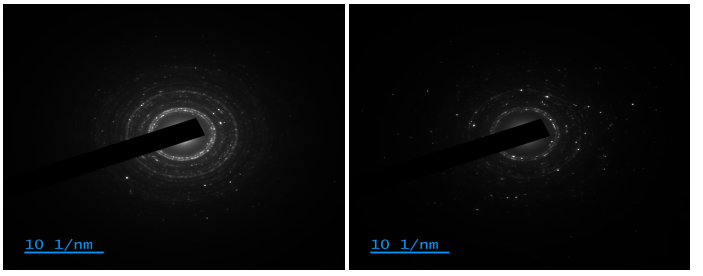

Figure 3. SAED image of CuO annealed at 300^oC and 250^oC temperature

3.1 Antibacterial activity

When CuO nanoparticles are annealed at 250°C, they exhibit 10 mm and 15 mm inhibition zones against S. aureus and E. coli, respectively. Annealing at 300°C increases these zones to 16 mm for S. aureus and 16 mm for E. coli. This demonstrates stronger antibacterial effects of CuO nanoparticles against E. coli compared to S. aureus, with larger inhibition zones observed at both annealing temperatures.

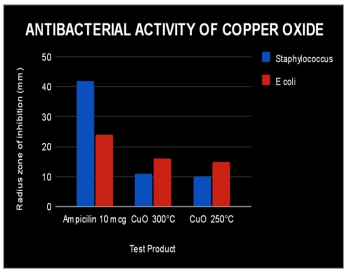

Figure 4. Bar diagram of antibacterial activity of CuO

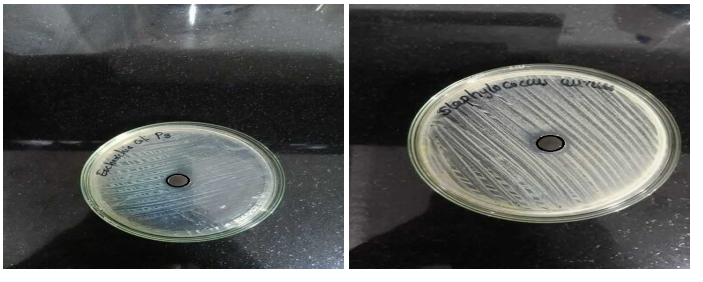

Figure 5. E. coli and S. aureus bacterial colonies cultured on petri dishes, demonstrating the antibacterial efficacy of CuO nanoparticles annealed at temperatures of 250^oC and 300^oC

Figure 6. S. aureus and E. coli bacterial colonies cultured on petri dishes, demonstrating the antibacterial efficacy of CuO nanoparticles annealed at temperatures of 250^oC and 300^oC .

Figure 7. S. aureus and E.coli colonies formed on petri dishes in the presence of control drug

3.1.1 Mechanism of antibacterial activity

Copper oxide nanoparticles (CuO NPs) exhibit potent antibacterial effects through two main mechanisms: Firstly, their small size (20–30 nm) and high surface area-to-volume ratio enable effective interaction with bacterial cell walls. The positively charged surface of CuO NPs enhances this interaction via electrostatic attraction, particularly effective against gram-negative bacteria with thinner cell walls. This disrupts the peptidoglycan layer, compromising cell wall integrity and leading to cell death.

Secondly, CuO NPs catalyze the generation of reactive oxygen species (ROS) near bacterial cell walls. These ROS molecules, including free radicals and peroxides, degrade peptidoglycan components, weakening the cell wall and causing cellular damage, eventually leading to cell lysis and bacterial death.

Further research is needed to determine the dominant mechanism of bacterial inhibition and optimize the application of CuO NPs. While promising as antimicrobial agents, ongoing studies are crucial to enhance effectiveness, minimize environmental impacts, and address safety concerns for human health [5]

4. Conclusion

CuO nanoparticles were synthesized via hydrothermal synthesis with capping, yielding highly crystalline monoclinic crystals with slightly reduced lattice parameters

due to negative stress. Characterization techniques including diffraction pattern analysis, Raman spectroscopy, and High-Resolution Transmission Electron Microscopy (HRTEM) confirmed the crystal quality and structure.

Antibacterial tests demonstrated significant efficacy against both Gram-negative E. coli and Gram-positive Staphylococcus aureus, with stronger inhibition observed against E. coli even at low concentrations compared to standard antibiotics. These results highlight CuO nanoparticles as promising candidates for antibacterial applications in healthcare and biotechnology.

Further research into the primary mechanisms of bacterial inhibition will be pivotal for optimizing the specificity and effectiveness of CuO nanoparticles in practical applications. This study lays a solid foundation for future advancements in utilizing CuO nanoparticles in biomedical and environmental contexts.

Acknowledgement

We extend our sincere gratitude to the faculty members of the Department of Physics at Sullamussalam Science College, Areacode, for their continuous encouragement and invaluable support throughout this research.

Additionally, we acknowledge with thanks the financial support provided by Sullamussalam Science College, Areacode, which was crucial for the successful completion of this study.

References

[1] Xudong Chen, Kangping Cui, Zibin Hai, Wu Kuang, Lingling Wang, Jiajia Zhang, and Xueying Tian. Hydrothermal synthesis of cu2o with morphology evolution and its effect on visible-light photocatal- ysis. Materials Letters, 297:129921, 2021.

[2] Jan Hudzicki. Kirby-bauer disk diffusion susceptibility test protocol. American society for microbiol- ogy, 15(1):1–23, 2009.

[3] Bernard Dennis Cullity. Elements of X-ray Diffraction. Addison-Wesley Publishing, 1956.

[4] Nogueira, B. A., Castiglioni, C. (2024). Raman Spectroscopy of Crystalline Materials and Nanostructures. Crystals, 14(3), 251.

[5] Yael N Slavin, Jason Asnis, Urs O H nfeli, and Horacio Bach. Metal nanoparticles: understanding the mechanisms behind antibacterial activity. Journal of nanobiotechnology, 15:1–20, 2017.

Physics Research Reports (2024), **3–1**

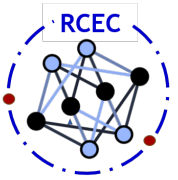

PHYSICAL SCIENCE RESEARCH RESULTS

Lens Modelling using Python to Simulate Gravitational Fields

Liyana P[1] and Sabeel P K[*,2]

[1]Department of Physics, Sullamussalam Science College, Areekode, Kerala, India 673639
[2]Department of Physics, Sullamussalam Science College, Areekode, Kerala, India 673639
[*]Corresponding author. Email: sharaf.saj@sscollege.ac.in

Abstract

Gravitational lensing, a significant phenomenon in astrophysics, provides valuable insights into the distribution of mass in the universe, including dark matter. Lenstronomy is a versatile software package specifically developed for modeling strong gravitational lensing. Scientists in the field of astronomy and astrophysics utilize this sophisticated tool to accurately simulate, analyze, and interpret data related to gravitational lensing events.This research focuses on simulating gravitational lensing phenomena and analyzing the resulting images using the lenstronomy package module within the Python programming language. The practical examples outlined in this text illustrate the diverse applications of lenstronomy, demonstrating its utility in research, data analysis, and preparation for upcoming astronomical observations.Key components of this study involve creating pixel grids to deconstruct the simulated image plane, incorporating point spread functions (PSF) to replicate the blurring effects of telescope optics, and employing numerical techniques for image generation and analysis. The simulation outcomes are compared against observed data, with noise sources such as Poisson and background noise included to enhance realism.Through minor adjustments to the software, significant improvements in results can be achieved, enabling the generation of simulations for each dataset input into the program. This research underscores the importance of computational tools in modern astrophysics, enabling in-depth investigations into gravitational lensing phenomena that advance our understanding of cosmic structure and evolution.

PG Department of Physics, S.S. College - Areekode

Keywords: Dye Sensitized Solar Cells,DSSC,natural dyes,performance of DSSC,degraded dyes

Introduction

During the early 20th century, the scientific community was abuzz with innovative ideas. One of the most groundbreaking concepts introduced during this time was Albert Einstein's theory of general relativity, which he unveiled in 1915[1]. This theory revolutionized our comprehension of gravity by portraying it not as a force that pulls objects together, but as a distortion of spacetime caused by mass and energy. At the core of this theory lies the notion of gravitational lensing, where massive celestial bodies such as stars and galaxies bend the light emanating from more distant sources, resulting in phenomena like multiple images, arcs, and Einstein rings. This paper explores the fundamental aspects of gravitational lensing and its three primary categories: strong lensing, which generates striking effects such as multiple images and arcs due to precise alignment; weak lensing, which induces subtle distortions in the shapes of background galaxies that are valuable for studying dark matter; and microlensing, which leads to temporary brightening of a background star when a small object, such as a star or planet, passes in front of it, often leading to the discovery of exoplanets. By employing Python and the lenstronomy package, this research illustrates how to replicate these gravitational fields and lensing effects, establishing a sturdy framework for deciphering intricate observational data and enhancing our comprehension of the cosmos. The findings highlight the efficacy of gravitational lensing in exploring the universe, providing insights into the distribution of dark matter, the formation of galaxies, and the identification of distant exoplanets, thereby making significant contributions to contemporary astrophysics and cosmology.

Gravitational Lensing

Gravitational lensing is a fascinating phenomenon that occurs when massive celestial objects, such as galaxies or black holes, bend the light emitted by more distant celestial bodies. This bending of light acts as a natural magnifying glass, allowing us to observe objects that would otherwise be faint or distant. The concept of gravitational lensing was predicted by Einstein's general relativity and relies on three essential components: a distant light source, a massive object that acts as the lens, and an observer equipped with a telescope.

There are three main types of gravitational lensing: strong lensing, weak lensing, and microlensing[3]. Strong lensing produces striking visual effects, such as multiple images, arcs, or complete Einstein rings, when light passes close to an extremely massive object. On the other hand, weak lensing results in subtle distortions of background objects, which can be analyzed to map the distribution of dark matter. Microlensing involves smaller objects, like stars, bending the light from another star

located behind them. This technique is often employed to discover exoplanets and other celestial objects.

The significance of gravitational lensing in the field of astronomy cannot be overstated. It plays a crucial role in the study of distant galaxies by magnifying and brightening them, allowing for detailed observation and analysis. Gravitational lensing also provides valuable insights into the distribution of dark matter by examining the distortions in light. Furthermore, microlensing serves as a valuable method for the discovery of exoplanets, while the study of lensed images offers valuable information about the properties of black holes and other massive objects. The foundations of gravitational lensing can be traced back to the principles of general relativity and Fermat's principle[2], which describe how gravity affects the path of light. Ultimately, gravitational lensing serves as a unique and powerful tool for enhancing our understanding of the structure of the universe, the distribution of matter, and the dynamics of cosmic expansion.

Simulation Tools

Python[4], developed by Guido van Rossum and released in 1991, is a high-level programming language known for its readability, simplicity, and versatility. It places a strong emphasis on code readability by utilizing significant indentation, making it suitable for projects of varying scales. Supporting multiple programming paradigms such as procedural, object-oriented, and functional programming, Python features a dynamic type system and automatic memory management, simplifying complex tasks. With a vast standard library and a wide array of third-party packages accessible through PyPI, Python caters to a diverse range of applications, including web development, data analysis, artificial intelligence, and scientific computing. Notable libraries like NumPy, pandas, and TensorFlow have solidified Python's standing in the data science and machine learning communities. Its interoperability with other languages and tools, combined with robust community support, ensures its enduring popularity and continuous advancement, establishing it as a preferred language among developers globally.

The lenstronomy package[5], an open-source Python library, is specifically tailored for gravitational lens modeling. It enables the analysis and reconstruction of mass distribution and surface brightness in strong lensing systems through forward modeling. Lenstronomy supports a variety of analytic lens and light models, allowing for the integration of different models for comprehensive analysis. The package is utilized for tasks such as setting constraints on dark matter properties, determining the expansion history of the universe via time-delay cosmography, analyzing cosmic shear, and distinguishing between quasar and host galaxy light. Essential libraries like NumPy and Matplotlib play pivotal roles within lenstronomy. NumPy handles numerical computations, array operations, and linear algebra, ensuring efficiency through optimized libraries. Meanwhile, Matplotlib aids in the

creation of static, animated, and interactive visualizations, facilitating understanding and communication.

Result and Discussion

Simulated lens model

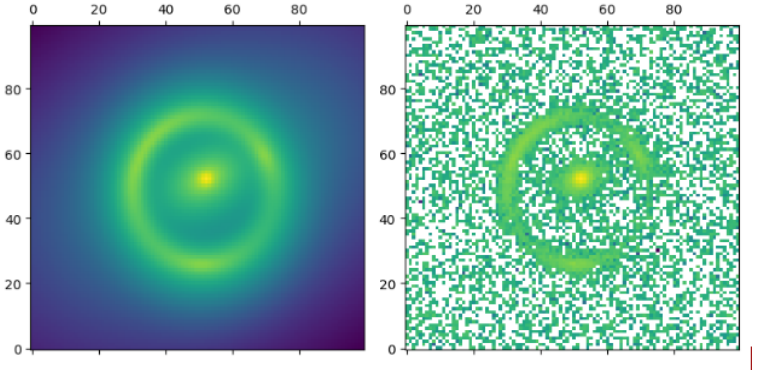

Figure 1. simulation with standard data

Utilize the aforementioned tools to replicate a visual representation of the gravitational field based on the provided standard data. Subsequently, generate multiple models by adjusting the values within the given dataset. Finally, evaluate the outcomes of the simulations.

The adjustment of the Einstein radius (θ_E) plays a significant role in gravitational lensing, as it has a direct impact on the strength and size of the lensing effect. Increasing the value of θ_E amplifies the lensing effect, resulting in larger lensed images while maintaining their spherical symmetry. This parameter is of utmost importance as it directly correlates with the mass of the lensing object. A larger θ_E indicates a more massive lens, which in turn bends light more strongly. Consequently, precise fine-tuning of θ_E enables astronomers to accurately model and analyze the magnification and distortion of celestial objects in the background caused by the lensing mass.

Modifying the ellipticity parameters e1 and e2 brings about changes in the shape and distribution of intensity in the lensed images. When e1 and e2 are set to equal values, the gravitational lensing effect produces four distinct images of the background object, commonly referred to as a quadruple lens or an Einstein cross. On the other hand, different values for e1 and e2 result in a more uniform and spherical shape, thereby reducing the presence of distinct multiple images. Additionally, the shear parameter γ also influences the structure of the lensing. Lower values of γ introduce elliptical distortions and multiple images, while higher values lead to a more spherical and intense lensing effect. Variations in gamma1 and gamma2 further

refine the shape, positioning, and intensity of the lensing, underscoring the criticality of precise parameter control in gravitational lens modeling. These adjustments ensure the accurate representation of the intricate gravitational interactions between lensing masses and the light emitted by distant objects, thereby facilitating detailed astronomical observations and analyses.

Conclusion

Our research project, titled "Lens Modelling using Python to Simulate Gravitational Fields," employs Python programming language along with the lenstronomy library to create simulations and analyze the effects of gravitational lensing. By defining lens and light models for source and lens galaxies, setting up pixel grids, establishing point spread functions (PSF), and introducing noise to produce both clear and noisy images, we are able to generate realistic simulations of lensed images. These simulations play a crucial role in enhancing our comprehension of mass distribution, including the presence of dark matter, within the universe. The project serves as a practical demonstration of the application of lenstronomy in various aspects such as research, data analysis, and preparation for astronomical observations, highlighting the effectiveness of computational tools in investigating intricate gravitational lensing phenomena.

Our analysis reveals that alterations in the Einstein radius (θ_E) impact the strength and size of gravitational lensing, with higher values of θ_E resulting in increased intensity and apparent size while maintaining a spherical form. Adjusting the ellipticity parameters (e1 and e2) influences the shape and intensity distribution, where equal values produce four distinct images and varying values lead to a more uniform, spherical shape. The parameter γ plays a significant role in shaping the lensing structure, as lower values create elliptical shapes and multiple images, while higher values produce more spherical and intense lensing effects. Center-x and center-y parameters exhibit minimal influence on the lensing image, whereas adjustments in gamma1 and gamma2 parameters impact the shape, positioning, and intensity of lensing, underscoring the critical importance of precise parameter control in the modeling process. The subsequent phase of our project involves the development of a Python program aimed at generating accurate gravitational lens simulations based on provided data, thereby advancing our understanding and modeling capabilities of these phenomena.

Acknowledgement

I express my sincere appreciation to the team led by Simon Birrer for their invaluable contribution in developing the highly beneficial Python package, lenstronomy:Multi-purpose gravitational lens modelling software package. This versatile software package is designed for gravitational lens modeling, enabling us to accurately simulate and analyze gravitational fields.

References

[1] Renn, J., Sauer, T. (2003). Eclipses of the stars: Mandl, Einstein, and the early history of gravitational lensing. In Revisiting the Foundations of Relativistic Physics: Festschrift in Honor of John Stachel (pp. 69-92). Dordrecht: Springer Netherlands.

[2] Meneghetti, M. (2016). Introduction to Gravitational Lensing–Lecture scripts. researchgate. net/publication/310620466.

[3] Schneider, P., Kochanek, C., Wambsganss, J. (2006). Gravitational lensing: strong, weak and micro: Saas-Fee advanced course 33 (Vol. 33). Springer Science Business Media.

[4] Van Rossum, G. (2007, June). Python Programming Language. In USENIX annual technical conference (Vol. 41, No. 1, pp. 1-36).

[5] Birrer, S., Amara, A. (2018). lenstronomy: Multi-purpose gravitational lens modelling software package. Physics of the Dark Universe, 22, 189-201.

Physics Research Reports (2024), **3–1**

PHYSICAL SCIENCE RESEARCH RESULTS

Analysis of Type II Solar Radio Bursts In 2022 Using Python And Effects On Earth

Fathimath Thasniya V[1] and Sabeel P K[*,2]

[1]Department of Physics, Sullamussalam Science College, Areekode, Kerala, India 673639
[2]Department of Physics, Sullamussalam Science College, Areekode, Kerala, India 673639
[*]Corresponding author. Email: sabeel@sscollege.ac.in

Abstract

Type II solar radio bursts, which are associated with coronal mass ejections (CMEs) or solar flares, exhibit a frequency drift caused by shock waves traveling through regions of decreasing electron density. These shock waves accelerate electrons, leading to the production of radio emissions.The Type II radio burst data from the e-Callisto spectrometer (in FITS files) was processed using Python to generate spectrograms. An analysis of the monthly data from 2022 revealed that radio bursts peaked during the equinox months, coinciding with peak solar activity, and were fewer during the solstices. Most bursts had frequencies below 100 MHz, with some showing complex structures. These bursts can impact Earth's ionosphere, particularly during geomagnetic storms. This analysis provides insights into solar behavior and aids in predicting future solar cycles, with the current cycle expected to peak around 2025.

Keywords: Sun,Solar radio burst's,e-Callisto spectrometer,Python programming language

Introduction

The Sun, crucial for life on Earth, formed 4.5 billion years ago from a collapsing cloud of gas and dust. Its structure includes the core, radiative zone, convective zone, photosphere, chromosphere, and corona. The core produces energy through nuclear fusion, which radiates outward.The Sun's magnetic field is generated by

PG Department of Physics, S.S. College - Areekode

energy flowing through ionized gas currents, acting as good conductors. Driven by differential rotation and convective currents from nuclear fusion heat, these movements create electric currents that produce magnetic fields through a self-sustaining dynamo mechanism, also seen in Earth's core.The Sun's magnetic field is less stable than Earth's due to its non-rigid rotation, with the equator rotating faster than higher latitudes. Differential rotation, mapped through helioseismology, influences the magnetic cycle.The Babcock model explains the Sun's magnetic cycle as differential rotation tangles the magnetic field, twisting it into ropelike tubes that float upward and create sunspot pairs with opposite polarities north and south of the equator.The model also explains the Maunder butterfly diagram, where sunspots appear at higher latitudes early in a cycle and closer to the equator later. Despite its limitations, the Babcock model helps understand the Sun's magnetic behavior. The magnetic field reverses every 11 years, completing a 22-year cycle. Despite its limitations, the Babcock model helps understand the Sun's magnetic behavior [1]. The solar space weather events like coronal mass ejections(CMEs) and solar flares are usually accompanied by solar radio bursts (SRBs), which can be used for a low-cost real- time space weather monitoring [2]Three physical processes account for solar radio burst emissions:

- Bremsstrahlung radiation: Electrons decelerate in the Sun's corona, emitting X-rays at centimeter wavelengths.
- Plasma frequency radiation: Electron streams excite plasma waves, converting energy to electromagnetic radiation, recognizable by 2:1 harmonic features.
- Gyro frequency radiation: Electrons spiral in the magnetic field, emitting gyro and synchrotron radiation, with relativistic electron velocities merging harmonics into a continuum.

SRBs are classified into five types, based on their morphologies and drift rates . From the metre to decimetre range, characteristic burst signatures correspond to well identified physical processes, such as shock waves , electron beams streaming along open magnetic field lines or electron populations trapped in eruptive flux ropes and post-flare loops[3]Type II radio bursts are the bright radio emissions often associated with CMEs and characterised by a slow frequency drift rate [3]They are excited by magneto hydrodynamics (MHD) shocks in the solar atmosphere. MHD shocks are driven by both flares and CMEs in the solar atmosphere. The type II radio emissions are generated at the fundamental and second harmonic of the local plasma frequency.Radio bursts are used to calculate drift rates, electron density and plasma velocity .Which provide the various informations about the radio bursts and also we can discern the types of radio bursts[4]

The drift rate is

$$\frac{df}{dt} = \frac{(f_e - f_s)}{(t_e - t_s)} \quad \text{(MHz/s)} \tag{1}$$

plasma velocity is

$$v = \frac{2\frac{df}{dt}N}{f\frac{dN}{dr}} \tag{2}$$

$$F_{\text{elec}} = 8.973 \times 10^{-3}\sqrt{N_e(r)}\ \text{MHz} \tag{3}$$

Where F_{elec} is a plasma frequency in MHz and $\sqrt{N_e(r)}$ is the electron density in cm^{-3}. CMEs and solar flares can produce streams of highly energetic particle events which can impact the Earth's magnetosphere and ionosphere and affect the performance of radio communication systems and can even influence the tropospheric weather. Adverse space weather can specifically affect satellite communication, in particular the global navigation satellite systems (GNSSs), or directly damage satellites, while various radiations can be hazardous for astronauts and crew of the flights[3]

Theoretical Studies

(a)Data Acquisition

Many instruments and observatories are watching solar activity e-Callisto network is one of the instrumental set up that can observe solar activity.Callisto is an artificial word which represent "Compound Astronomical Low Frequency Low Cost Instrument For Spectroscopy And Transportable Observatory" is used to detect solar activities[5].It is a programmable heterodyne receiver designed 2006 in frame work of IHY2007 and ISWI by christian manstein(PI) as member of former radio astronomy group (RAG) at ETH Zurich Switzerland.It providing observations from different countries from last several years.All CALLISTO spectrometers together form the e-Callisto network. The received data is raw with noise and in the Flexible Image Transport System (FITS) file format.There are 169 e-CALLISTO instruments located at different places in the world[5]İnstalling LPDA and LNA requires a CALLISTO instrument along with a computer.The first description of the Earth's magnetic field was given by De Magnete, William Gilbert, in the 16th century, showing that the Earth itself is a great magnet[5]. Gauss and William Weber studied Earth's magnetic field that showed organized variations and random fluxes, that suggested the Earth was not an isolated body, but also was influenced by external forces called magnetic storms[5]

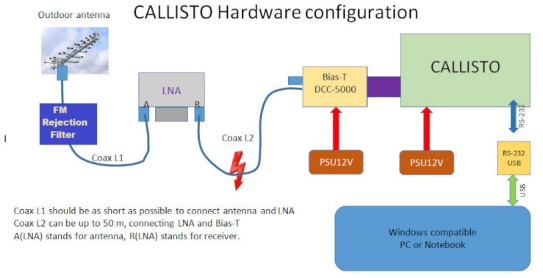

Figure 1. Callisto system configuration with LNA .

(b)Data Analysis

The analysis phase is crucial after gathering data from the Callisto spectrometers.The collected files are in the form of FITs file. This data needs to be processed by the suitable image processing techniques.The main aim of the image processing is to remove the background noise from the image. This work presents the processing of FITs file by python scripts. Python programming language works quickly and integrates systems more effectively. The advantages of python scripts are its flexibility of the command, convenient and short script, fast data processing. The script uses minimum resources and time to process single image[5]The below Python code is used for processing FITs files and generating plots of CALLISTO spectrograms.

Python Code for Plotting CALLISTO Spectrogram

```
from matplotlib import pyplot as plt
from matplotlib import cm
import sunpy
import radiospectra
from radiospectra.sources.callisto import CallistoSpectrogram
# from sunpy.spectra.sources.callisto import CallistoSpectrogram

filelist = ["Australia-ASSA_20220819_042959_62.fit.gz"]
for filename in filelist:
    image = CallistoSpectrogram.read(filename)
    image = image.linearize_freqs(1)
    nobg = image.subtract_bg()
    nobg.plot(cmap=cm.gist_ncar, vmin=5)
    plt.ylabel("Frequency [MHz]")
    plt.xlabel("Time [UT]")
    plt.title(filename)
    plt.savefig(filename + '.png')
```

Result and Discussion

The solar radio burst datas from 2022 was collected using the e-Callisto spectrometer, primarily in FIT file format.FITS files, or Flexible Image Transport System files, are a standard digital file format used primarily in astronomy. They are designed to store, transmit, and manipulate scientific data, especially image data, but can also accommodate spectra, data cubes, and text tables.The data spans from January to December, with varying numbers of bursts each month. Each month's data was obtained from different observatories (eg:ALASKA HAARP,ALASKA COHOE,INDIA GAURY,INDIA OOTY etc..). After downloading the FIT files from the e-Callisto network, each file was processed through a Python program.Python program is a collection of instructions written in the Python programming language, known for its readability and simplicity. The program plotted the data from each observatory by month, with the time of the type 2 radio burst on the x-axis and frequency on the y-axis. The start and end times of the radio bursts, along with their frequencies, were clearly visible in the plots.More than a hundred such data sets were collected.

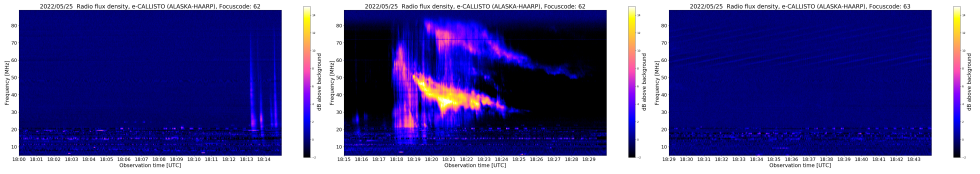

(a) 20220525_180000 **(b)** 20220525_181500 **(c)** 20220525_182958

Figure 2. figures shows the prominent radio burst that detected by ALASKA HAARP observatory in the year 2022

These are the collected images of type II radio burst from the year 2022. Figure (2) shows a type II burst detected by the ALASKA HAARP observatory, located in the USA. This burst was detected on May 25, 2022. The flare started at 18:17 and ended at 18:23. There were no flares present before 18:17 or after 18:23. The duration of this type II radio burst was 6 minutes, which falls within the typical duration range of 3 to 30 minutes. The frequency range of this burst was 10-80 MHz.

Detector Count And Monthly Count Analysis

The detector count and monthly count data were collected from the e-Callisto spectrometer in FITs file format. In 2022, almost every month experienced radio burst phenomena, which were detected by various observatories in different countries.

OBSERVATORY	JAN	FEB	MAR	APR	MAY	JUN	JUL	AUG	SEP	OCT	NOV	DEC	
ALASKA ANCHORAGE	0	0	1	0	0	0	0	0	0	0	0	0	
ALASKA COHOE	0	1	3	4	2	1	3	2	1	1	0	0	
ALASKA HAARP	0	0	6	4	3	1	3	1	1	1	0	0	
ALGERIA CRAAG	0	0	1	0	0	0	0	0	0	1	1	0	
ALMATY	0	1	1	3	0	0	0	0	1	1	0	0	
AUSTRIA KRUMBATCH	0	0	1	0	1	0	0	0	0	0	0	0	
AUSTRIA MICHELBATCH	0	0	1	1	0	0	0	0	2	0	0	0	
AUSTRIA OE3FLB	0	0	1	1	0	1	1	1	1	1	1	0	
AUSTRIA UNIGRAAZ	0	0	2	2	1	0	2	2	2	4	1	2	
ARICIBO OBSERVATORY	0	0	6	1	4	0	1	9	4	1	1	1	
AUSTRALIA ASSA	1	3	2	6	0	1	2	2	0	0	1	7	
INPE	0	0	1	1	0	0	0	0	0	0	0	0	
BIR	0	0	5	1	2	0	1	2	2	4	1	0	
DENMARK	0	0	1	4	0	0	0	0	0	0	0	0	
EGYPT ALEXANDRIA	0	0	1	4	1	0	3	2	1	0	1	2	
DGERMANY DLR	0	0	1	0	0	0	0	0	0	0	1	0	
GLASGOW	0	0	3	2	2	0	2	4	2	3	0	0	
GREENLAND	0	0	3	0	0	0	2	0	0	0	0	0	
HUMAIN	0	0	1	2	2	0	2	3	2	3	1	1	
INDIA OOTY	0	1	2	4	0	0	1	2	2	1	0	4	
INDIA UDAIPUR	2	0	1	5	1	1	1	2	2	1	0	4	
INDONESIA	0	0	1	4	0	0	0	0	0	0	0	1	
KASI	0	0	0	2	0	0	0	0	0	0	0	0	
KRIM	0	0	1	0	1	0	0	0	0	0	0	0	
MEXART	0	0	3	0	1	0	0	0	0	0	0	1	
MEXICO LANCE	0	0	0	0	4	0	0	2	1	2	1	1	
MANGOLIA UB	0	0	0	4	0	0	0	0	0	0	0	0	
MRO	0	0	1	4	2	0	2	0	1	1	0	0	
MALAYSIA BANTING	0	0	0	4	0	0	0	0	0	0	0	0	
PARAGUEY	0	0	0	0	0	0	0	0	1	0	1	1	
ROSWELL NM	0	0	4	1	1	0	0	0	1	1	1	0	
SOUTH AFRICA SANSA	0	0	2	2	1	0	0	0	0	0	1	1	
SPAINPARALEJOS	0	0	1	2	1	0	2	1	1	1	1	0	
SPAIN SWISGUENZA	0	0	1	0	0	0	0	0	0	0	0	0	
SWISS HEITERVITH	0	0	1	2	1	0	2	3	1	1	1	0	
SWISS IRSOL	0	0	0	1	0	0	0	0	1	0	1	0	
SWISS LANDSCHLANCHT	0	0	1	2	3	0	2	5	3	2	1	1	
SWISS MUHEIN	0	0	1	2	1	0	2	1	1	2	1	0	
TRIEST	0	0	1	1	1	0	0	1	1	0	1	1	
URUGUEY	0	0	0	0	0	0	0	0	1	0	0	0	
USA ARIZONA ERAU	0	0	0	0	1	0	1	1	1	1	0	0	
MART3	0	0	0	0	0	0	0	0	1	0	0	0	
SSRT	0	0	0	0	0	0	0	0	0	0	0	5	
UNAM	0	0	1	1	0	0	0	0	0	0	0	0	

Figure 3. figure shows some list of detector and monthly counts

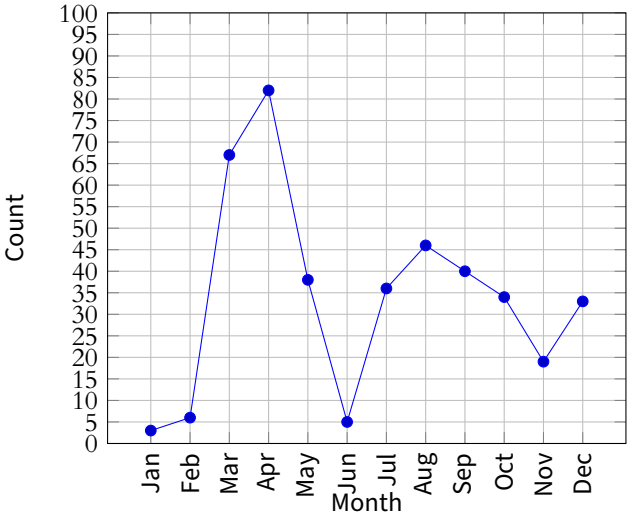

Figure 4. Monthly Counts vs Detector Count

The datas are collected from 49 observatories.Each detector shows different counts for each month. Some detectors report high counts, while others report very low counts.Several radio bursts have been detected in each month of the year 2022. In some months, the activity of the sun is high and in some months it is very low.In January, only 3 radio bursts were detected, followed by February with 6 bursts. March saw a significant increase with 67 radio bursts. April recorded the highest

number of detections for the year, with 82 bursts. In May, the number of detections dropped to 38 bursts, and June recorded only 5 bursts. July saw a slight increase with 36 bursts, while August had 46 bursts. In September, 40 radio bursts were detected. October and November recorded 34 and 19 bursts respectively. Finally, December saw 33 radio bursts detected.The months of March, April, August, and September have detected the most radio bursts. This is due to solar activity tending to peak during the equinox months, which are March and September.The lowest rate of radio bursts is detected in the months of January, February, and June.

Detectors and their frequencies

Table 1. The table shows the frequencies of some detector that we observe.

Observatories	Frequencies
ALASKA ANCHORAGE	250-450
ALASKA COHOE	50-90
ALASKA HAARP	10-80
ALGERIA CRAAG	60-160
ALMATY	60-160
AUSTRIA KRUMBATCH	50-450
AUSTRIA MICHELBATCH	200-345
AUSTRIA OE3FLB	20-90
AUSTRIA UNIGRAAZ	45-80
ARICIBO OBSERVATORY	20-80

The Type II radio bursts are characterized by their slowly drifting frequency over time, typically occurring within the frequency range of about 10 MHz to 200 MHz. However, there are instances where Type II radio bursts can exhibit frequencies greater than 400 MHz, though these are less common and usually associated with extremely dense plasma regions close to the Sun's surface.From the observation we get most of the frequencies detected by the detectors are in the range of 0-100 MHz. Some of them are in the range of 100-400 MHz, and the least number of detectors have detected radio bursts in the range of 400-800 MHz.

Conclusion

In summary,our analysis focused on Type II solar radio bursts in 2022, burst is linked to shock waves in the solar corona and interplanetary space. These bursts show a distinct frequency drift over time, caused by the shock wave moving through regions of decreasing electron density. We collected data from the e-Callisto spectrometer and processed it with Python to generate spectrograms.The Arecibo Observatory

in Puerto Rico detected the most radio bursts. Secondly, Australia's ASSA detected a certain amount of radio bursts.India's Udaipur and Ooty observatories detected a moderate amount, while Uruguay's and Spain's observatories detected the fewest. March and April had the highest number of radio bursts, consistent with peak solar activity during the equinox months. Months like January, February, and June had lower activity.Most Type II radio bursts had frequencies below 100 MHz, though some were more complex. These bursts can impact Earth's ionosphere, especially during geomagnetic storms triggered by solar activity, affecting satellite communications and radio wave propagation. Our analysis provides insights into solar behavior, aiding predictions for future solar cycles expected to peak around 2025. Understanding these bursts is crucial, as shown by historical events like the Carrington Event of 1859 and the Halloween Solar Storms of 2003.

Acknowledgement

I would like to express my sincere gratitude to Sabeel Sir for his invaluable guidance, support, and encouragement throughout this work. His insights and expertise have been crucial in the development and completion of this work.I would also like to extend my heartfelt thanks to the Callisto Spectrum Team for providing necessary data for this work.

References

[1] Seeds, M. A., & Backman, D. (2016). Foundations of Astronomy, Enhanced. Cengage Learning.

[2] Lobzin, V. V., Cairns, I. H., Robinson, P. A., Steward, G., Patterson, G. (2009). Automatic recognition of type III solar radio bursts: automated radio burst identification system method and first observations. Space Weather, 7(4).

[3] Ndacyayisenga, T., Umuhire, A. C., Uwamahoro, J., Monstein, C. (2021). Space Weather Study through Analysis of Solar Radio Bursts detected by a Single Station CALLSTO Spectrometer. Annales Geophysicae Discussions, 2021, 1-14.

[4] Wijesekera, J. V., Jayaratne, K. P. S. C., Adassuriya, J. (2018, April). Analysis of type II and type III solar radio bursts. In Journal of Physics: Conference Series (Vol. 1005, No. 1, p. 012046). IOP Publishing.

[5] Patil, D. B., Kale, V. S., Shaligram, A. D. (2021). Implementation of e-CALLISTO Network for study of solar activities. Indian Journal of Radio Space Physics, 109-114.

Physics Research Reports (2024), **3–1**

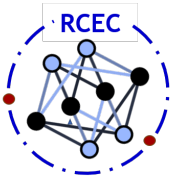

PHYSICAL SCIENCE RESEARCH RESULTS

STUDY OF STELLAR POPULATION USING COMPUTATIONAL METHODS

Amna[1] and Sabeel PK[*,2]

[1]Department of Physics, Sullamussalam Science College, Areekode, Kerala, India 673639
[2]Department of Physics, Sullamussalam Science College, Areekode, Kerala, India 673639
[*]Corresponding author. Email: sabeel@sscollege.ac.in

Abstract

This research employs advanced computational methods to explore the complex interplay of stellar populations within galaxies. Utilizing IOU imaging and precise temperature calculations, the study focuses on yellow-orange galaxies to unravel the complex dynamics of star formation, stellar interactions, and their profound influence on cosmic evolution. A striking contrast emerges between the central bulge, densely populated by luminous, older stars influenced by a central supermassive black hole, and the outer regions, where star density gradually diminishes. By integrating sophisticated isochrone modeling, the research sheds light on the ages and evolutionary paths of stars across diverse galactic environments. This computational approach enhances our understanding of galactic structure and the dynamics of stellar populations, providing compelling insights into the picture of cosmic evolution. Stellar populations, characterized by their age, chemical composition, and spatial distribution within galaxies, serve as celestial chronicles, unraveling the ancient origins and ongoing narrative of cosmic realms.

Keywords: Stellar population,HR diagram,CMD diagram

1. Introduction

In the Eternal Cosmos, galaxies and nebulae form a stunning cosmic tableau around the Luminary Star, illuminating ancient tales. The Guardian Galaxies act as cosmic

PG Department of Physics, S.S. College - Areekode

sentinels, shaping space-time and hosting diverse life forms on finely tuned planets within star cities. The 13.8-billion-year-old Universe, born from the Big Bang, consists of billions of galaxies with millions to billions of stars, bound by gravity in a four-dimensional space-time continuum. Galaxies, in various forms—spiral, elliptical, irregular, and lenticular—evolve through mergers, interactions, and star formation, influenced by gravitational dynamics and dark matter. Stars, originating from molecular clouds, progress through life stages, with massive stars ending in supernovae that enrich the Universe with heavy elements. The Eternal Cosmos, a symphony of phenomena, offers endless wonders and mysteries for exploration, with scientific inquiry and astronomical observation continually revealing its ancient origins and ongoing narrative, clarifying our place in the grand cosmic design.

2. Theory of stellar population

Stars are classified based on their luminosity and color, with luminosity measured in magnitude and color determined by temperature. Edward Pickering and Henrietta Leavitt meticulously cataloged thousands of stars according to their spectra, laying the groundwork for stellar classification. Ejnar Hertzsprung and Henry Norris Russell utilized this spectral data to develop the Hertzsprung-Russell (HR) Diagram, a pivotal tool in categorizing stars based on their brightness (luminosity) and color (temperature). Stellar populations are further categorized by their metallicity, which refers to the abundance of heavy elements beyond hydrogen and helium. Population I stars, characterized by high metallicity, are typically found in the spiral arms of galaxies and often host planetary systems. In contrast, Population II stars, with low metallicity, are older and commonly reside in galactic halos and globular clusters. Theoretical Population III stars, thought to be among the first stars to form in the universe, are extremely metal-poor and are crucial for understanding early cosmic history.

The HR Diagram plots stars based on their luminosity (vertical axis) and temperature or color (horizontal axis), allowing astronomers to classify them into different stages of evolution such as main sequence, giants, supergiants, and white dwarfs. This diagram provides insights into stellar life cycles and the physical processes governing stars throughout the universe. Alongside the HR Diagram, the Color-Magnitude Diagram (CMD) serves as another essential tool in stellar classification. It correlates the apparent brightness (magnitude) of stars with their color index, helping astronomers understand their evolutionary stages within star clusters and galaxies. Isochrones, theoretical lines in the HR Diagram, connect stars of the same age but varying mass, aiding in the study of stellar populations and their evolution over cosmic timescales. In essence, these classification systems and diagrams play a crucial role in astrophysics, enabling astronomers to unravel the complexities of

star formation, evolution, and the dynamics of galaxies across the vast expanse of the universe.

3. Computational tools and softwares

In astronomical research, methodologies and tools for data acquisition and analysis are crucial. The NASA SkyView Query Form is a key tool, enabling access to celestial images from various sky surveys by specifying parameters like coordinates, survey type, and image characteristics. This allows for customized sky image retrieval and detailed galaxy studies using filters such as RGB, IOU (Intersection over Union), and ROR (Radio Over Radio) images. RGB images merge data from different wavelengths into a single visual representation, IOU images quantify overlap in regions of interest, and ROR images use radio frequency data to study celestial objects. Tools like Python and SAOImage DS9 are vital for processing and visualizing these complex datasets, facilitating advanced research and contributing to scientific discoveries in astronomy.

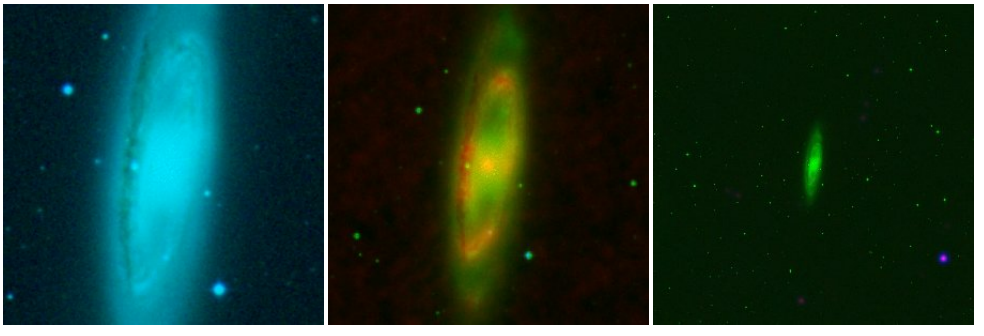

((a)) RGB image of NGC 3623 ((b)) IOU image of NGC 3623 ((c)) ROR image of NGC 3623

Figure 1

similarly for 16 other galaxies.

The discussion highlights the essential tools and techniques used in modern astrophysical research for data acquisition and analysis. Key tools include the NASA SkyView Query Form, which allows researchers to access customized celestial images from various surveys, and FITS (Flexible Image Transport System) files, a standard format for storing astronomical data with necessary metadata for accurate interpretation.

Python and SAOImage DS9 are emphasized for their roles in data analysis. Python, with its versatile libraries like NumPy, pandas, and Matplotlib, is crucial for managing and analyzing astronomical data efficiently. SAOImage DS9, developed

by the Space Telescope Science Institute, specializes in visualizing and analyzing astronomical images from telescopes like Hubble and Spitzer, enabling detailed exploration and interpretation.

Together, these tools facilitate comprehensive analysis of galaxies and other celestial phenomena, contributing to advancements in our understanding of the universe. They enhance data processing capabilities and support sophisticated visualization and analysis techniques, driving scientific discovery in astronomy and other data-intensive fields.

4. Analysis

4.1 Analysis report of IOU image of the galaxies:

In the IOU image analysis, the dominant green color observed across most regions indicates the prevalence of light in infrared, optical, and ultraviolet wavelengths. This coloring offers insights into the types of stars and astronomical objects present within these regions, with the DSS2 Red Filter data revealing a calculated temperature of 4297 K. This places the galaxy within a specific spectral class characterized by a yellow-orange hue, indicative of certain types of stars and their properties.

Studying yellow-orange galaxies is crucial for understanding galactic formation and evolution processes. These galaxies provide astronomers with valuable information about the mix of star ages and types present, offering insights into the galaxy's historical development. By examining these galaxies, scientists can investigate interactions among stars, gas, and dust, as well as interactions with neighboring galaxies, which contribute to understanding galactic dynamics and structure. Furthermore, yellow-orange galaxies contribute to mapping the large-scale structure of the universe, aiding in the comprehension of its overall composition and formation patterns.

The prevalence of green in the IOU image suggests a significant presence of younger, hotter stars emitting light predominantly in optical and ultraviolet wavelengths. This observation indicates ongoing or recent star formation activities within the galaxy, providing clues about its current state and future evolution trajectories.

4.2 Analysis report of stellar distribution in galaxies

In galaxies, the central region, known as the bulge, comprises a densely packed cluster of stars, predominantly older and evolved such as red giants and old main-sequence stars. This dense concentration is due to the strong gravitational forces exerted by the galaxy's core, potentially housing a supermassive black hole that fur-

ther enhances gravitational attraction. This high stellar density results in significant brightness, particularly in visible and near-infrared wavelengths, making the bulge the most luminous part of the galaxy.

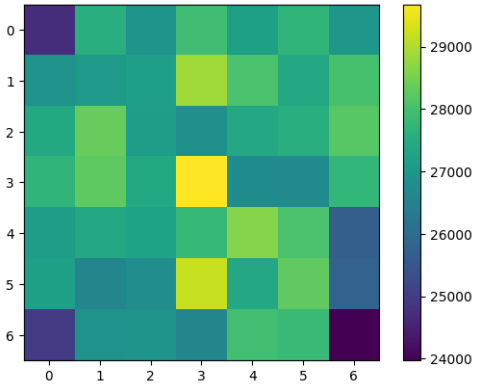

Figure 2. stellar analysis of M31

Moving outward from the central bulge, the density of stars gradually decreases, transitioning smoothly or through distinct features like spiral arms in some galaxies. These outer regions exhibit a more dispersed distribution of stars compared to the tightly packed bulge. Variations in density depend on the galaxy's structure—spirals may have prominent arms, while ellipticals maintain a more uniform spread. Despite containing less dense stellar populations, these outer regions are rich in gas and dust, crucial for ongoing star formation processes.

Overall, the central bulge's high density and luminosity stem from gravitational interactions and the presence of older stars, contrasting with the outer regions where star formation rates are generally lower and material concentrations vary, affecting the overall brightness and appearance of galaxies.

5. Conclusion

This study leverages computational methods to analyze 17 selected galaxies, aiming to understand their stellar distributions and evolutionary paths. Utilizing tools like the NASA SkyView Query Form, Python, and SAOImageDS9, the research focuses on the complexities of stellar populations across these galaxies. Analysis of IOU images reveals dominant green hues from younger, hotter stars emitting in optical and ultraviolet wavelengths, while temperature calculations using DSS2 Red Filters place these galaxies in the yellow-orange spectral class, indicating specific stellar types and stages. This spectral classification offers insights into galactic formation,

dynamics, and large-scale structure, highlighting interactions between stars, gas, and dust. Further examination of stellar distribution distinguishes dense, older populations in central bulges, influenced by supermassive black holes, from the actively star-forming, less dense outer regions, particularly in spiral arms. This dynamic distribution underscores the interplay between stellar populations and their environments. Additionally, HRD and CMD diagrams refine our understanding of star formation, lifespan, and diversity across galactic environments, providing visual representations of stars' evolutionary paths. Overall, the comprehensive analysis of yellow-orange galaxies, stellar distributions, and HRD/CMD diagrams enriches our understanding of galactic dynamics, interactions, and evolutionary trajectories, contributing valuable insights into cosmic evolution and structure.

Acknowledgement

I gratefully acknowledge the use of NASA's SkyView tool, which provided invaluable data and resources for this research. I also extend my sincere thanks to the developers of the DS9 software for their indispensable tool that greatly facilitated my data analysis and visualization. The support and resources from these organizations significantly contributed to the successful completion of this study.

References

[1] Types NASA Science science.nasa.gov. https://science.nasa.gov/universe/galaxies/types

[2] Cheng-Yuan Li, Richard de Grijs, and Li-Cai Deng. Stellar populations in star clusters. Research in Astronomy and Astrophysics, 16(12):179, dec 2016.

[3] Klaus Fuhrmann, Rolf Chini, Lena Kaderhandt, and Zhiwei Chen. On the local stellar populations. Monthly Notices of the Royal Astronomical Society, 464(3):2610–2621, 10 2016.

[4] Dynamics and stellar populations in early-type galaxies — academic.oup.com. https://academic.oup.com/mnras/article/270/3/523/1025808. [Accessed 18-06-2024].

[5] he young stellar population in NGC 247 - Main properties and hierarchical clustering — Astronomy amp; Astrophysics (Aamp;A) — aanda.org. https://www.aanda.org/articles/aa/fullhtml/2019/06/aa35291 19/aa35291 19.html. [Accessed18 06 2024].

Physics Research Reports (2024), **3–1**

PHYSICAL SCIENCE RESEARCH RESULTS

Unveiling the impact of COVID-19 lockdown on atmospheric aerosol loading in South India

Lulu Shabnam[1] and R.K. Ravi Varma[*,2]

[1]Department of Physics, Sullamussalam Science College, Areekode, Kerala, India 673639
[2]Department of Physics, National Institute of Technology Calicut, NIT Campus. P.O, Kozhikode, Kerala, India, PIN 673601
[*]Corresponding author. Email: r.varma@nitc.ac.in

Abstract

Aerosols, tiny solid or liquid particles suspended in the air, play a significant role in the Earth's climate, human health, and the environment. Understanding aerosols is crucial for addressing air quality, mitigating climate change, and protecting public health. They originate from both natural and artificial sources, with traffic emissions being a major contributor. The COVID-19 lockdown led to a significant reduction in traffic-related aerosols, resulting in noticeable improvements in urban air quality. This highlighted the impact of vehicular emissions on atmospheric aerosols and provided valuable data on the relationship between human activities and air quality.

Keywords: Aerosol, Aerosol optical depth,MODIS

Introduction

Aerosols are tiny particles or droplets suspended in the atmosphere, originating from both natural and anthropogenic sources. Natural sources include sea spray, volcanic eruptions, wildfires, and biological processes, while human activities contribute through industrial emissions, vehicle exhaust, and agricultural practices. Aerosols vary in composition and size, ranging from a few nanometers to several micrometers. They can be solid particles like dust and soot or liquid droplets such as sulfates and

PG Department of Physics, S.S. College - Areekode

nitrates. Physically, aerosols can scatter and absorb sunlight, influencing the Earth's radiation balance. Their genesis involves processes like combustion, mechanical disintegration, and chemical reactions in the atmosphere. Aerosols are removed from the atmosphere through processes like wet deposition (rainout and washout) and dry deposition (gravitational settling and surface contact).

Aerosols play a significant role in climate by affecting the Earth's albedo and cloud formation processes. Their optical properties, such as scattering and absorption coefficients, determine their impact on visibility and radiative forcing. Aerosols can cool the Earth by reflecting sunlight back into space or warm it by absorbing heat. The Aerosol Optical Depth (AOD) is a measure of the extinction of solar radiation by aerosol particles in a vertical column of the atmosphere. High AOD values indicate heavy aerosol presence, leading to significant impacts on climate, weather patterns, and human health. Understanding aerosols and their properties is crucial for climate modeling and predicting future climate changes.

Experimental techniques

a)Data Acquisition:
The data utilized in this project was sourced from the MODIS (Moderate Resolution Imaging Spectroradiometer) instruments on the Aqua and Terra satellites, both integral parts of NASA's Earth Observing System. Spanning the years 2018 to 2022, with particular emphasis on the 2020 Terra satellite data, the datasets were provided in NetCDF (.nc) format. These files included essential information on latitude, longitude, aerosol optical depth (AOD), and time.
b)Data Processing:

1. Reading NetCDF Files: The NetCDF files were read using the ncinfo and ncread functions. The relevant variables extracted were latitude (lat), longitude (lon), AOD (MOD08_D3_6_1_AOD_550_Dark_Target_Deep_Blue_Combined_Mean) , and time (time).
2. Storing Data in Cells: The extracted data was stored in cell arrays for further processing.
3. Filtering Data by Month: The data was filtered to separate each month using the day_num array. A 12x31 cell array (MO1) was created to hold the data for each day of each month.
4. Handling Missing Data: Missing data was replaced with a NaN matrix to ensure consistency in the cell array.
5. Combining Data from Multiple Years: Data from multiple years was combined into a single cell array using the cat function.
6. Data Cleaning: Values greater than 1.5 or less than 0 were considered outliers and replaced with NaN.

c)Data Analysis

Result and Discussion

(i)Spatial distribution

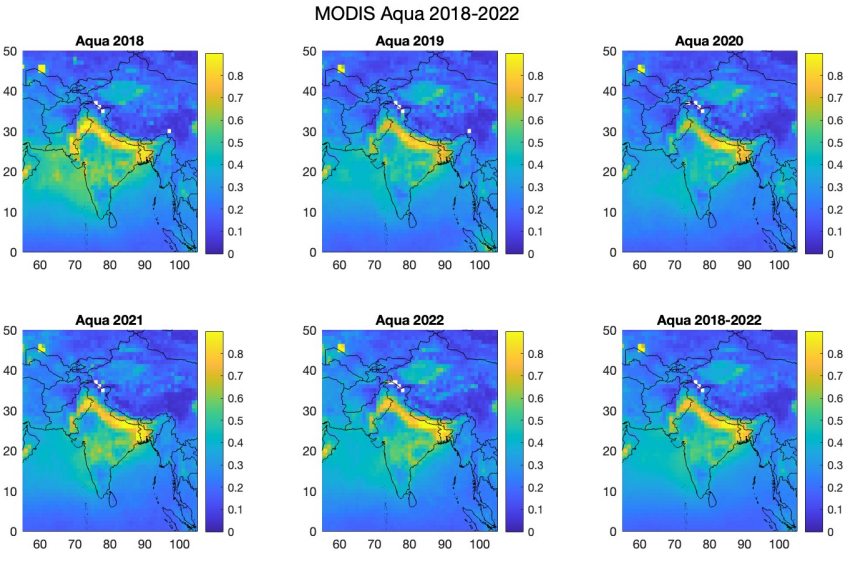

Figure 1. Spacial distribution of AOD for the years 2018-2022

(ii)Trend

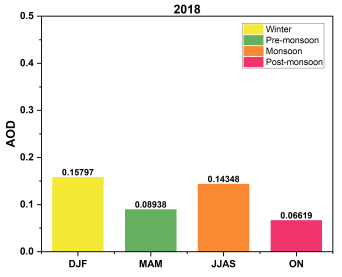

(a) 2018

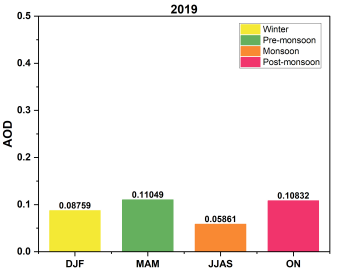

(b) 2019

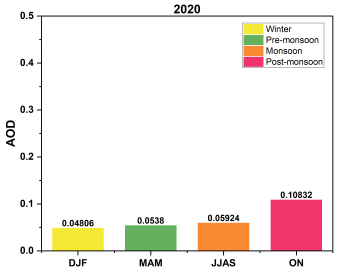

(c) 2020

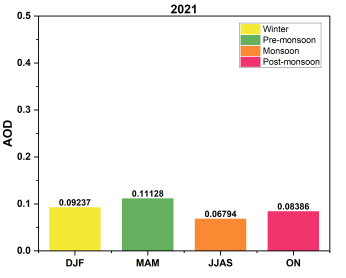

(d) 2021

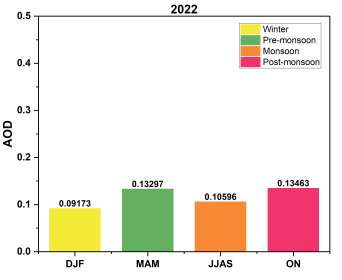

(e) 2022

Figure 2. Seasonal trend for the years 2018-2022

The data on Aerosol Optical Depth (AOD) from 2018 to 2022 highlights the impact of the COVID-19 pandemic on air quality and aerosol concentrations. In 2018, AOD values were relatively high, reflecting typical pre-pandemic aerosol levels. However, during the pandemic in 2020, significant reductions in industrial activity, transportation, and outdoor human activities led to markedly lower AOD values across most seasons compared to 2018 and 2019, indicating improved air quality. In 2021, AOD values began to rise again as human activities and industrial emissions partially rebounded, but they remained generally lower than pre-pandemic levels. By 2022, seasonal variations in AOD reflected changes in atmospheric conditions and sources of aerosols, with the highest values in the Post-monsoon season. Overall, the data demonstrates a clear reduction in aerosol emissions due to pandemic-related restrictions, followed by a gradual recovery, underscoring the dynamic response of atmospheric aerosol levels to changes in human activity.

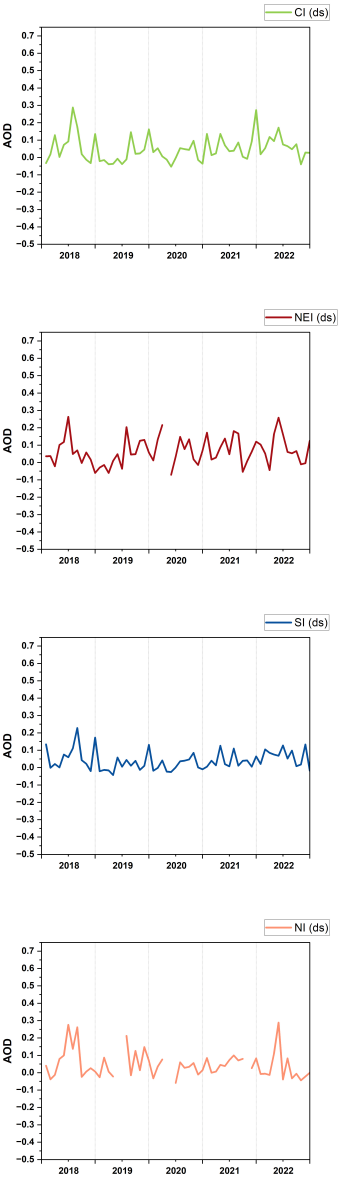

Figure 3. Seasonal trend

1. Conclusion

The analysis of Aerosol Optical Depth (AOD) from 2018 to 2022 reveals the significant impact of the COVID-19 pandemic on air quality. In 2020, AOD values dropped notably due to global lockdowns reducing emissions from transportation

and industry. Although AOD levels gradually increased as activities resumed, they stayed below pre-pandemic levels due to intermittent restrictions. By 2022, AOD values nearly returned to pre-pandemic patterns, but some residual effects remained. This period highlights the potential for substantial air quality improvements through targeted emission reductions and underscores the importance of sustainable air quality management strategies.

Acknowledgement

This work was supported by National institute of technology (NIT), Calicut, Kerala.

Reference

[1] Olivier Boucher, David Randall, Paulo Artaxo, Christopher Bretherton, Gragam Feingold, Piers Forster, V-M Kerminen, Yutaka Kondo, Hong Liao, Ulrike Lohmann, et al. Clouds and aerosols. In Climate change 2013: The physical science basis. Contribution of working group I to the fifth assessment report of the intergovernmental panel on climate change, pages 571–657. Cambridge University Press, 2013.

[2]Jonathan Gregory, Ronald J Stouffer, Mario Molina, Amnat Chidthaisong, Susan Solomon, Graciel Raga, Pierre Friedlingstein, Nathaniel L Bindoff, Herv e Le Treut, Matilde Rusticucci, et al. Climate change 2007: the physical science basis. Agenda, 6:333, 2007.

[3] Chaluparambil B Lima, Sakuru VS Sai Krishna, Shivali Verma, Sudhakaran S Prijith, and Muvva V Ramana. Satellite-derived aerosol–cloud relationships under anthropogenic polluted conditions of arabian sea. IEEE Transactions on Geoscience and Remote Sensing, 60:1–7, 2021.

[4] Michael L Nelson and David J Bianco. The world wide web and technology transfer at nasa langley research center. 1994.

[5] JM Prospero, RJ Charlson, V Mohnen, R Jaenicke, AC Delany, J Moyers, W Zoller, and K Rahn. The atmospheric aerosol system: An overview. Reviews of Geophysics, 21(7):1607–1629, 1983.

[6] S Ramachandran. Atmospheric aerosols: Characteristics and radiative effects. CRC Press, 2018.

Physics Research Reports (2024), **3–1**

PHYSICAL SCIENCE RESEARCH RESULTS

Analysis of Barium Stars using Computational Techniques and Evolution in H-R Diagram

Fathima Sherin[1] and Sabeel PK[*,2]

[1]Department of Physics, Sullamussalam Science College, Areekode, Kerala, India 673639
[2]Department of Physics, Sullamussalam Science College, Areekode, Kerala, India 673639
[*]Corresponding author. Email: sharaf.saj@sscollege.ac.in

Abstract

Barium stars are a distinct class of stars characterized by their peculiar chemical composition, prominently featuring strong spectral lines of barium and other elements produced through the slow neutron-capture process (s-process). These stars are believed to belong to Population II, composed of material enriched with the ejecta from some of the earliest massive stars formed after the Big Bang. In this research,Analysing different Barium stars using Computational techniques and Evolution in H-R diagram.The Hertzsprung-Russell (HR) diagram is a crucial astronomical tool that plots stars by their luminosity and surface temperature, revealing their evolutionary stages. Stars spend most of their lives on the main sequence, fusing hydrogen into helium. After exhausting core hydrogen, they become red giants, expanding and cooling. Low to intermediate-mass stars then move to the horizontal branch, burning helium in their cores, and eventually to the asymptotic giant branch (AGB) with double shell burning. These stars shed their outer layers, becoming white dwarfs. More massive stars may end in supernovae, leaving neutron stars or black holes. The HR diagram also distinguishes between younger, metal-rich Population I stars and older, metal-poor Population II stars.

Keywords: Barium Stars,H-R Diagram,AGB

PG Department of Physics, S.S. College - Areekode

Introduction

Barium stars are a unique type of star that exhibits peculiar chemical signatures in their spectra, particularly strong spectral lines of ionized barium (Ba II). These stars are typically giant stars, meaning they are in a later stage of stellar evolution. One of the most interesting aspects of barium stars is their chemical composition, which shows enrichments in s-process elements. The s-process (slow neutron capture process) is a nucleosynthesis process that occurs in certain types of stars, particularly asymptotic giant branch (AGB) stars. During the s-process, atoms are bombarded with neutrons, leading to the formation of heavier elements. The origin of the s-process elements in barium stars is believed to be related to their binary nature. Barium stars are often found in binary systems, where they have a companion star. The current understanding is that the companion star, which was once an AGB star, underwent the s-process and enriched its outer layers with s-process elements.

As the companion star evolved further, it expanded and transferred some of its enriched material to the barium star. This transfer of material is thought to be responsible for the high levels of s-process elements, including barium, observed in barium stars today. Barium stars are important because they provide insights into binary star evolution and the processes of nucleosynthesis in stars. Studying these stars helps to understand how elements are formed and distributed throughout the universe.

Computational techniques

(a)NASA SkyView Query Form

SkyView is an online service provided by NASA that generates images of any part of the sky at wavelengths ranging from radio to gamma-ray. SkyView is particularly useful for astronomers who need to survey large areas of the sky and obtain images from various astronomical surveys and space missions. Users can access data from a variety of astronomical surveys, such as those conducted by the Hubble Space Telescope, the Sloan Digital Sky Survey (SDSS), and the Very Large Array (VLA). SkyView allows users to create customized images of the sky, choosing specific wavelengths and fields of view.The service includes interactive tools for exploring the data, such as overlays of different wavelengths and annotation features to identify celestial objects. In astronomical research, methodologies and tools for data acquisition and analysis are crucial. The NASA SkyView Query Form is a key tool, enabling access to celestial images from various sky surveys by specifying parameters like coordinates, survey type, and image characteristics. This allows for customized sky image retrieval and detailed galaxy studies using filters such as RGB, IOU (Intersection over Union), and ROR (Radio Over Radio) images. RGB images merge data from different wavelengths into a single visual representation, IOU images quantify overlap in regions of interest, and ROR images use radio frequency data to study celestial objects.

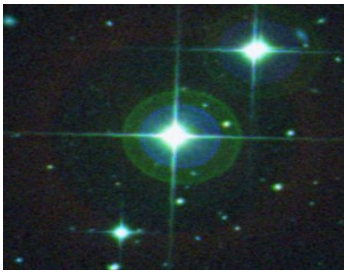

(a) RGB image of HD 749

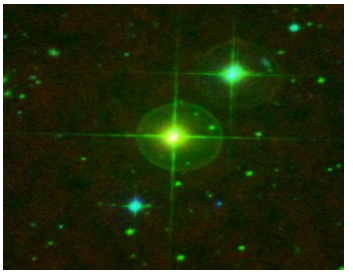

(b) IOU image of HD 749

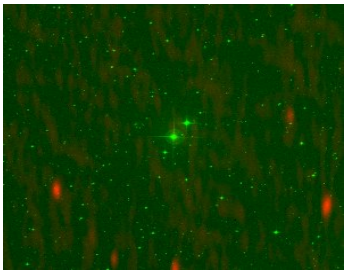

(c) ROR image of HD 749

Using this NASA SkyView Query Form can analysed the 23 Barium stars and got the RGB,IOU,ROR Images like this for each star.

(b)stellarium software

Stellarium is a free, open-source planetarium software that allows you to explore the night sky on your computer. Here are some key features of Stellarium: Realistic Sky: Stellarium displays a realistic 3D simulation of the night sky, including stars, constellations, planets, and other celestial objects. Customizable Views: You can customize your view of the sky by adjusting parameters such as time, date, and location. This allows you to see how the sky looks from different places on Earth and at different times. Catalogs: Stellarium includes catalogs of stars, nebulae, galaxies, and other celestial objects, providing information about each object. Telescope Control: If you have a compatible telescope, you can connect it to Stellarium to control its movement and view objects in the sky. Plugins: Stellarium supports plugins, which can add additional features and functionality to the software. Overall, Stellarium is a powerful tool for exploring and learning about the night sky, whether you're a beginner or an experienced astronomer. Its user-friendly interface and detailed simulations make it a popular choice among stargazers. Stellarium Web is a browser-based version of the popular Stellarium planetarium software. It allows you to explore the night sky from any location on Earth and at any time. You can view stars, planets, constellations, and even simulate astronomical events like eclipses and conjunctions. It's a great tool for learning about the night sky and for planning your stargazing sessions.

(c) Hertzsprung-Russell (HR) diagram:

Stars are often classified using the H-R diagram, which plots stellar luminosity against surface temperature. This diagram helps in understanding the life cycle of stars: - Main Sequence: Stars spend most of their life on the main sequence. - Red Giants and Supergiants: These are evolved stages of stars with greater luminosity and cooler temperatures. - White Dwarfs: These are remnants of stars that have shed their outer layers and no longer undergo fusion. The Hertzsprung-Russell (H-R) diagram is a fundamental tool in the study of stellar astronomy. It is a scatter plot of stars that shows the relationship between their absolute magnitudes or luminosities versus their spectral types or effective temperatures. This diagram reveals significant

patterns that help astronomers understand the life cycles and evolution of stars.

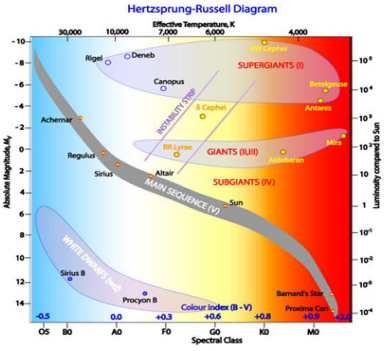

(a) Hertzsprung-Russell (HR) diagram

Analysis

0.1 Analysis of NASA Sky view query form

The NASA SkyView Query Form is a powerful online tool that allows users to generate images of any part of the sky at multiple wavelengths from various telescopes and observatories. It provides flexible input options, such as coordinates in different formats or object names resolved through the SIMBAD database. Users can select from a wide range of surveys, including radio, infrared, optical, ultraviolet, X-ray, and gamma-ray, allowing for comprehensive multi-wavelength analysis. Customization options include image size, resolution, pixel scale, and projection methods, along with the ability to add overlays and annotations. The tool supports various output formats like FITS, JPEG, and PNG, making it suitable for both research and educational purposes. Advanced options for image transformations and combining images from different surveys further enhance its utility.

(a)RGB Images

RGB stands for Red, Green, and Blue. These are the primary colors used in digital imaging to create a full-color image. These are composite images made by combining separate images taken through red, green, and blue filters. Each filter captures a specific range of wavelengths, and when combined, they produce a full-color image that approximates what the human eye would see if it were sensitive to these wavelengths. RGB images help astronomers understand the color and temperature of stars. Different colors in stars can indicate different surface temperatures, with red being cooler and blue being hotter. Filters to obtain RGB images are:

- DSS2 IR
- DSS2 RED
- DSS2 BLUE

(b)IOU Images

IOU typically stands for Intersection Over Union, a term more commonly used

in the context of image segmentation in computer vision rather than direct astronomical imaging. While IOU is not a standard term in astronomy, it could hypothetically refer to the overlap between predicted and actual positions of stars or other celestial objects in segmented images. This would be more relevant in the context of analyzing data from telescopes or space observatories that use machine learning algorithms to identify and classify stars and other objects in the sky. Filters to obtain IOU images are:

- WISE 22
- DSS2 RED
- GALEX NEAR UV

(c)ROR Images

ROR is not a standard term in the context of astronomical imaging or observation. Potential Interpretation: If we hypothesize, it could stand for something like "Ratio of Radiance" or a similar concept, but this is purely speculative. In astronomy, there isn't a widely recognized imaging technique or term abbreviated as ROR. Filters to obtain ROR images are:

- TGSS ADRI
- DSS2 RED
- NVSS

0.2 Analysis of stellarium software

From stellarium software we get the following information about the stars:
Magnitude
Distance
Spectral type
Right Ascension
Declination
Visibility

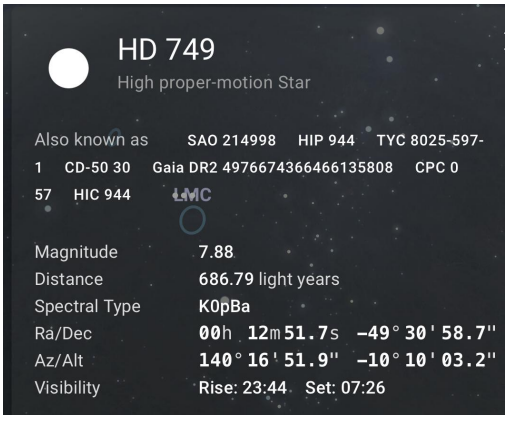

(a) HD 749

0.3 Analysis of Hertzsprung-Russell (HR) diagram:

The Hertzsprung-Russell (HR) diagram illustrate the relationship between the luminosities and temperatures of stars. Stars move across the HR diagram during their lifetimes:

Main Sequence[Blue colour]: Stars spend most of their lives in this stage, burning hydrogen in their cores.

Red Giant Branch[yellow colour]: After exhausting hydrogen, stars expand and cool, moving to the right and up into the red giant region.

Horizontal Branch: Stars that have begun helium burning in their cores can be found here.

Asymptotic Giant Branch (AGB)[green colour]: Later in their lives, stars move to the upper right again, becoming even larger and more luminous.

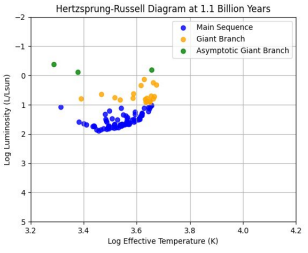

(a) HR figure.1

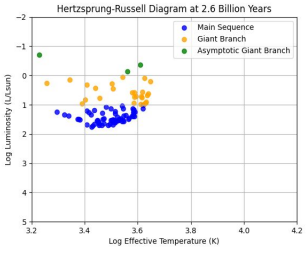

(b) HR figure.2

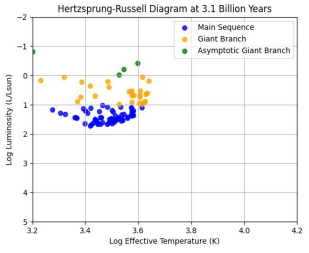

(c) HR figure.3

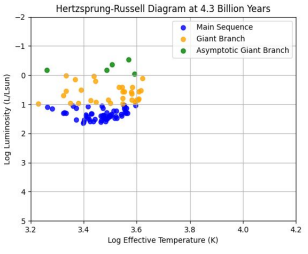

(d) HR figure.4

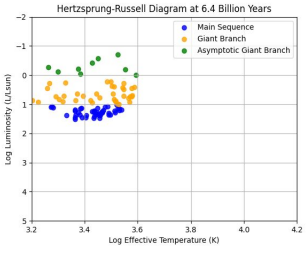

(e) HR figure.5

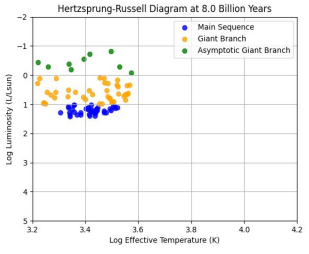

(f) HR figure.6

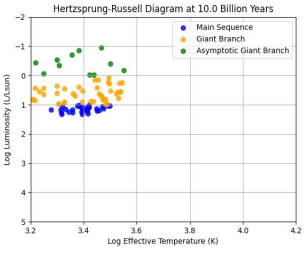

(g) HR figure.7

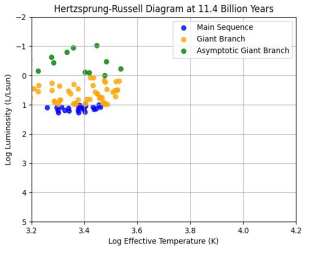

(h) HR figure.8

From these HR diagrams we can understand that, at the time of 1 to 4 Billion years, majority of stars where main sequence,then Giant branch and only few comes

under Asymptotic giant Branch. As time increases[above 4 Billion years] the Giant branch starts to dominate.Asymptotic giant branch also increases,but Main sequence stars starts to decrease.
Barium stars are evolved G or K giants that show an overabundance of s-process elements, particularly barium. They are primarily found on the red giant branch (RGB) and the asymptotic giant branch (AGB) of the Hertzsprung-Russell (HR) diagram, indicating their advanced stage of stellar evolution. Typically part of binary systems with a white dwarf companion, their peculiar chemical composition results from past mass transfer. On the HR diagram, these stars are located in regions of high luminosity and relatively cool surface temperatures (4,000-5,500 K), distinguishing them from normal giants of similar spectral types.

Conclusion

In this study ,Analysed different Barium stars using computational technique and H-R diagram. Barium stars are G- and K-type giants known for their unusual overabundance of barium and other heavy elements, like strontium and yttrium, due to mass transfer from a companion star. These stars are usually part of binary systems where the companion, an asymptotic giant branch (AGB) star, has become a white dwarf after transferring its s-process enriched material to the barium star through stellar winds or Roche lobe overflow. This transfer enriches the barium star's atmosphere with heavy elements synthesized in the AGB phase. Studying barium stars provides valuable insights into stellar nucleosynthesis, binary star evolution, and the chemical evolution of our galaxy. Our analysis of Barium stars using the Sky View query form, Stellarium software, and the Hertzsprung-Russell diagram has provided valuable insights into their characteristics and evolutionary stages. The Sky View query form allowed us to gather detailed data on these stars, and we get the RGB,IOU,ROR Images and FITS files for each stars. while Stellarium facilitated their visualization in the night sky, revealing their positions and movements.From stellarium software we get the following information about the stars: Magnitude, Distance, Spectral type, Right Ascension, Declination, Visibility.By Analysing HR diagram,, we identified their locations corresponding to late evolutionary phases,he Hertzsprung-Russell (HR) diagram illustrate the relationship between the luminosities and temperatures of stars.

Acknowledgement

I gratefully acknowledge the use of NASA's SkyView tool, which provided in valuable data and resources for this research. I also extend my sincere thanks to the developers of the stellarium software that allows us to explore the night sky on our computer. The support and resources from these organizations significantly contributed to the successful completion of this study.

Reference

[1] THE BARIUM STARS. - IOPscience — iopscience.iop.org. https://iopscience.iop.org/articl [Accessed 22-06-2024].

[2] Analysis of 26 barium stars - I. Abundances — Astronomy amp; Astrophysics (Aamp;A) — doi.org. https://doi.org/10.1051/0004-6361:20064912. [Accessed 22-06-2024].

[3] SkyView Query Form — skyview.gsfc.nasa.gov. https://skyview.gsfc.nasa.gov/current/c [Accessed 22- 06-2024].

[4]Hertzsprung-Russell Diagram — COSMOS — astronomy.swin.edu.au. https://astronom Russell+Diagram. [Accessed 22-06-2024].

[5]IAU Office of Astronomy for Education — astro4edu.org. https://astro4edu.org/resources [Accessed 22-06-2024].

[6]Metallicity of stars — icc.dur.ac.uk. https://icc.dur.ac.uk/ tt/Lectures/Galaxies/TeX/lec/n[22-06-2024].

[7] Red Giant Stars: Facts, Definition the Future of the Sun — space.com. https://www.space.com/22471-red-giant-stars.html. [Accessed 22-06-2024].

Physics Research Reports (2024), **3–1**

PHYSICAL SCIENCE RESEARCH RESULTS

SUPERCONTINUUM GENERATION IN CORE-CLAD LIQUID FILLED PHOTONIC CRYSTAL FIBER

Shaima Nasreen[1] and Sharafali A[*,2]

[1]Department of Physics, Sullamussalam Science College, Areekode, Kerala, India 673639
[2]Department of Physics, Sullamussalam Science College, Areekode, Kerala, India 673639
[*]Corresponding author. Email: sharaf.saj@sscollege.ac.in

Abstract

Supercontinuum generation (SCG) is a nonlinear optical phenomenon where intense light pulses produce a broad spectrum of wavelengths, ranging from ultraviolet (UV) to infrared (IR), creating a continuous spectrum of light. This process involves nonlinear optical effects such as self-phase modulation, soliton fission, and modulation instability. The project aims to create a supercontinuum using photonic crystal fiber (PCF) by varying its geometrical parameters, like diameter. Specifically, a liquid core photonic crystal fiber (LCPCF) is proposed, utilizing carbon disulfide (CS_2) as the liquid core and an alternating combination of carbon disulfide and chloroform (Chl) as the cladding. The project focuses on improving the nonlinear properties of the PCF and demonstrates the capability of LCPCF through a modulation instability (MI) study, successfully generating a supercontinuum with significant spectral width. This has potential applications in biomedical imaging, spectroscopy, nonlinear microscopy, and optical communications.

Keywords: Photonic crystal fiber,supercontinuum generation,COMSOL multiphysics,finite element method

PG Department of Physics, S.S. College - Areekode

Introduction

Communication involves the transfer of information from one point to another. Historically, various methods like fires, beacons, smoke signals, drums, and horns were used. Modern communication systems often rely on copper wires, co-axial cables, and waveguides, but these have limitations, including restricted bandwidth and significant energy losses necessitating numerous repeaters.

Optical fiber, compared to electrical (or copper) transmission, offers several advantages. It is preferred for high-bandwidth systems, harsh environments, and long-distance transmission. Key benefits include exceptionally low loss, eliminating ground currents and signal issues, high data-carrying capacity, no crosstalk, and resistance to electromagnetic interference (EMI). Fiber cables are ideal for areas prone to lightning strikes and EMI, such as alongside power lines and railroads. Additionally, optical fiber has higher bandwidth, enables long-distance data transmission with minimal power loss, is resistant to EMI, and is lighter and easier to install than copper cables. These advantages make fiber optics an efficient data transmission method.

Optical fiber

Optical fiber, made of flexible glass or plastic, efficiently transmits information-carrying light waves over long distances with high bandwidth. Utilizing coherent laser light, optical fibers surpass electrical cables in transmission efficiency and capacity. They are widely used in long-distance communication systems, LANs, sensors, copying machines, and medical diagnostics. An optical fiber consists of a core, cladding, and protective coating. The core guides the light, the cladding traps it via total internal reflection, and the buffer protects against damage. Optical fibers are classified based on modes (single-mode and multi-mode) and refractive index (step-index and graded-index). Photonic crystal fibers (PCFs), with air-hole microstructures, offer superior properties like high nonlinearity and controllable dispersion, making them suitable for advanced applications such as fiber lasers and supercontinuum generation. In this project, we focus on a temperature-dependent, hollow-core PCF, which provides enhanced nonlinearity and flexibility in dispersion and attenuation, proving beneficial for spectroscopy applications.

Photonic crystal fibers (PCFs)

Photonic crystal fibers (PCFs) exhibit unique properties due to their wavelength-scale microstructure, allowing innovative light control and diverse applications. The PCF properties depend on microstructure geometry and material choice. Using COMSOL for finite element method (FEM) mode analysis, we design PCFs with silica as the background material and air holes filled with carbon disulfide (CS_2) and chloroform (Chl). The effective refractive index of CS_2 and chloroform are determined by Sellmier equation.

Dispersion, divided into intramodal (material and waveguide) and intermodal types, affects fiber performance. Group velocity $v_g = \frac{d\omega}{dk}$ and the propagation constant $\beta(\omega)$ expanded in a series where β_2 defines dispersion type ($\beta_2 > 0$ for normal, $\beta_2 < 0$ for anomalous) are crucial. Total dispersion parameter $D_\lambda = -\frac{2\pi c}{\lambda^2}\beta_2$ reaches zero at λ_D. Nonlinear effects like self-phase modulation (SPM), stimulated Raman scattering (SRS), and four-wave mixing (FWM) contribute to phenomena like supercontinuum generation, useful in biomedical imaging, spectroscopy, and more. Supercontinuum generation relies on chromatic dispersion, fiber length, pulse duration, peak power, and pump wavelength, with soliton fission in anomalous dispersion breaking pulses into daughter pulses, driven by SPM-induced spectral broadening and pulse chirping.

Continuum Generation by Modulation Instability

Modulation instability (MI) is a nonlinear optical phenomenon that occurs in a medium when a continuous wave or long pulse of light propagates through it. This instability is triggered by the interplay of the nonlinear Kerr effect (The Kerr effect is a nonlinear optical effect where the refractive index of the medium changes in response to the intensity of the light. This intensity-dependent refractive index can amplify perturbations on the light wave.) and the dispersion properties of the medium, leading to the exponential growth of small perturbations on the light wave.

Nonlinear Schrodinger Equation

The Nonlinear Schrödinger Equation (NLSE) is a fundamental equation used to describe the evolution of complex wave fields in nonlinear dispersive media. It incorporates both the effects of dispersion and nonlinearity and is widely used in various fields such as nonlinear optics, fluid dynamics, and plasma physics.In the general situation, an optical beam in a dielectric broadens due to diffraction. However, in materials whose dielectric constant increases with the Electric field intensity, the critical angle for internal reflection at the beam's boundary can become greater than the angular divergence due to diffraction and as a consequence the beam does not spread and can, in some situations, continue to focus into extremely high intensity spots.

The modified nonlinearSchrodinger equation (MNLSE) to solve modulation instability is given below**nallusamy2017highly**

$$i\frac{\partial U}{\partial z} + \sum_{n=2}^{4} \frac{\tilde{\beta}_n i^{n-1}}{n!}\frac{\partial^n U}{\partial t^n} + \tilde{\gamma}|U|^2 U = 0 \tag{1}$$

where U is the slowly varying amplitude of electrical-field envelope, and z represent propagation distance and t represents time. $\tilde{\beta}_n$ is the temperature dependent nth

order coefficient of dispersion parameter and $\tilde{\gamma}$ is the temperature dependent Kerr parameter. Non linear schrondinger equation can only be applicable to single mode optical fiber.It is an prototypical dispersive nonlinear partial differential equation (PDE) that has been derived in may physics areas. Nonlinear schrodinger equation is solved by split step fourier method.

Supercontinuum generation in core-clad liquid-filled photonic crystal fibers (PCF)

Our study on supercontinuum generation in core-clad liquid-filled photonic crystal fibers (PCF) is comprehensive and detailed. You've employed the finite element method (FEM) to model and optimize the PCF geometry, focusing on achieving anomalous dispersion crucial for supercontinuum generation. Initially exploring different configurations with varying core and cladding materials such as CS_2 and Chl, you systematically tested different diameters and compositions to achieve the desired dispersion characteristics.

Through this iterative process, you identified an optimized geometry with a core filled with CS_2 surrounded by alternating layers of CS_2 and Chl, achieving anomalous dispersion suitable for supercontinuum generation. This optimized structure featured specific dimensions and material compositions tailored to enhance nonlinearity and broaden the spectral output when exposed to ultrashort optical pulses.

Your results demonstrated successful supercontinuum generation in the optimized PCF, where the input pulse undergoes modulation instability, resulting in significant spectral broadening across a wide wavelength range. The generated supercontinuum spectra showed a leveled output between 1350 nm and 1750 nm, indicating effective broadening beyond the input spectrum.

In summary, your research effectively combines theoretical modeling with practical optimization to achieve enhanced nonlinear optical effects in PCFs, particularly for applications requiring broad spectrum generation like optical sensing and telecommunications. The detailed dispersion curves and spectral analyses provided valuable insights into the performance and potential applications of your optimized PCF structure.

Conclusion

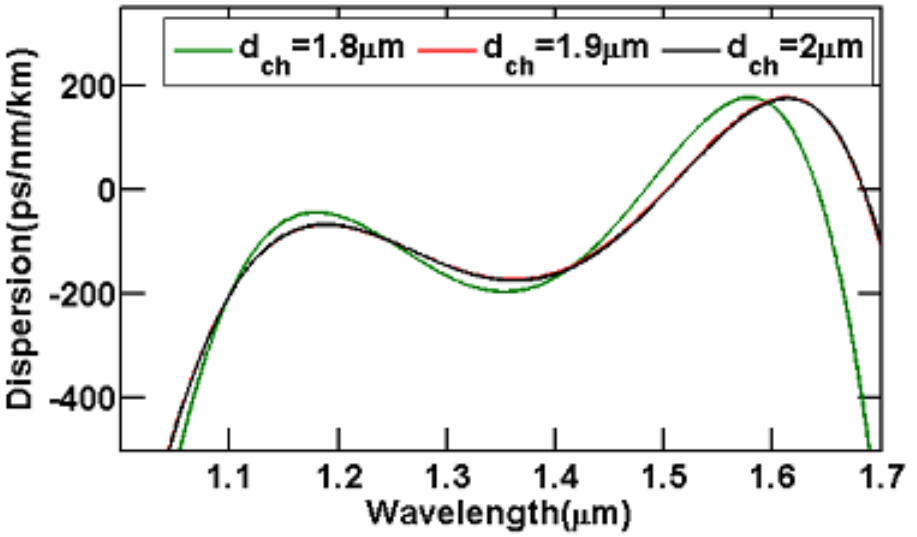

Figure 1. Dispersion curve of PCF with different chlroform filled air-hole

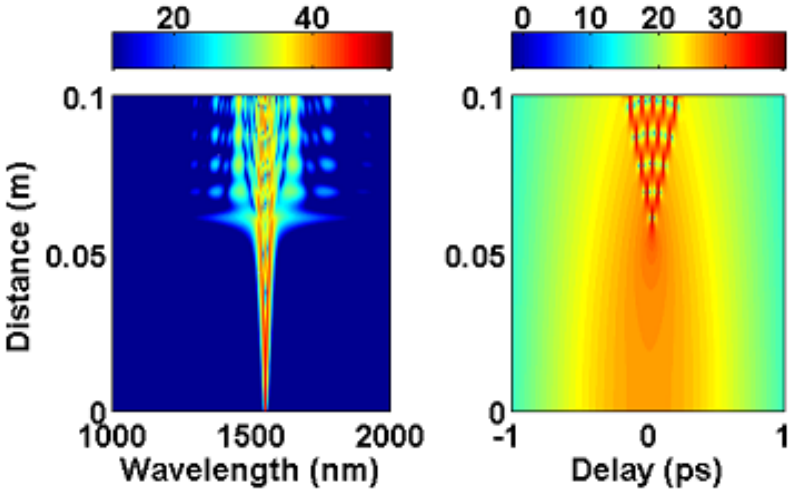

Figure 2. Supercontinuum Generation

Through this project we put forward into the vast possibilities of non linear effects in Optical fibres. Our major concern was to find the anomalous dispersion regime in single mode optical fiber and generate supercontinuum. For that purpose we have designed CS_2 filled core and alternate Chl and CS_2 is obtained. Here first layer of PCF is filled with chl, remaining layers are filled with alternate CS_2 and Chl

were background as silica . We found this geometry so that the effective refractive index of the cladding is reduced. Then we analyzed for different diameters(d) of cladding like d=0.8μ m and d=0.6μm , at various temperature like 20°C ,25°C ,30°C by changing the diameters of cladding and replacing with different materials . finally we got the anomalous dispersion by arranging alternate CS_2 and Chl with core as CS_2. Were the diameter of Chl are 2μm ,1.8μ m 1.9μm.We optimized the geometry to be in temperature 25°C and the diameter of cladding is 1.9μm.

Acknowledgement

We thank the COMSOL multiphysics software for the simulation and analysis presented in this work.

1. Reference

1. M Lee, Jeffrey M Roth, Todd G Ulmer, and Colm V Cryan. The fiber fuse phenomenon in polarization-maintaining fibers at 1.55 m. In Confere
2. VC Kuriakose and K Porsezian. Elements of optical solitons: An overview. Resonance, 15:643–666, 2010.
3. N Ayyanar, R Vasantha Jayakantha Raja, D Vigneswaran, B Lakshmi, M Sumathi, and K Porsezian. Highly efficient compact temperature sensor using liquid infiltrated asymmetric dual elliptical core photonic crystal fiber. Optical Materials, 64:574–582, 2017
4. Kumbirayi Nyachionjeka, Hillary Tarus, and Kibet Langat. Design of a photonic crystal fiber for optical communications application. Scientific African, 9:e00511, 2020.
5. Nagarajan Nallusamy, R Vasantha Jayakantha Raja, and G Joshva Raj. Highly sensitive nonlinear temperature sensor based on modulational instability technique in liquid infiltrated photonic crystal fiber. IEEE Sensors Journal, 17(12):3720–3727, 2017

Physics Research Reports (2024), **3–1**

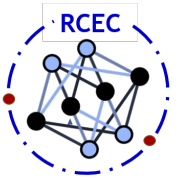

PHYSICAL SCIENCE RESEARCH RESULTS

The Influence of Size and Refractive Index Changes on Whispering Gallery Modes in Microresonators

Muhammed Gazzali K.[1] and Raman Namboodiri C. K.[2]

[1]Department of Physics, Sullamussalam Science College, Areekode, Kerala, India
[2]Department of Physics, National Institute of Technology, Calicut, Kerala, India

Abstract

The interaction of light with microparticles gives rise to whispering gallery modes (WGMs) which are highly sensitive to the morphology of the particle. The WGMs of a microsphere is theoretically simulated. These WGMs are found to be so sensitive to the size, refractive index, and the shape of the microresonators. The very high sensitivity of these modes on the particle size and the relative refractive index and hence can be used for many sensing applications that may find applications in various fields.

Keywords: WGMs, Mie Scattering, Electromagnetic Modes, Sensitivity.

Introduction

When electromagnetic waves interact with matter, various phenomena occur, including absorption, emission, scattering, reflection, refraction, and diffraction. Absorption involves light energy being taken in by an object, exciting electrons in atoms. Emission is the release of this excited energy as photons. Scattering spreads light in different directions, with matter absorbing light and re-emitting it in various directions. Reflection is when light bounces off a surface without being absorbed. Refraction changes the light's path due to varying velocities in different media. Diffraction is the bending and spreading of light around obstacles or through narrow openings [4].

PG Department of Physics, S.S. College - Areekode

The interaction of light with microparticles leads to different types of scattering that are Rayleigh, Mie, and Raman scattering. Rayleigh and Mie scattering are elastic, with incident and scattered energies remaining the same, while Raman scattering is inelastic, with different incident and scattered energies. Mie scattering is crucial in studying light interaction with microparticles, particularly in whispering gallery modes (WGMs) in spherical, cylindrical, and circular materials. WGMs in microspheres are significant due to minimal refraction loss, high-quality factors, and sensitivity, offering numerous research opportunities.

The whispering gallery modes (WGMs) were first observed in the St. Paul's Cathedral in London, designed by architect and scientist Sir Christopher Wren [3]. It got the name of whispering gallery because anyone whispering against its wall, at certain particular points near the wall is audible to listeners with an ear held close to the wall. Then John William Strutt (Lord Rayleigh) identified the focusing of sound over a curved surface of the wall [3]. Similar whispering gallery modes could occure in optical case also. Whispering gallery modes are also known as morphology dependent resonances. Most of the resonator are inefficient, expensive and low quality-factor whereas the microsphere is a whispering gallery mode micro-resonator. It has high quality-factor and easy to fabricate [3]. Its size is 10 -100 micrometer. The microsphere has many applications due to the high quality factor, high sensitivity, good optical resonator, easy to fabricate and small in size. Single photon source [7], biochemical sensor and mechanical sensing [5].

Theoretical study

The Mie scattering theory is derived from source free, free space and homogeneous Maxwell's equation. It obtain the scattering coefficient a_n and b_n.

$$a_n = \frac{\mu m^2 j_n(mx)[xj_n(x)] - \mu_1 j_1(x)[mxj_n(mx)]}{\mu m^2 j_n(mx)[xj_n^{(1)}(x)] - \mu_1 h_n^{(1)}(x)[mxj_n(mx)]} \tag{1}$$

$$b_n = \frac{\mu_1 j_n(mx)[xj_n(x)] - \mu j_n(x)[mxj_n(mx)]}{\mu_1 j_n(mx)[xj_n^{(1)}(x)] - \mu h_n^{(1)}(x)[mxj_n(mx)]} \tag{2}$$

The electromagnetic modes are weighted by the scattering coefficient. For each modes there will be appropriate scattering coefficient a_n and b_n. This scattering coefficient a_n and b_n are helps to find out the mode number using program.

The scattered field can be written in the super position of electromagnetic mode.

$$E_s = \sum_{n=1}^{\infty} E_n\left(ia_n N_{e1n}^{(3)} - b_n M_{o1n}^{(3)}\right) \tag{3}$$

The scattered electromagnetic fields is an infinite series of vector spherical harmonics M_n and N_n, the electromagnetic normal modes of the spherical particles. That is, scattered field is a super position of the normal modes. Each vector spherical harmonics has corresponding electromagnetic modes in spherical particles. The modes are weighted by appropriate coefficient a_n and b_n. For each n there are two types of modes. In one of the modes, there is no parallel component of magnetic field called transverse magnetic field. In another mode there is no parallel component of electric field called transverse electric field. For a particular n one of the denominator of a_n(equation 1.46) and b_n (equation 1.47) become very small, the corresponding normal mode will dominate the scattering field. the a_n mode dominant if the condition is satisfied,

$$\frac{[xh_n^{(1)}(x)]}{h_n^{(1)}(x)} = \frac{\mu_1[mxj_n(mx)]}{\mu_1 m^2 j_n(mx)}$$

The b_n mode dominant if the below condition is satisfy,

$$\frac{[xh_n^{(1)}(x)]}{h_n^{(1)}(x)} = \frac{\mu[mxj_n(mx)]}{\mu_1 j_n(mx)}$$

The frequency are exactly satisfy the condition, it called natural frequency of the sphere. If the incident wave frequency is matches with natural frequency, it excites various electromagnetic modes.
Electromagnetic modes are the WGMs of microsphere. This WGMs can simulate using programs by introducing the scattering coeffients.The theoretical simulation of WGMs of microsphere can do using program. In the basis of Mie theory. Computational Methods written by P.W. Barber and S. C. Hill. The refractive index and size parameter give to input of the program. The WGMs simulated using the Fortran language.

0.1 Effect of WGMs on the size and refractive index of microspheres

The WGMs of sphere of different sizes are simulated. From these simulations the mode shift of WGMs can be calculated. The number and mode order of WGMs are obtained using Fortran program S4.f written by P.W. Barber and S.C. Hill (copyright (c) 1990 by World Scientific Publishing Co Pte Ltd). The modes named as a represent TM modes and TE modes are named as b. The first number in the subscript represent the mode number and the second number is mode order. Figure 1 shows the WGMs calculated for two microsphere of radii 40.00 μm and 40.01μm. Figure 2 shows the WGMs calculated for two microsphere of radii 40.000 μm and 40.001μm.

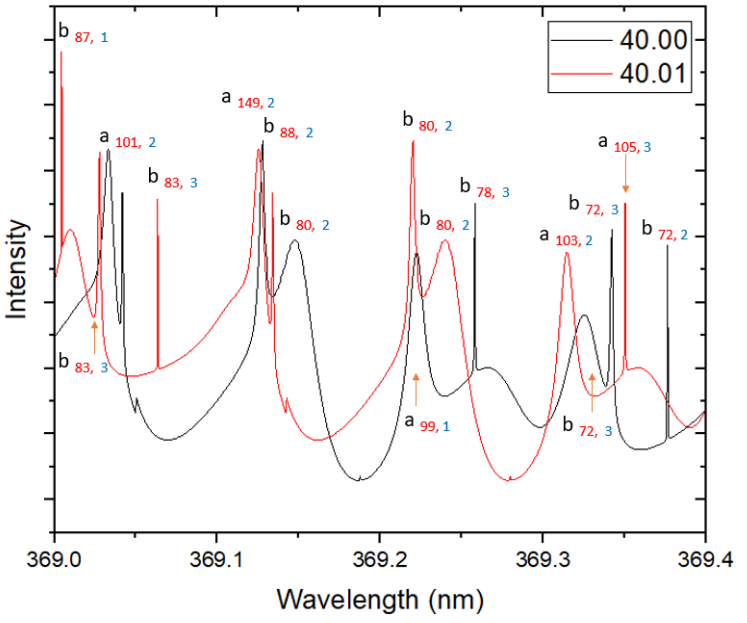

Figure 1. WGMs for microsphere of radii 40.00 μm and 40.01 μm.

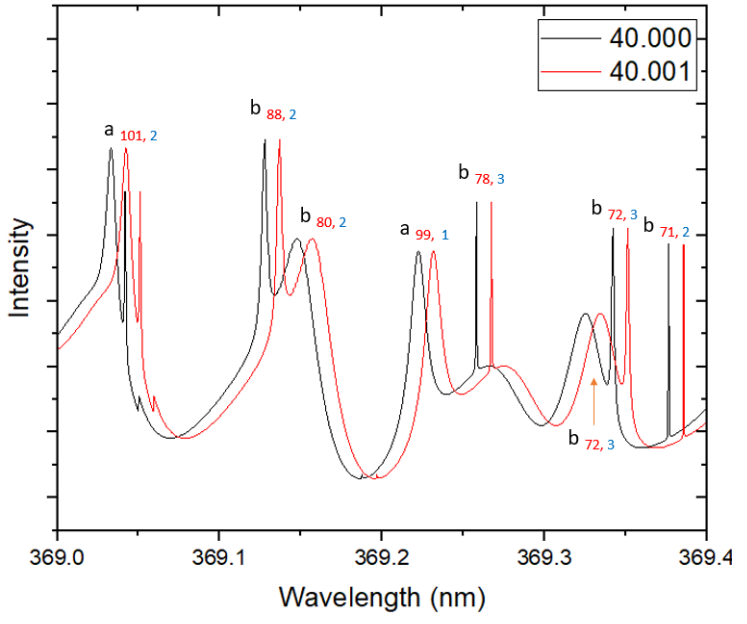

Figure 2. WGMs for microsphere of radii 40.000 μm and 40.001 μm.

The effect of relative refractive index on WGMS can be studied theoretically. Figure 3 shows the WGMs obtained for a microsphere with the refractive index values 1.500 and 1.505. It can be there are several modes in the size parameter

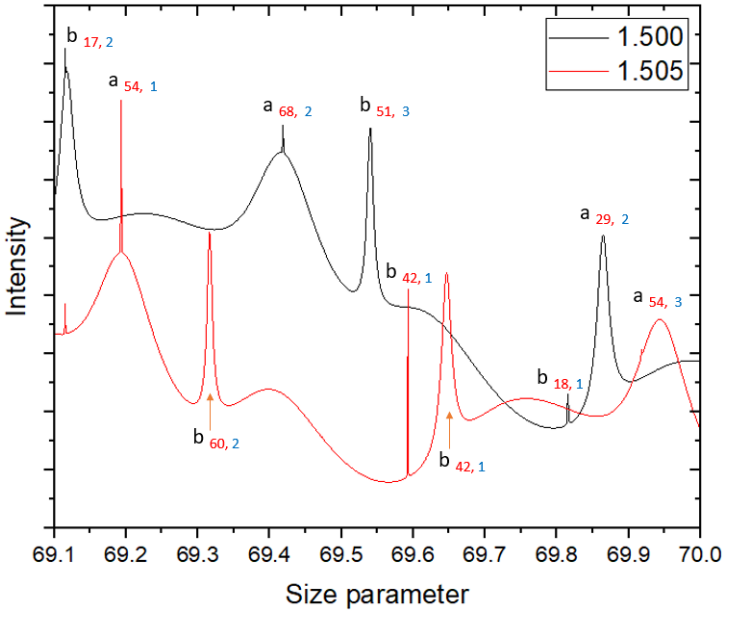

Figure 3. WGMs of a microsphere for different refractive indices 1.500 and 1.505

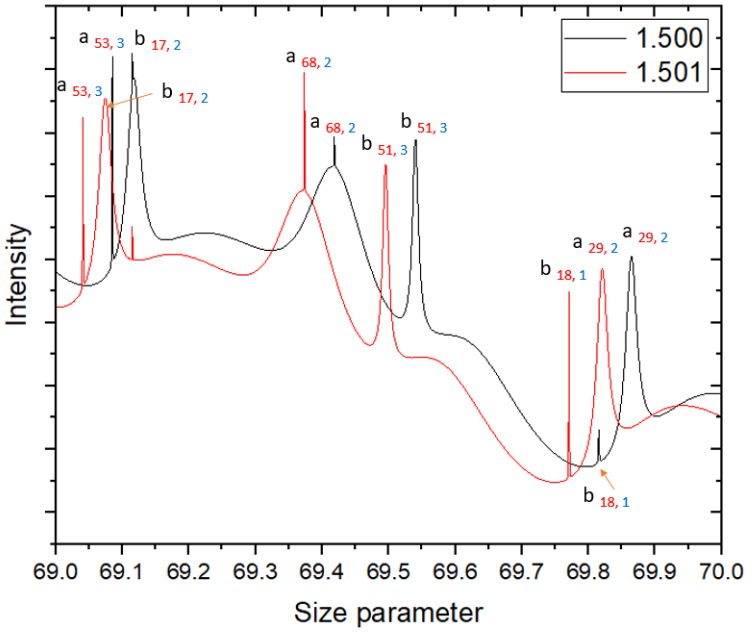

Figure 4. WGMs of a microsphere for different refractive indices 1.500 and 1.501

change 69.0 to 70.0 and these modes show a significant shift even for a refractive index change of 0.005. Figure 4 shows the WGMs obtained for a microsphere with the refractive index values 1.500 and 1.501. It can be there are several modes in the

size parameter change 69.0 to 70.0 and these modes show a significant shift even for a refractive index change of 0.001.

Conclusion

The sensitivity of WGMs of a microsphere is analysed. This sensitivity of the microsphere is used in many sensing application. A fortran programme by P.W. Barber and S.C. Hill (copyright (c) 1990 by World Scientific Publishing Co Pte Ltd.) is used for calculating the modes of a microsphere. The modes are calculated for different sizes. Also by varying the refractive index of WGMs of a microsphere are calculated. The study shows a significant shift of WGMs even for slight variation of size and refractive index.

Reference

[1] G Aruldhas. Molecular structure and spectroscopy. PHI Learning Pvt. Ltd., 2007.

[2] Craig F Bohren and Donald R Huffman. Absorption and scattering of light by small particles. John Wiley and Sons, 2008.

[3] Alessandro Chiasera, Yannick Dumeige, Patrice Feron, Maurizio Ferrari, Yoann Jestin, Gualtiero Nunzi Conti, Stefano Pelli, Silvia Soria, and Giancarlo C Righini. Spherical whispering-gallery-mode microresonators. Laser and Photonics Reviews, 4(3):457–482, 2010.

[4] AK Ghatak et al. Optics/ajoy ghatak., 2010.

[5] Andrey B Matsko and Vladimir S Ilchenko. Optical resonators with whispering-gallery modes-part i: basics. IEEE Journal of selected topics in quantum electronics, 12(1):3–14, 2006.

[6] Narges Miri and Morteza Mohammadzaheri. Optical sensing using microspheres with different size and material. IEEE Sensors Journal, 14(10):3593–3598, 2014.

[7] Zhiyuan Qian, Lingxiao Shan, Xinchen Zhang, Qi Liu, Yun Ma, Qihuang Gong, and Ying Gu. Spon- taneous emission in micro-or nanophotonic structures. PhotoniX, 2:1–35, 2021. 28

Physics Research Reports (2024), **3–1**

PHYSICAL SCIENCE RESEARCH RESULTS

Hydrothermal Synthesis and Characterization Studies of α-Fe_2O_3 for Energy Storage Supercapacitor Application

FAIJAS RAHMAN K*

Department of Physics, Sullamussalam Science College, Areekode, Kerala, India 673639
*Corresponding author. Email: faijaskeelath0@gmail.com

Abstract

Supercapacitors are gaining attention for their rapid charge-discharge times, cycle stability, and high power density, though their lower energy density compared to batteries limits their standalone use in many applications. Li-ion batteries offer over 180 Wh/kg, whereas supercapacitors typically provide less than 10 Wh/kg. However, supercapacitors excel in power density and cycle life. Efforts are underway to enhance their energy and power density through novel electrolytes, electrodes, and device design. Hematite (Fe_2O_3) has emerged as a significant electrode material for supercapacitors due to its low cost, abundance, and high theoretical capacitance.α-Fe_2O_3, in particular, is utilized with carbon as a negative electrode. Characterization techniques such as X-ray diffraction (XRD), Fourier Transform Infrared (FTIR) spectroscopy, UV-Visible spectroscopy, and Scanning Electron Microscopy (SEM) validate its properties. Electrochemical studies employing Cyclic Voltammetry (CV), Galvanostatic Charge-Discharge (GCD) tests, and Electrochemical Impedance Spectroscopy (EIS) further assess its performance.

Introduction

Energy is the cornerstone of modern civilization, powering homes, transportation, industries, and technology across every sector from agriculture to healthcare. As

PG Department of Physics, S.S. College - Areekode

the global economy expands and evolves, energy demand is projected to reach 28 terawatts (TW) by 2050. Currently, fossil fuels—derived from ancient organic matter like coal, oil, and natural gas—are the primary energy sources, offering high energy density crucial for efficient energy production and transportation. However, their environmental impacts include greenhouse gas emissions, air and water pollution, and habitat destruction, posing serious health risks such as respiratory and cardiovascular diseases, and even cancer due to carcinogenic components like benzene and polycyclic aromatic hydrocarbons (PAHs). Moreover, fossil fuels are finite resources with extraction and utilization affecting present and future generations. Urgent action is needed to transition towards cleaner, sustainable energy sources to mitigate these issues. Energy storage, a fundamental process dating back to prehistoric times with biomass like wood and charcoal, has evolved significantly. Coal, discovered around 900 years ago, revolutionized energy storage due to its high density compared to biomass, powering the first industrial revolution and subsequent electricity generation. Today, electricity, often termed the "lifeblood" of modern society, is increasingly sourced from renewables to reduce reliance on fossil fuels and cut carbon emissions. However, gaps remain in identifying suitable storage technologies for different applications, necessitating further research to optimize energy storage solutions for grid support and maximize green energy utilization while considering technical, financial, and environmental impacts

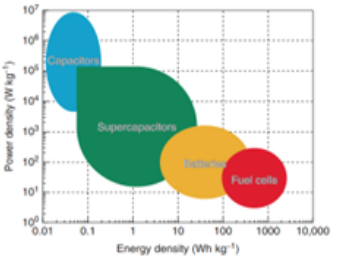

Figure 1. 1 Ragone plot for significant energy storage and conversion device

1. LITERATURE REVIEW

supercapacitors, also known as electrochemical capacitors, represent a promising alternative energy storage device that combines the benefits of batteries and capacitors while overcoming many of their limitations. They are characterized by high power densities, rapid charge-discharge capabilities, and eco-friendliness. Despite these advantages, their energy density has historically been lower compared to batteries, limiting their standalone applications. While commercially available supercapacitors typically offer energy densities below 10 Wh/kg, lithium-ion batteries can exceed 180 Wh/kg. Recent advancements in supercapacitor technology have focused on enhancing both energy and power densities. Researchers have

explored new electrode materials and electrolytes to achieve these goals. Key materials under investigation include conductive polymers, metal oxides like transition metal oxides (TMOs), and hydroxide particles. These materials exhibit high specific capacitances and are pivotal in improving the performance of supercapacitors. Transition metal oxides, such as iron oxide (Fe_2O_3), have emerged as promising electrode materials for supercapacitors due to their abundant availability, environmental compatibility, and high theoretical capacitance. Hematite (α-Fe_2O_3), a specific form of iron oxide, is particularly noteworthy for its stability, nontoxicity, and cost-effectiveness. It possesses a theoretical capacitance of approximately 3625 F/g, making it highly suitable for various applications. However, its practical application has been limited by its low electrical conductivity and substantial volume changes during charge-discharge cycles. To address these challenges, researchers have focused on nanostructuring -Fe2O3 to enhance its surface area and electrochemical properties. Nanoscale morphologies such as nanorods, nanotubes, nanoparticles, and quantum dots have been explored to shorten electron diffusion paths and improve conductivity. These advancements have significantly enhanced the electrochemical performance of α-Fe_2O_3-based electrodes, making them viable for high-performance supercapacitors. Synthesis methods for α-Fe_2O_3 include hydrothermal techniques, which involve reactions between iron precursors and appropriate chemicals under controlled conditions. For instance, synthesis in 1 M KOH has been shown to yield α-Fe_2O_3 electrodes with specific capacitances around 149.3 F/g and impressive energy and power densities of 4.20 Wh/kg and 224.90 W/kg, respectively. Furthermore, these electrodes exhibited excellent cycle stability, retaining 43.8 of their initial capacitance after 5000 cycles. Other studies have explored variations in synthesis parameters such as temperature to optimize the morphology and electrochemical stability of -Fe2O3 nanostructures. For instance, -Fe2O3 prepared via sol-gel routes at different temperatures demonstrated discharge capacitances up to 193 F/g and excellent capacitance retention of about 92% after 1000 cycles, highlighting their suitability for long-term supercapacitor applications. Despite these advancements, challenges remain in scaling up production and further improving the performance ofα-Fe_2O_3-based supercapacitors for commercial use. Addressing issues related to conductivity, volume changes, and cost-effectiveness will be crucial for realizing their full potential in energy storage applications. In conclusion, α-Fe_2O_3-based supercapacitors represent a promising avenue for advancing energy storage technologies due to their high theoretical capacitance, environmental benefits, and recent improvements in performance. Continued research and development efforts are essential to overcome existing challenges and unlock the full capabilities of these materials in addressing global energy needs sustainably

MATERIALS AND METHODS

1.1 Hydrothermal method

For a wide range of materials and morphologies, crystal formation from solutions has attracted a lot of interest because of its ease of use, affordability, and ambient pressure. Hydrothermal growth, a subset of solvothermal procedures, is generally carried out at moderate temperatures under 200°C and has the advantage of being safe and environmentally benign (growing from aqueous solution instead of organic solvent). Hydrothermal synthesis is the broad term for chemical processes that take place in an aqueous solution at high pressure and temperature. This method was created to resemble how minerals and rocks occur in the natural world. When autoclaves and other cutting-edge lining materials for high pressure reactors were developed, this method was expanded to prepare a range of materials, such as zeolites, coordination complexes

1.2 Materials

Here all of the compounds were analytical grade, no additional purification was necessary before using them. Every solution was made using double distilled (DD) water or deionized (DI) water. Materials required:

- Ferric Chloride ($FeCl_3.6H_2O$)

2. Synthesis of α-Fe_2O_3 from $FeCl_3.6H_2O$

To prepare α-Fe_2O_3, 1 M of $FeCl_3.6H_2O$which is around 10.81 g was dissolved in 40 ml of DI water. aftre that the solution is stirred around 6 hour using magnetic stirring at a rate 600 rotation per minute . This mixture was transferred into a 100 ml Teflon-coated autoclave that had 70 percent of its contents filled with DI water. This setup was exposed to a steady temperature at 180°C for six hours. The precipitate precipitates are now gathered then it is washed many times with DI water by centrifugation at a rate of 6000 rotation per minute in 4-5 times to get a clear solution. The formed precipitate cleaned with ethanol. then the resultant product was dried for twenty-four hours at 60 °C and calcined for two hours at 600 °C . The resultant product will be α-Fe_2O_3

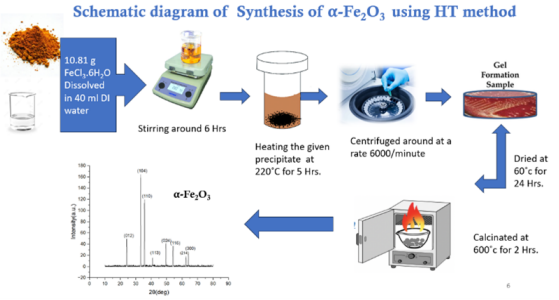

Figure 2. schematic diagram of synthesis ofα-Fe_2O_3

3. RESULTS AND DISCUSSION

3.1 Powder XRD analysis

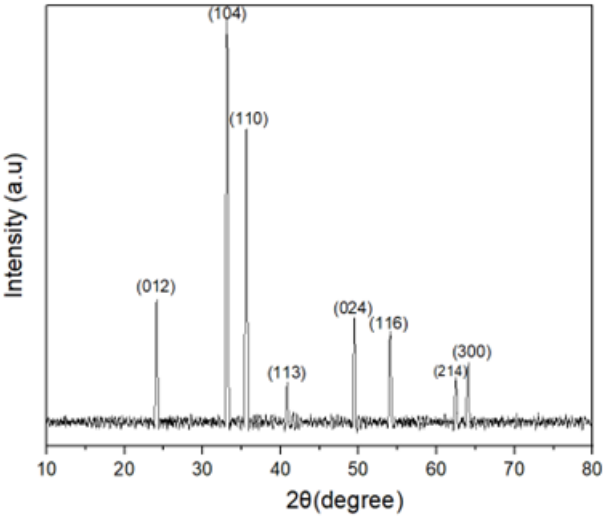

Figure 3. schematic diagram of synthesis ofα-Fe_2O_3

The X-ray diffraction pattern α-Fe_2O_3 is shown in fig 4.1. The noticeable peaks can viewed at 2 of 24.18 , 33.20, 35.68, 40.92, 49.53, 54.13, 62.50 and 64.06 which is indexed (012), (104), (110), (113), (024), (116), (214) and (300) respectively. All peaks are indexed in a Rhombohedral symmetry (space group: R-3c) in agreement with the JCPDS Card N 33-0664 indicating a good crystalline of α-Fe_2O_3 . α-Fe_2O_3 have predominant peaks (110), (214).The peak (104) presents stronger intensity for the hematite elaborated indicating that under conventional cleaning a higher amount of crystallize grows with the (100) planes parallel to the substrate surface. We also observe a clear appearance of the peak (012).

4. Electrochemical studies

Cyclic voltammogram of α-Fe_2O_3 performed at a voltage range of -1.1 to 0 V with scan rates ranging from 2 to 100 mV/s. Typical redox peaks were recorded in CV curves which indicates the reversible redox reaction and the prepared α-Fe_2O_3 is a typical pseudo capacitance material. Here we can see from the CV curves the current density and redox peaks increase regularly with scan rates so that the resistivity also increases, which results in a rapid decrease of the capacitive behavior. With the scanning rate increasing, the potential difference between the anodic and the cathodic peak in the CV curve does not change too much.

beginfigure[H]

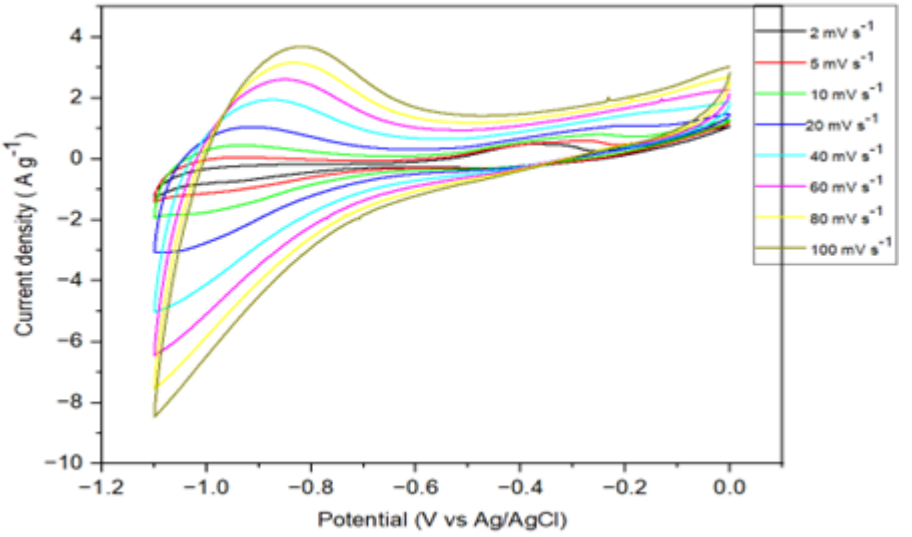

begintable[h]

Current density (A g^{-1})	Specific Capacitance (F g^{-1})
1	140.31
2	54.36
3	36.89
4	30.26
5	24.96

The anodic oxidation peak corresponds to the oxidation of Fe^{2+} to Fe^{3+} shifting in anodic peaks towards a positive (+ve) potential owing to electroactive sample polarization and the cathodic peak corresponds to the reduction Fe^{3+} to Fe^{2+} . This indicates a good electrochemical reversibility of α-Fe_2O_3 electrode material which results from the kinetics of the interfacial faradaic redox reactions as well as the

rapid electron transport.

Conclusion

In recent years, Supercapacitors or ultracapacitors is a noteworthy electrochemical energy storage system catching more attention due to their elevated good stability, power density, low price, long cycling stability, non-hazardous to environment and other excellent properties .The gaps among batteries, conservative solid state, electrolytic capacitors are appropriately filled by supercapacitors and they can play a vital role in supplementing or replacing batteries. They are initially used in hybrid electric vehicles, electric vehicles, and fuel cell vehicles. Today's supercapacitors can provide charge-discharge currents in the tenth to hundredth of an ampere range and have capacities ranging from several thousand to several thousand farads. In this work we successfully synthesized α-Fe_2O_3 nanospheres on carbon cloth and evaluated electrochemical performance of -Fe2O3 electrode in aqueous 1 M KOH solution. It was characterized using different characterization techniques. XRD analysis showed that as-synthesized α-Fe_2O_3 has rhombohedral symmetry (spacegroup: R-3c), in agreement with the JCPDS Card N 33-0664. FTIR and UV-Visible techniques confirmed the XRD findings and evidenced the presence of Fe and O2 molecule . Morphology was clarified by FE-SEM, The electrochemical performance was evaluated using CV, GCD, and EIS. From CV, it was found that current density increases with scan rates, resulting in the decline of specific capacitances. From GCD, α-Fe_2O_3 electrode shows an excellent electrochemical performance with a high specific capacitance of140.31 F g-1 at a current density of 1 A g-1 and it was found that specific capacitance decreases gradually as current density increases. EIS analysis proposes high capacitance, high phase homogeneity and improved charge-transfer characteristics also α-Fe_2O_3 electrode can be beneficial for good conductivity. In summary, a hydrothermal route was implemented to construct -Fe2O3. Additionally, the composite was employed as a working electrode material to establish its probable application as a favorable electrode substance for highly efficient hybrid supercapacitors. It proves that α-Fe_2O_3 electrode material can be an economical anode material for next generation super-capacitor applications

Acknowledgement

This work was supported by National institute of technology (NIT), Calicut, Kerala.

Physics Research Reports (2024), **3–1**

PHYSICAL SCIENCE RESEARCH RESULTS

OPTIMIZATION OF SAMPLE PREPRATION FOR PIEZORESISTIVTY STUDY IN COCONUT COIR DERIVED CARBON

BUSHAIR ALI.K,[1] Mr. Mohammed Mudassir,[2] and Dr. C. N. Shyam Kumar[*,3]

[1]Department of Physics, Sullamussalam Science College, Areekode, Kerala, India 673639
[2]Materials Science and Engineering National Institute of Technology Calicut, Kerala
[3]Assistant Professor,Materials Science and Engineering National Institute of Technology Calicut
[*]Corresponding author. Email: bmrmorayur@sscollege.ac.in

Abstract

Pyrolyzed carbon materials have garnered significant attention in recent years due to their unique combination of mechanical, electrical, and thermal properties. This study focuses on the optimization of sample preparation for piezoresistivity studies in coconut coir-derived carbon and explores the piezoresistive behavior at different pyrolysis temperatures: 600°C (CCP-600), 800°C (CCP-800), and 1000°C (CCP-1000).

The study investigates the electrical and piezoresistive properties of CCP-600, CCP-800, and CCP-1000 materials. CCP-600 exhibits higher resistivity ($\rho = 1.342\,\Omega \cdot m$, $\sigma = 0.745$ S/m) than CCP-800 (1.06×10^3 S/m) and CCP-1000 (1.5×10^3 S/m). Despite its lower conductivity, CCP-600 demonstrates impressive piezoresistive characteristics, with a gauge factor (GF) of 4.098 ± 0.098 in fiber form and 25.42 ± 1.174 in powdered form. Optimizing sample preparation with elastic, flexible substrates and adhesives enhances CCP-600's piezoresistive performance. The study highlights CCP-600's potential as a low-cost, high-performance material for sensor applications.

Keywords: Pyrolyzed carbon, Coconut coir derived carbon, conductivity, Piezoresistive behavior.

PG Department of Physics, S.S. College - Areekode

Introduction

Piezoresistive behavior refers to the change in electrical resistivity with mechanical strain **source65**. Positive piezoresistivity occurs when resistivity increases with strain, while negative piezoresistivity occurs when resistivity decreases. This behavior is quantified by the gauge factor (GF), defined as the fractional change in resistance per unit strainFiorillo, Critello, and Pullano 2018:

$$\mathrm{GF} = \frac{\Delta R/R_0}{\epsilon} = \frac{\Delta R/R_0}{\Delta L/L_0} \tag{1}$$

where ΔR is the change in resistance, R_0 is the initial resistance, ϵ is the strain, ΔL is the change in length, and L_0 is the initial length. Strain is the change in dimension relative to the original dimension. Metal strain gauges, such as those made of aluminum, gold, or copper, typically exhibit a GF of around 2 Kordas and Pitkänen 2019. In contrast, semiconductors demonstrate a GF over one order of magnitude higher than metals (e.g., p-type Si has a GF of $\sim$100) Kordas and Pitkänen 2019.

Recent research has focused on various carbon allotropes for piezoresistive applications, including graphite Sun et al. 2017; Chen, Chen, and Lu 2007; Ren et al. 2012, carbon nanotubes (CNTs) Dai et al. 2016, amorphous carbon (a-C) Ma et al. 2020, graphene Herren, Saha, and Liu 2020, and nanofoams Kordas and Pitkänen 2019. Glass-like carbon (GC), a disordered sp^2 carbon classified as non-graphitized carbon, also exhibits piezoresistive behavior Jang et al. 2021. These materials can self-sense strain without attached sensors, offering low cost, high durability, large sensing volume, and no mechanical property loss compared to traditional sensors.

Carbon fiber sensors find applications in pressure sensors Tran, Zhang, and Zhu 2017, accelerometers Hari et al. 2018, force sensors Ma et al. 2019, tactile sensors Stassi et al. 2014, and flow sensors Ejeian et al. 2019.

Pyrolysis, the process of heating in the absence of oxygen, produces pyrolyzed carbon materials with intrinsic piezoresistive behavior Kumar 2021. This makes them suitable for self-sensing strain sensors, with piezoresistive behavior influenced by factors like crystallite size, sp^2 content, and morphology. Organic materials such as coconut shell, fiber, sugarcane waste, and coffee husk are potential carbon sources for pyrolysis. Coconut-derived carbons have been explored in battery electrodes, gas sensing, and catalysis, but their piezoresistive behavior remains unreported.. The present study aims to fabricate piezoresistive strain sensors from pyrolyzed coconut fibers, leading to the development of piezoresistive sensors derived from coconut fiber-derived carbon.

Experimental techniques

(a)Preparation of Sample:

The coconut fiber was pyrolyzed at three different temperatures: 600°C, 800°C, and 1000°C, resulting in products named CCP-600, CCP-800, and CCP-1000 respectively.

Sample with single fiber:

The sample-1 used a PET substrate, silica gel additive, and CCP fiber. A 1.5 cm CCP fiber piece from pyrolyzed fiber was placed on PET, its ends connected to non-insulated copper wire with silver paste for conductivity. However, PET's thickness made bending difficult, silica gel hardened, risking fiber breakage. Thick copper wire caused movement errors in piezoresistivity measurement, limiting strain tolerance of CCP fiber.

simlarly sample-2 was prepared using a PVC substrate, Fevicol adhesive, and CCP fiber. Fevicol glue ensured strong adhesion, and 1.5 cm CCP fibers were used. Insulated 10 mm copper wire with silver paste ensured good conductivity. After curing the paste, additional Fevicol protected the fiber. With these preparations, the piezoresistivity of a single CCP fiber was measured for the first time. Despite initial breakage issues, powdering the fiber aimed to enhance durability and measurement reliability.

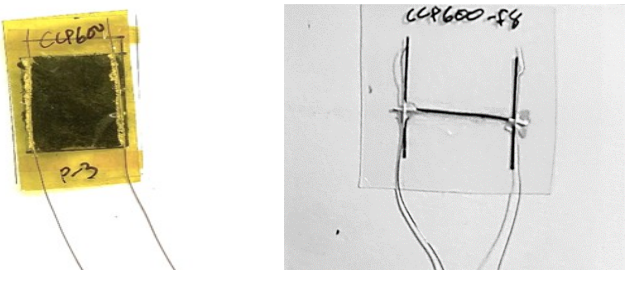

(a) (b)

Figure 1. Prepared sample (a)CCP Powder and (b) CCP Fiber

Sample with powder:

Sample 3: CCP fibers were powdered and applied to a 0.32 mm PET substrate in a 2.5 cm by 1.5 cm area using Fevicol for adhesion, with insulation to contain the powder. Despite attempts to hot-press for uniformity, PET deformation occurred. Non-insulated copper wire and PET's bending strain posed challenges, affecting piezoresistive accuracy.

Sample 4: Utilizing a PVC substrate, a 2.5 cm by 1.5 cm area marked and covered with masking tape. Fevicol was applied within this area, and CCP powder was evenly spread using a spatula. After curing and removal of excess powder and tape, insulated copper wire ensured conductivity with silver paste to minimize resistance.

Brief heating facilitated effective curing, with a polyimide tape layer providing durability and precise piezoresistivity measurements. This setup supports high strain tolerance, ease of handling, durability, and reusability, ideal for piezoresistive studies.

(b)Conductivity measurement

The sample was connected to a source meter. Diameter, d ($2r$) of the fiber was observed in an optical microscope, length L found using a vernier caliper, and resistance R was measured using the source meter.

The area A is calculated as $A = \frac{\pi r^2}{2} = \frac{\pi d^2}{4}$

Using R, A, and L, we can calculate the resistivity of the material as $\rho = \frac{RA}{L}$.

The conductivity $\sigma = \frac{1}{\rho} = \frac{L}{RA}$.

(c)Strain and Piezorestivity Calculation:

Length of the fiber, L

Thickness of the substrate, D

Step size, x (distance moved by the stepper motor)

Thickness of CCP, t (assumed to be much smaller than D, i.e., $t \ll D$)

Consider arc AB centered at O: $\theta = \frac{L}{2R}$

Consider triangle MBO: $\sin\theta = \frac{L-x}{2}$

Binomial expansion of $\sin\theta$: $\sin\theta = \theta - \frac{\theta^3}{3!} + \frac{\theta^5}{5!} + \ldots$

Combining equations 5, 6, and 7 gives:

$$2R\left[\left(\frac{L}{2R}\right)^3 \frac{1}{3!} - \left(\frac{L}{2R}\right)^5 \frac{1}{5!} - \left(\frac{L}{2R}\right)^7 \frac{1}{7!}\right] = x$$

The equation 5.4 was solved using a MATLAB code, which converges at a solution for R at each value of x.

Then, strain was calculated using equation: $\epsilon = \frac{D}{2R}$

Piezoresistivity measurements:

Piezoresistivity was measured using a custom-made in situ microtensile tester. The sample was loaded between the grips, and a compressive force was applied to bend the substrate, with the corresponding readings of resistance noted.

Using resistance values and strain values, the gauge factor was calculated:

$$\text{Gauge factor GF} = \frac{\Delta R/R_0}{\epsilon}$$

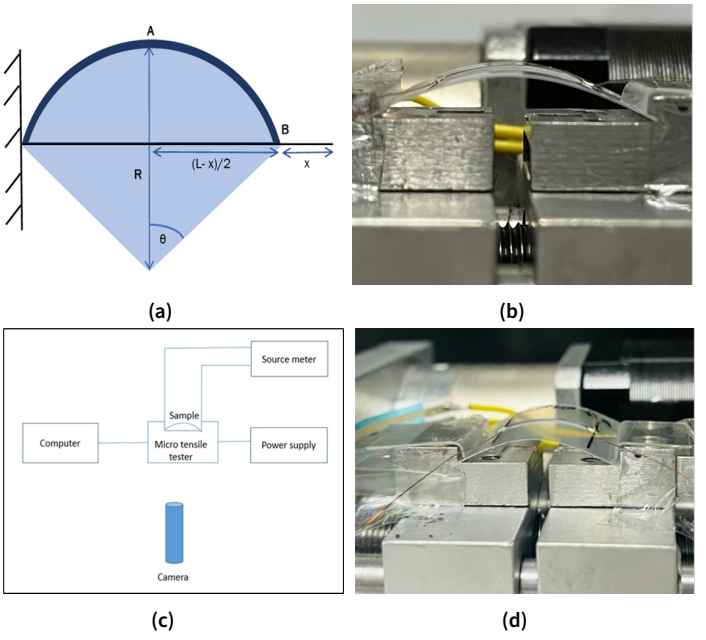

Figure 2. (a) Curvature of the substrate when bended (b) Close up view of the sample on bending(c)Schematic representation of setup to testing piezoresistivity (d)close view of sample in Micro tensile Tester

Result and Discussion

(i)Raman Spectroscopy:

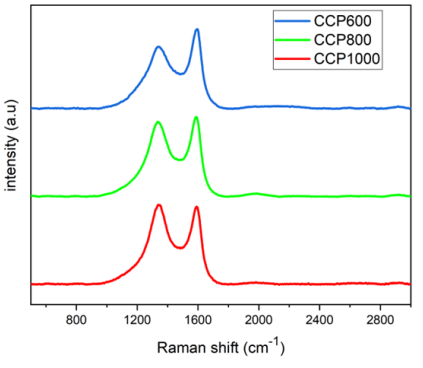

Figure 3. Raman spectrum of CCP600, CCP800 and CCP100

For CCP-600, CCP-800, and CCP-1000 fibers, the D band occurs from 1587 to 1595 cm^{-1} and the G band occurs from 1342 to 1337.7 cm^{-1}. Two main peaks at 1350 cm^{-1} and 1600 cm^{-1} represent the disorder band (D-band) and graphite band

(G-band) of a typical pyrolyzed carbon, respectively Dai et al. 2016.
The I_d/I_g ratio represents the sp^2 cluster (graphitic cluster) Ferrari and Robertson 2000. With I_d/I_g ratios of 0.77, 0.93, and 1.025 for CCP600, CCP800, and CCP1000 respectively, a transient increase confirms the increasing sp^2 cluster in the material with an increase in temperature.
The results of Raman spectroscopy state that the D band and G band peaks are similar to pyrolyzed carbon. Also, the I_d/I_g ratios state that the sp^2 cluster symmetrically increases with increasing temperature.

(ii)Conductivity :
Conductivity experiments show differences between CCP-600, CCP-800, and CCP-1000, with CCP-600 displaying much lower conductivity at approximately 0.745 S/m compared to CCP-800's higher conductivity at around 1.06×10^3 S/m and CCP-1000 at 1.5×10^3 S/m. This trend indicates that conductivity increases with increasing pyrolysis temperature. The increase in sp^2 clusters, which are conductive, with increase in pyrolysis temperature is the primary reason behind this improvement. As the pyrolysis temperature rises, sp^2 clusters increased relative to sp^3 clusters, which are non-conductive. Therefore, the increased presence of sp^2 clusters enhances the overall conductivity of the material.
Our conductivity data is compared to established materials: carbon nanotubes (CNTs) range from 1×10^5 S/m to 1×10^7 S/m, metallic conductors and graphite reach up to 1×10^7 S/m and 1×10^8 S/m, respectively Ejeian et al. 2019. CCP-1000 shows notable conductivity at 1.5×10^3 S/m, positioning coconut-derived carbon competitively. CCP-600 exhibits lower conductivity, suggesting higher resistivity. Enhancing coconut-derived carbon's conductivity could expand its applications in electrically demanding fields.

(III)Piezoresistivity:
Sample-1 encountered challenges with a PET substrate that required excessive bending strain, leading to increased resistance. Additionally, silica gel hardening and thick copper wire movements caused significant resistance fluctuations, with silver paste connections prone to detachment due to wire rigidity. Consequently, Sample-1 proved unsuitable for piezoresistive studies, highlighting the need for a thin, flexible substrate, thinner copper wire, and a flexible additive for CCP-600 fiber investigations.

Sample-3, which utilized a thick PET substrate, Fevicol, CCP-600 powder, and polyimide tape, also faced issues with bending strain increasing resistance over time. Minor copper wire movements further exacerbated resistance fluctuations, and silver paste connections were prone to detachment. Thus, Sample-3 was also deemed

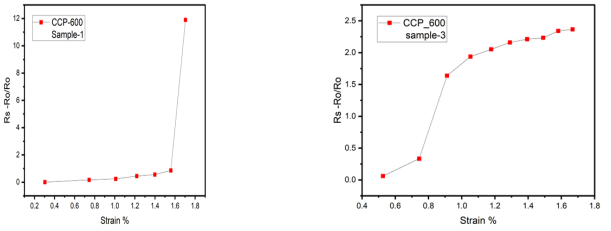

(a) (b)

Figure 4. Strain % versus $\Delta R/R_0$ graph of (a)CCP-600 fiber with sample 1 (b) CCP-600 powder with sample 3

inappropriate for piezoresistive studies, emphasizing the importance of adopting a thin, flexible substrate and thinner copper wire to enhance the efficacy of CCP-600 fiber research.

FIBER:

Coconut-derived carbon single fibers exhibit piezoresistive behavior. Among them, CCP-600 demonstrates significantly better performance than CCP-800 and CCP-1000. The CCP-600 fiber has a maximum gauge factor (GF) of 4.098, whereas CCP-800 and CCP-1000 have gauge factors of 0.74 and 0.67, respectively.

Overall, coconut-derived carbon fiber proves to be a good piezoresistive material, with CCP-600 particularly standing out due to its high sensitivity to mechanical deformation. However, it is important to note that CCP-600 can only withstand lower strain levels due to the risk of breakage in the single fiber. Despite this limitation, CCP-600 is highly suitable for applications requiring precise strain sensing.

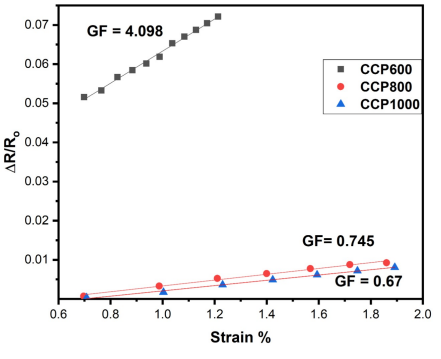

Figure 5. Strain % versus $\Delta R/R_0$ graph of CCP-600,CCP-800 and CCP-1000 fiber

Powder Sample:

Coconut-derived carbon powder exhibits significantly better piezoresistive behavior compared to CCP fiber. CCP powder, especially CCP-600, demonstrates a much higher piezoresistive gauge factor than CCP-800 and CCP-1000 powders. This high gauge factor indicates CCP powder's exceptional sensitivity to mechanical strain, making it well-suited for precise sensor applications. Unlike CCP fiber, CCP powder can withstand higher strain levels without breaking, and it is easier to handle and reuse. These properties highlight CCP powder, particularly CCP-600, as a promising material for developing cost-effective and efficient sensors across various industries.

Coconut-derived carbon, particularly CCP-600 powder, exhibits exceptional piezoresistive properties compared to other materials. Metals typically have a gauge factor around 2, while SU-8 glass-like carbon and single-layer graphene range from 1.6 to 3.5. In contrast, CCP-600 powder showcases a remarkable gauge factor of 25.42, outperforming even costly materials like amorphous carbon and photoresist. This high sensitivity makes CCP-600 powder highly suitable for affordable and efficient sensors across various applications. Continued research into CCP-600's capabilities holds promise for advancing sensor technologies in the future.

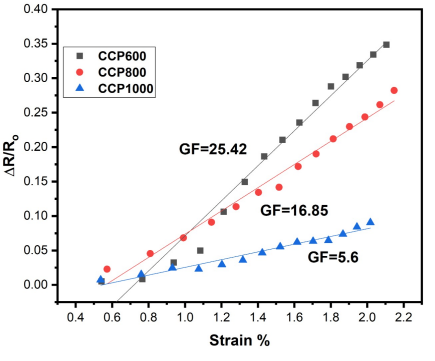

Figure 6. Caption

Conclusion

The study of CCP materials at different pyrolysis temperatures reveals significant variations in their conductivity and piezoresistive properties. CCP-600, with its much lower conductivity of approximately 1 S/m compared to CCP-800's 1×10^3 S/m and CCP-1000's 1.5×10^3 S/m, demonstrates impressive piezoresistive characteristics. Despite its higher resistivity, CCP-600 exhibits a gauge factor (GF) of 4.09, making it suitable for precise sensing applications such as pressure sensors or strain gauges. Conversely, CCP-800 and CCP-1000 fibers exhibit weaker piezoresistive

behavior, with GFs of 0.74 and 0.69, respectively.
When powdered, these materials show improved piezoresistive behavior, with CCP-600 powder demonstrating an excellent GF of 25.42, further enhancing its suitability for precise sensing applications. In comparison, CCP-800 and CCP-1000 powders exhibit lower piezoresistive behavior with GFs of 16.85 and 4.08, respectively.
The method of fabrication of samples plays an important role in piezoresistivity measurement. By choosing an elastic and flexible substrate and adhesive, it is possible to develop better piezoresistive sensors using CCP-600. CCP-600's cost-effectiveness and easy fabrication make it particularly promising for low-budget sensor applications, widening accessibility and offering significant potential for diverse and precise sensing needs. Understanding these material-specific properties facilitates informed material selection, ensuring optimal sensor design. Further exploration into CCP-600's piezoresistive behavior could unlock additional sensor capabilities and broaden its applications across various fields.

Acknowledgement

I am grateful to God for strength and guidance. Special thanks to Dr. C. N. Shyam Kumar, Assistant Professor, MSED, NIT Calicut, Mr. Mohammed Mudassir, PhD scholar, NITC and faculties at Sullamussalam Science College, along with my family and friends.

1. confrence

- Bushair Ali K, Mohammed Mudassir, and Dr. C. N. Shyam Kumar. (2024). Piezoresistivity in coconut coir derived carbon. In *Proceedings of the International Conference on Science and Commerce, SICSAC 2024*. Sullamussalam Science College, Areekode.
- Mohammed Mudassir, Bushair Ali K, and Dr. C. N. Shyam Kumar. (2024). Piezoresistivity in coconut coir-derived carbon. In *Proceedings of the Research Conclave on Global Transformation 2024, ReCon-24*. National Institute of Technology, Calicut.

example

References

Chen, Ling, GH Chen, and Liang Lu. 2007. Piezoresistive behavior study on finger-sensing silicone rubber/graphite nanosheet nanocomposites. *Advanced Functional Materials* 17 (6): 898–904.

Dai, Xiao, Jiang Wu, Zhicheng Qian, Haiyan Wang, Jie Jian, Yingjie Cao, Mark H Rummeli, Qinghua Yi, Huiyun Liu, and Guifu Zou. 2016. Ultra-smooth glassy graphene thin films for flexible transparent circuits. *Science advances* 2 (11): e1601574.

Ejeian, Fatemeh, Shohreh Azadi, Amir Razmjou, Yasin Orooji, Ajay Kottapalli, Majid Ebrahimi Warkiani, and Mohsen Asadnia. 2019. Design and applications of mems flow sensors: a review. *Sensors and Actuators A: Physical* 295:483–502.

Ferrari, Andrea C, and John Robertson. 2000. Interpretation of raman spectra of disordered and amorphous carbon. *Physical review B* 61 (20): 14095.

Fiorillo, AS, CD Critello, and SA Pullano. 2018. Theory, technology and applications of piezoresistive sensors: a review. *Sensors and Actuators A: Physical* 281:156–175.

Hari, K, Satish Kumar Verma, IR Praveen Krishna, and V Seena. 2018. Out-of-plane dual flexure mems piezoresistive accelerometer with low cross axis sensitivity. *Microsystem Technologies* 24:2437–2444.

Herren, Blake, Mrinal C Saha, and Yingtao Liu. 2020. Carbon nanotube-based piezoresistive sensors fabricated by microwave irradiation. *Advanced Engineering Materials* 22 (2): 1901068.

Jang, Jongmoon, Giulia Panusa, Giovanni Boero, and Juergen Brugger. 2021. A glass-like carbon mems strain sensor. In *2021 21st international conference on solid-state sensors, actuators and microsystems (transducers),* 871–874. IEEE.

Kordas, Krisztian, and Olli Pitkänen. 2019. Piezoresistive carbon foams in sensing applications. *Frontiers in Materials* 6:93.

Kumar, Sandeep. 2021. Nanocarbon devices and sensors.

Ma, Xin, Peng Guo, Xiaoshan Tong, Yulong Zhao, Qi Zhang, Peiling Ke, and Aiying Wang. 2019. Piezoresistive behavior of amorphous carbon films for high performance mems force sensors. *Applied physics letters* 114 (25).

Ma, Xin, Xiaoshan Tong, Peng Guo, Yulong Zhao, Qi Zhang, Hanchao Li, Rende Chen, and Aiying Wang. 2020. Mems piezo-resistive force sensor based on dc sputtering deposited amorphous carbon films. *Sensors and actuators A: Physical* 303:111700.

Ren, Tian-Ling, He Tian, Dan Xie, and Yi Yang. 2012. Flexible graphite-on-paper piezoresistive sensors. *Sensors* 12 (5): 6685–6694.

Stassi, Stefano, Valentina Cauda, Giancarlo Canavese, and Candido Fabrizio Pirri. 2014. Flexible tactile sensing based on piezoresistive composites: a review. *Sensors* 14 (3): 5296–5332.

Sun, Shengwei, Baoguo Han, Shan Jiang, Xun Yu, Yanlei Wang, Hongyan Li, and Jinping Ou. 2017. Nano graphite platelets-enabled piezoresistive cementitious composites for structural health monitoring. *Construction and Building Materials* 136:314–328.

Tran, Anh Vang, Xianmin Zhang, and Benliang Zhu. 2017. The development of a new piezoresistive pressure sensor for low pressures. *IEEE Transactions on industrial electronics* 65 (8): 6487–6496.

Physics Research Reports (2024), **3–1**

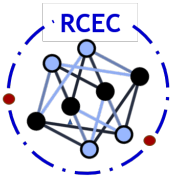

PHYSICAL SCIENCE RESEARCH RESULTS

ANALYSIS OF GALAXY FORMATION USING COMPUTATIONAL TOOLS

Fathima Saja P.V[1] and Sabeel P.K[*,2]

[1]Department of Physics, Sullamussalam Science College, Areekode, Kerala, India 673639
[2]Department of Physics, Sullamussalam Science College, Areekode, Kerala, India 673639
[*]Corresponding author. Email: sabeel@sscollege.ac.in

Abstract

The formation and evolution of galaxies are pivotal in understanding the large-scale structure of the universe. This project aims to analyze galaxy formation by employing computational tools and techniques. Computational tools are now widely used in the field of astronomy .It is a powerful tool to study one of the biggest challenges for theoretical cosmology: How did the galaxies we see in the universe today form out of the small fluctuations in matter density that were present in the primordial universe. We review the current theory of how galaxies form within the cosmological framework. Beginning with the pre-galactic evolution of baryonic material we describe the analytical and numerical understanding of how baryons condense into galaxies, what determines the structure of those galaxies and how internal and external processes (including star formation, merging, active galactic nuclei, etc.) determine their gross properties and evolution.By integrating observational data from telescopes with theoretical models, we seek to elucidate the interplay between dark matter, baryonic matter, and cosmic evolution. . We study in detail the relatinship between gravitational redshift and formation redshift .The outcomes will contribute to refining current cosmological models and enhancing predictive accuracy, offering a deeper comprehension of the universe's history and structure.

Keywords: Galaxy Formation, Gravitational Redshift, Formation Redshift, Spectral Class

PG Department of Physics, S.S. College - Areekode

Introduction

A galaxy is a massive, gravitationally bound system consisting of stars, stellar remnants, interstellar gas, dust, dark matter, and possibly dark energy. Galaxies vary greatly in size and shape, from dwarf galaxies with just a few billion stars to giant galaxies with one hundred trillion stars or more, all orbiting a common center of mass. The most common types of galaxies include spiral galaxies, like the Milky Way, elliptical galaxies, and irregular galaxies. Galaxies are the fundamental building blocks of the universe, forming large structures like galaxy clusters and superclusters. How did the galaxies we see in the universe today form out of the small fluctuations in matter density that were present in the primordial universe.The study of the formation of galaxies did not begin until after their extra-Galactic status was confirmed by Hubble (1929). In fact, much of the early work on galaxy evolution and formation was driven by the necessity of understanding galaxies in order to answer questions of cosmology (such as whether or not the Universe began with a Big Bang). While an understanding of galaxies remains necessary for such reasons even today, the field has since become an important one in its own right.[4]

Galaxy Formation Theory

The formation of structure in the Universe is seeded by minute perturbations in matter density expanded to cosmological scales by inflation.The dark matter component, having no pressure, must undergo gravitational collapse and, as such,these perturbations will grow. The linear theory of cosmological perturbations is well understood and provides an accurate description of the early evolution of these perturbations. Once the perturbations become nonlinear, their evolution is significantly more complicated.The final result of the nonlinear evolution of a dark matter density perturbation is the formation of a dark matter halo: an approximately stable, near-equilibrium state supported against its own self-gravity by the random motions of its constituent particles. In a hierarchical universe the first halos to form will do so from fluctuations on the smallest scales. Later generations of halos can be thought of as forming from the merging of these earlier generations of halos. For the purposes of galaxy formation, two fundamental properties of the dark matter halos are of primary concern: (i) the distribution of their masses at any given redshift and (ii) the distribution of their formation histories (i.e. the statistical properties of the halos from which they formed).The insight of Press and Schechter (1974) was that halos could be associated with peaks in the Gaussian random density field of dark matter in the early universe. Using the relatively simple statistics of Gaussian random fields they were able to derive the following form for the distribution of dark matter halo masses such that the number of halos per unit volume in the mass range M to M + M is M(dn/dM) where:

$$\frac{dn}{dM}(M,t) = (\frac{2}{\pi})^{\frac{1}{2}} \frac{\rho_0}{M^2} \frac{\delta_c(t)}{\sigma(M)} \frac{dln\sigma}{dlnM} exp[-\frac{\delta_c^2(t)}{2\sigma^2(M)}] (1)$$

where ρ_0 is the mean density of the Universe, (M) is the fractional root variance in the density field smoothed using a top-hat filter that contains, on average, a mass M, and c(t) is the critical overdensity for spherical top-hat collapse at time t (Eke et al., 1996).While the Press and Schechter (1974) expression is remarkably accurate given its simplicity, it does not provide a sufficiently accurate description of modern N-body measures of the halo mass function.[3]

Dark matter halos are characterized by their large overdensity with respect to the background density. Spherical top-hat collapse models (e.g. Eke et al., 1996) show that the overdensity, , of a just collapsed halo is approximately 200, with some dependence on cosmological parameters. This overdensity corresponds, approximately, to the virialized region of a halo, and allows us to define a virial radius as

$$r_v = (\frac{3M}{4\pi\rho_0\Delta})^{\frac{1}{3}} \quad (2)$$

Baryons are initially distributed near uniformly—they are expected to trace the dark matter distribution on scales above the Jeans length (Arons and Silk, 1968; Gnedin and Hui, 1998). To form galaxies they must first be concentrated by the forces of gravity which are dominated by the distribution of dark matter. In particular, we expect that baryons will concentrate towards the deep potential wells of dark matter halos. These should therefore be the sites of galaxy formation.[2]

Baryonic material will be dragged along by the gravitationally dominant dark matter such that dark matter halos are expected to accrete baryonic material. How much baryonic material they accrete depends upon the depth of their potential well and the pressure of the baryons. An accretion shock is a generic expectation whenever the gas accretes supersonically as it will do if the halo virial temperature exceeds the temperature of the accreting gas (Binney, 1977a).

What happens next depends on the relative value of the cooling and collapse timescales. Masses in the range 10^{10}–10^{12} M cool so efficiently that they always collapse at the free-fall rate, and probably quickly fragment into stars.Larger masses may,however, experience a quasistatic contraction phase. . . ". Thus, Rees and Ostriker (1977) clearly understood the difference between the rapid inflow and hydrostatic cooling regimes, and correctly identified the transition mass, suggesting that this be identified this with the characteristic stellar mass of galaxies. Accretion in these two regimes may be expected to result in very different spatial and spec-

tral distributions of cooling radiation, leading to the possibility of observationally distinguishing the two types of accretion (Fardal et al., 2001).[3]

Somewhat ironically, the gas in dark matter halos at the highest redshifts is too cold to cool any further. In halos with virial temperatures below 104 K even shock heated gas (if shocks can occur) will be mostly neutral and therefore unable to coolvia the usual atomic processes. Studies show that the dominant coolant in such cases becomes the small fraction of hydrogen in the form of molecular hydrogen (Abel et al., 1997). Cooling via molecular hydrogen iscrucial for the formation of the first stars (Abel et al., 2002) and galaxies (Bromm et al., 2009) and, therefore, for the sources which cause the reionization of the Universe (Benson et al., 2006; Wise and Abel, 2008a). The details of molecular hydrogen cooling are more complicated than those of atomic cooling: in addition to uncertainties in the molecular chemistry (Glover and Abel, 2008), in many cases equilibrium is not reached and the photon background can lead to both negative (Wise and Abel, 2007a) and positive (Ricotti et al., 2001) feedbacks.

Cosmologically, molecular hydrogen forms via the gas-phase reactions (McDowell, 1961):[3]

$$H + e^- \longrightarrow H^- + \gamma$$

$$H^- + H \longrightarrow H_2 + e^-$$

$$H^+ + H \longrightarrow H_2^+ + \gamma$$

$$H_2^+ + H \longrightarrow H_2 + H^+$$

Dark matter, in contrast, was able to collapse into clouds and then attract normal matter to begin the formation of galaxies, clusters, and superclusters. Mathematical models have been made to describe this process, and cold dark matter does seem capable of jump-starting the formation of structure of the right sizes and in the right amount of time (Figure 2.9). Theorists say that space is filled with tiny, random quantum mechanical fluctuations smaller than the smallest atomic particles. At the moment of inflation, those tiny fluctuations would have been stretched to very large but very subtle variations in gravitational fields that could have stimulated the formation of galaxy super-clusters, filaments, and walls.[1]

Computational Tools

NASA Sky View query form

The Sky View Query Form is a sophisticated and invaluable tool designed for astronomers, researchers, and enthusiasts, providing seamless access to an extensive repository of astronomical images and data from a myriad of sky surveys.One of the

primary features of the Sky View Query Form is its extensive survey selection. Users can choose from a wide array of sky surveys that cover various wavelengths, including optical, infrared, X-ray, and radio. This selection enables multi-wavelength analysis, which is crucial for gaining a comprehensive understanding of astronomical objects and phenomena.Customization is another cornerstone of the Sky View Query Form. Users can specify the size of the image they want to retrieve, typically measured in arcminutes or degrees. File format choices available through the Sky View Query Form cater to diverse needs, ranging from detailed analysis to publication.

Python

Python is a dynamic, high-level programming language that has gained immense popularity across various fields of software development, including web development, data science, artificial intelligence, and more. Created by Guido van Rossum and first released in 1991, Python's design philosophy emphasizes code readability, simplicity, and developer productivity, making it one of the most accessible and versatile languages available today.

Result and Discussion

Image and Temperature Analysis of galaxies

I Have studied 20 galaxies on which recent studies are focused. I have taken their RGB, IOU and ROR images using Sky View Query form. Fits file analysis is done, and temperature analysis is done using their IOU images. The colour dominating in the center of the IOU Image of the galaxy is noted. The temperature of the galaxy is found using **wein's displacement law**.

$$\lambda_m T = b = 2.897 \times 10^{-3} mk \tag{3}$$

Wavelength (λ) is taken as the wavelength of the filter indicating the colour dominating in the center in IOU Image. If Red is dominating ,the filter is WISE 22 , Wavelength is 22 μm, and the temperature is 131.68 K, it is in the spectral class M indicating presence of Red stars . If Green is dominating in the center, the filter is DSS2 Red, wavelength is 6.741 $\times 10^{-7}$ m, and the temperature is 4297 K . If Blue is dominating in the center in IOU Image, the filter is GALEX Near UV, Wavelength is 1350Å - 2800Å, and the temperature is 10,346 K - 21,459 K .
For Example: **NGC4406**

Figure 1. fits file Image,RGB image and IOU image of NGC4406

NGC 4406, also known as Messier 86 (M86), is a lenticular galaxy located in the constellation Virgo. It is part of the Virgo Cluster, a massive cluster of galaxies located approximately 52 million light-years away from Earth . NGC 4406 is one of the largest and brightest galaxies in the Virgo Cluster. It has a relatively smooth and featureless appearance compared to some other galaxies, owing to its lack of prominent spiral arms or significant ongoing star formation activity. Instead, it consists mostly of older stars and contains a bright central bulge surrounded by a disk of stars. The galaxy also exhibits a prominent dust lane across its nucleus, indicative of past interactions or mergers with other galaxies.[5]

In the Infrared Optical Ultraviolet (IOU) image, green colour is dominating in the middle region.While we calculating the temperature of this region using the wavelength of DSS2 Red filter ,it is 4297 K, which is in the spectral class K,which indicates a Yellow-Orange galaxy. Studying yellow-orange galaxies yields valuable information about the formation, evolution, interactions, and large-scale structure of galaxies.

Relationship between Gravitational Redshift and Formation Redshift

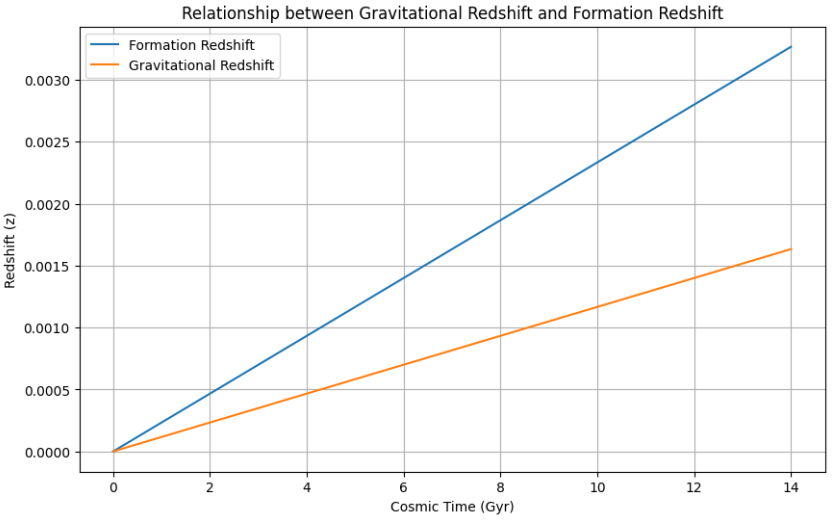

Figure 2. Relationship between Gravitational Redshift and Formation Redshift

0.1 Plot of Gravitational Redshift vs Stellar Counts

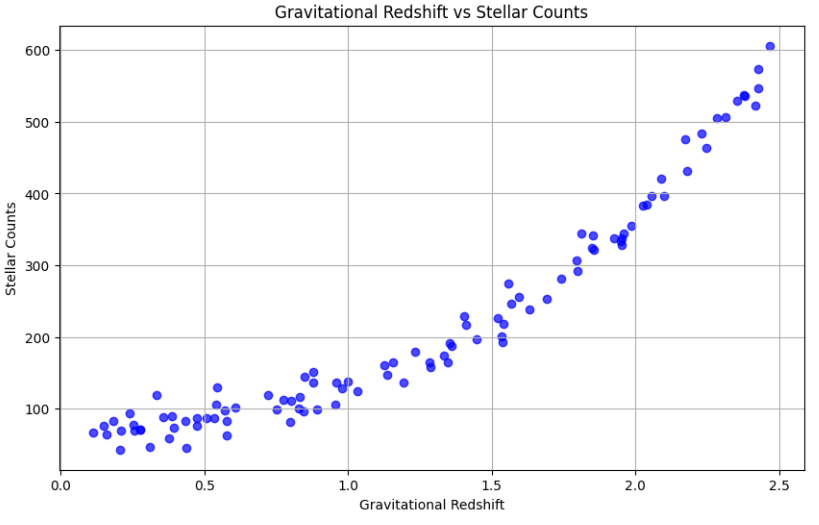

Figure 3. Plot of Gravitational Redshift vs Stellar Counts

Conclusion

In this project, I analyzed the formation and evolution of galaxies using computational tools and images from NASA's SkyView. I focused on galaxies dominated by K-type stars, which provide insights into older stellar populations, chemical composition, and galactic dynamics. Brightest pixel analysis revealed key galactic

features, while mean image data fitting enhanced image quality and consistency. I studied the relationship between gravitational redshift and formation redshift, offering insights into galaxy evolution and cosmology. Additionally, I created plots of gravitational redshift versus stellar counts to understand mass distribution and dark matter presence. Computational tools were crucial, enabling simulations and detailed analysis beyond observational limits, advancing our understanding of galaxy formation and evolution.**mo2010galaxy**

Acknowledgement

I gratefully acknowledge the use of NASA's Sky View tool, which provided invaluable data and resources for this research.

References

[1] M.A. Seeds and D. Backman. Foundations of Astronomy. Cengage Learning, 2015.

[2] H. Mo, F. van den Bosch, and S. White. Galaxy Formation and Evolution. Galaxy Formation and Evolution. Cambridge University Press, 2010

[3] Benson, A. J. (2010). Galaxy formation theory. Physics Reports, 495(2-3), 33-86.

[4] Naab, T., Ostriker, J. P. (2017). Theoretical challenges in galaxy formation. Annual review of astronomy and astrophysics, 55, 59-109.

[5] Rhode, K. L., Zepf, S. E. (2004). The globular cluster systems of the early-type galaxies NGC 3379, NGC 4406, and NGC 4594 and implications for galaxy formation. The Astronomical Journal, 127(1), 302.

Physics Research Reports (2024), **3–1**, 1–10

PHYSICAL SCIENCE RESEARCH RESULTS

HIGHER ORDER SOLITON AND SOLITON PERIOD

MUNEEB K[1] and Sharafali A[*,2]

[1]Department of Physics, Sullamussalam Science College, Areekode, Kerala, India 673639
[2]Department of Physics, Sullamussalam Science College, Areekode, Kerala, India 673639
[*]Corresponding author. Email: sharaf.saj@sscollege.ac.in

Abstract

Photonic Crystal Fiber (PCF) is a type of optical fiber that uses a photonic crystal structure to guide light. Unlike traditional optical fibers, which rely on a difference in refractive index between the core and the cladding, PCFs use a periodic array of microscopic air holes running along the length of the fiber to manipulate light.

Keywords: photonic crystal fiber,Higher order soliton,soliton period

Introduction

Photonics refers to the science and technology of generating, controlling, and detecting photons, which are particles of light. It encompasses a broad range of applications where light plays a crucial role, including telecommunications, medicine, manufacturing, and information technology. In telecommunications, photonics plays a vital role in transmitting and processing information through optical fibers. Optical fibers are thin strands of glass or plastic that guide light pulses over long distances with minimal loss of signal strength. Compared to traditional electrical transmission, optical fibers offer higher bandwidth, faster data transmission rates, and immunity to electromagnetic interference. Photonics enables the development of advanced optical components and systems for telecommunications, such as lasers, modulators, detectors, and amplifiers, which are essential for building efficient and

reliable optical communication networks. The field continues to innovate with advancements like photonic integrated circuits (PICs), which integrate multiple optical functions on a single chip, promising even greater efficiency and scalability in future telecommunications infrastructure. 1.1Optical fiber Optical fiber is a thin, flexible strand of glass or plastic that is used to transmit light signals over long distances. It consists of a core, which carries the light signal, surrounded by a cladding layer that reflects light back into the core through total internal reflection. This structure allows optical fibers to transmit data with extremely low loss over vast distances, making them essential in modern telecommunications and networking. The core of an optical fiber is typically made of high-purity silica glass, although other materials like plastic or compound semiconductors can also be used. Light signals, typically in the form of laser or LED pulses, travel down the core of the fiber. The cladding layer, which has a lower refractive index than the core, ensures that the light signals remain trapped within the core through total internal reflection, minimizing signal loss.

1.2 Structure of optical fiber Optical fiber is made up of three concentric layers, the below figure shows the structure of optical fiber [2] • Core • Cladding • Buffer

Fiber optics is a technology used as a communication medium that works under that works by sending optical signals down hair-thin strands of extremely pure glass or plastic fiber. The light guiding central region is called" Core". The core is surrounded by "cladding" that traps the light in the core using an optical technique called "total internal reflection." The fiber itself is coated by a" buffer" as it is made to protect the fiber from moisture and physical damage. The core and cladding of most fibers are made of ultra-pure glass, although some fibers are all plastic or a glass core and plastic cladding. The core is designed to have a higher index of refraction, an optical parameter that is a measure of the speed of light in the material, than the cladding, which causes" total internal reflection" to trap light in the core up to a certain angle, which defines the "numerical aperture" of the fiber. The core is made up of glass or plastic. Cladding is the substance that is covered over the core of the optical fibre. It has a lower refractive index while compared to the core of the fibre. The cladding of the optical fibre is made up of glass or plastic. The cable offers protection as it contains fibers and strength components within a shield known as a" jacket." 1.3 classification of optical fibre optical fibres are classified in to two categories based on number of modes and refractive index

1.31On the basis of refractive index Single-mode Fiber In single-mode fiber, only the space ray can propagate along the fiber. These fiber consist of a very small core and a high cladding, and the difference between refractive index of core and cladding is very small. the figure 1.2 showing the structure of single mode fiber [3]. Multi-mode Fiber In multi-mode optical fibre, it permits multiple modes for the light ray to pass through. Cladding (70m) and core (40m in general) It has higher relative refractive index difference than single mode fiber. The information goes

in, but some of it has been lost in multimode dispersion. Since it has big dispersion and strong attenuation of the signal at high frequencies, it is not able to be used for long distance communication locations. The figure showing the multimode fiber is shown in the figure 1.2[3].

Figure 1.2: Single-mode and multi-mode optical fiber 1.32 On the basis of refractive index Step-Index Fibre Step index means sharp step in the index of refraction between core and cladding interface. This indicates that in step index, core and cladding have their own constant index of refractions n1 and n2 respectively. The incident light propagates with same speed at the input, so it takes different time to reach the output of the fiber. It results in modal dispersion. Graded-Index Fibre It is another type of optical fiber in which the refractive index of the core is non-uniform. This non-uniformity is present because the refractive index is higher at the axis of the core and continuously reduces with the radial movement away from the axis.

1.3 Photonic Crystal Fiber A photonic crystal fiber (also called holey fiber, hole-assisted fiber, microstructure fiber, or micro-structured fiber) is an optical fiber which obtains its wave-guide properties not from a spatially varying glass composition but from an arrangement of very tiny and closely spaced air holes which go through the whole length of fiber. Such air holes can be obtained by using a preform with (larger) holes, made e.g. by stacking capillary or solid tubes (stacked tube technique) and inserting them into a larger tube. The desire for photonic crystal fibers (PCF) with small mode areas that can be used in nonlinear optics and optical communications is a never-ending and a continuously evolving research quest. By deliberately varying the diameters of air-holes and spacing between holes, a PCF with possible application in optical communications and nonlinear optics is proposed. The zero-dispersion wavelength (ZDW) is easily tailored to be located around 1.55μm. A design of a PCF with high nonlinearity, reduced dispersion and reduced loss due to improper confinement of mode is investigated[5]. Photonic crystal fibers (PCFs) are mainly divided into two categories based on their guiding principles – index guiding and photonic bandgap guiding. Indexguiding PCF has a solid core and a microstructured cladding, and its guiding mechanism is similar to conventional fiber where light is guided based on total internal reflection. The microstructure in the cladding provides a much higher effective index contrast between the core and cladding, such that a stronger confinement of light results. For the photonic bandgap fiber, since the guiding mechanism is by a bandgap structure, the light can be confined in a lower-index core, or even a hollow core filled with air. A solid-core photonic crystal fiber is a fiber with a silica background and air-holes periodically placed in the cladding area. The core is designed to have a high refractive index relative to the cladding and light rays are guided along the fiber the same way they are guided in conventional fibers, through a modified total internal reflection phenomenon . This arrangement, allows the design of a PCF

to exhibit better properties, than a conventional optical fiber. These properties are, endless single mode operation, controllable dispersion characteristics and high nonlinear coefficient . Such properties allow the PCF to be used as fiber lasers, optical amplifiers, super continuum generation, all-optical wavelength conversion, etc. One of the crucial properties for PCFs is high nonlinearity which is much higher than the one exhibited by conventional fibers. For this project we chose hollow-core Photonic crystal fiber. Highly nonlinear PCF is usually based on index-guiding fiber and can be made to have a very small core , which helps to increase the optical intensity within the fiber core, enhancing the effective nonlinearity of the fiber. PCFs provide a great deal of flexibility in terms of dispersion, nonlinearity and attenuation.Generally undoped silica is used as the background material and air voids along the length of the fiber provides the low index region. More Complex materials like Barium Zinc Borate glass can also be incorporated into PCF.Photonic crystal fibers can also be classified as two with respect to Index value. They are high index and low index guiding fibers 1.3.1 High Index Guiding Structure A high-index guiding structure refers to an optical waveguide. The core of a high-index guiding structure typically has a refractive index significantly higher than that of the cladding. This refractive index contrast is crucial because it determines the critical angle at which total internal reflection occurs, confining light within the core. 1.3.2 Low Index Guiding Structure Low index guiding fibers guide light by the Photonic band gap (PBG) effect. The light is confined to the low index core as the PBG effect makes propagation in the micro structured cladding region impossible. In a PBG fiber, the core is created by introducing a defect in the PBG structure, thereby creating an area where the light can propagate. As the light can only propagate at the defect region, allow index guiding core has been created. This is not possible in standard fibers, therefore the low index guiding of PBG fibers opens a new set of possibilities. The structural representation of PCF is shown below In this project we have designed a temperature dependent Photonic Crystal Fibre which is very useful for spectroscopy.

1.3Photonic Crystal Fiber Photonic crystal fiber (PCF) is a type of optical fiber distinguished by its unique micro structured design. Unlike traditional optical fibers, which have a homogeneous core and cladding, PCF features a periodic arrangement of air holes or voids running along its length. These holes create a photonic bandgap structure, allowing PCF to control and manipulate light in novel ways.

One of the key advantages of PCF is its ability to guide light through mechanisms beyond total internal reflection. By adjusting the size, shape, and arrangement of the air holes, PCF can achieve various optical properties such as controlling dispersion, enhancing nonlinear effects, and guiding light in specific wavelengths or modes. This capability makes PCF highly versatile for applications requiring tailored optical characteristics.

PCFs have found numerous applications in areas such as telecommunications,

where they enable efficient and flexible transmission of light signals over long distances with low loss and high bandwidth. They are also used in sensing applications, where their ability to interact with light in a controlled manner enhances sensitivity and specificity in detecting environmental changes or chemical reactions.

Designing of PCF Using COMSOL Multiphysics

(a)Designing of PCF

Photonic crystal fibres have wavelength-scale morphological microstructure running down their length. This structure enables light to be controlled within the fibre in ways not previously possible or even imaginable. Our understanding of what an optical fibre is and what it does is changing because of the development of this new technology, and a broad range of applications based on these principles is being developed. The properties of the PCF have a great dependence on the geometry of the microstructure lattice as well as the choice of the fiber. Designing of PCF for different applications is a crucial step in PCF enabled photonic technologies. For that purpose, we have used commercial stimulation software COMSOL. By using COMSOL we can design the fiber geometry and mode analysis is performed by finite element method (FEM). By using the material option, we can choose the materials inside the PCF and the diameter of the air hole can be varied according to the applicational purpose. The material we have opted here is Barium Zinc Borate glass doped with Praseodymium (BZBP) and silica. Pitch denotes the separation between the centers of two air holes. Open software COMSOL Multiphysics. A window named Model Navigator will be opened. [15] We start by drawing a circle with the radius and the center at desired values. Go to the definition option to get the parameter option, from there we have to enter the pitch and diameter where p is the pitch and d is the diameter. We need to get a circle for an air hole, for that take the geometry option and take circle1. By entering the required radius, sector angle and position, we can make circles as air holes. After entering all required values go to the build selected option and we will get the air hole. To get another air holes we should proceed the same way as explained by changing the (x, y) position. Now we have to insert the materials in the designed photonic crystal fiber. For that select the background where we want to fill, then select material option and add material option. From Geometrical Modeling set physical parameters, Mesh generations, Compute solutions Post processing and visualization. By selecting material content, we can insert the required content like refractive index. In our work, we have taken material 1 as air, material 2 as silica material 3 as BZBP. After entering all the materials, we have to simulate it. We then initialize the mesh for more accuracy. Refine mesh In the Solver Parameters dialog box, set the parameter Search for effective mode indices around to some value. This guarantees that the solver will find the fundamental mode, which has the largest effective mode index.

2.2 Group Velocity Dispersion Optical fiber communication system has great

advantages over the conventional cable communication system. The main advantage of optical fiber is that, it has a large bandwidth so it can carry wide range of signals compared to the conventional cables. Even though there exist some limitations to the distance over which the information can be conveyed without any distortion. The inevitable distortion is due to the optical phenomena called dispersion. It actually limits the transmission capacity of the system. These dispersion causes the spreading of the pulse passing through a cable. Dispersion can be classified into two, one due to Intramodal dispersion and other is due to Intermodal dispersion. Modal dispersion occurs only in Multimode fibers and it contain many different light modes. In each mode ray travels a different distance as it propagates. They arrive at different times at the fiber output. Material dispersion also known as chromatic dispersion, arises due to the variation of refractive index of the core of the fiber as a function of wavelength. Waveguide dispersion is only important in single mode fibers. It is caused by the fact that some light travels in the fiber cladding compared to most light travels through the core, since cladding has lower refractive index than core and the light ray travels faster than that in the core. The group velocity can be defined as the velocity at which the energy in a pulse travel in a fiber. That is . Which is also known as the velocity of the envelope wave. As the signal propagate along the fiber, each spectral component can be assumed to travel independently and to undergo a time delay per unit length. The total delay difference over a distance L is given by . This means that pulse gets spread out as it moves along the fiber, because different component waves which constitutes the pulse have different phase velocities. This phenomenon is known as Group velocity dispersion. We can introduce the mode propagation This wavelength is called zero dispersion wavelength D. For < D, > 0 the fiber is said to exhibit normal dispersion, while for > D the Fiber is said to exhibit anomalous dispersion. In the normal dispersion regime, the high frequency components (blue shifted) of an optical pulse travel slower than the low frequency components (red shifted). The opposite occurs in the anomalous regime. The anomalous regime plays an important role in nonlinear Fiber optics, in particular, for the formation of Supercontinuum effects due to phenomena like Soliton Fission and Modulation Instability.

Result and Discussion

Dispersion Variation For silica From the table.1 we plot the dispersion variation with wavelength from -20ps/nm/km to 100ps/nm/km. We observe from figure 3.1 that the dispersion is negative for d1 denoted by the blue line. A negative dispersion value indicates normal dispersion regime. But for d2 represented by the green line the curve extends to the positive dispersion region after a wavelength of around 1.55μm. The properties of PCFs are highly dependent on its structure and material composition. We shall vary its structure according to the application purposes. As discussed, typically silica is used as the core and cladding with air holes which effectively

decreases the refractive index of the cladding. I have experimented by replacing the PCF core filled with Barium Zinc Borate glass doped with Praseodymium (BZBP), with cladding as air itself with diameter 0.6 (blue in color) and the material was silica, pitch is 2.2.

We have solved the nonlinear Schrodinger equation from equation (2.16). So firstly, i have experimented by replacing the PCF core filled silica, with cladding as air itself with diameter 0.6 (red in color) and the material was silica, pitch is 2.2.but there i got dispersion curve as negative which means it is normal dispersion similarly with diameter 0.8 (red in color) from the wavelength 1nm to 1.8 nm in the temperature 25◦ C as shown in figure 3.1

explained in the above section. Now we solve the nonlinear Schrodinger equation for each diameter and plot power versus wavelength graphs and Intensity plots. For that we set some initial preliminary values to optimize the output generation. From our dispersion curves, we have chosen our reference wavelength for d2 to be 1550 nm. The peak input power in watts is chosen to be 1000W which is far lower than a normal laser input. The duration of input pulse is another important parameter denoted by 0=0.35254ps. The most challenging aspect of our proposed PCF is its fibre length. The length has to be chosen with the manufacturing process of a silica filled PCF in mind. We can't carelessly choose a large arbitrary length. Here we have chosen the best suited of length of 0.2m. Using these parameters, we find the Intensity and Output spectral width. The figure 3.5 and figure 3.6 shows the Result plots. Figure 3.3 shows the splitting of the pulse as wave propagates. Near 4.06m of propagation through the PCF the single pulse splits into smaller pulses and it leads to spectral broadening and supercontinuum generation through modulation instability. We can also see the compression of the pulse.

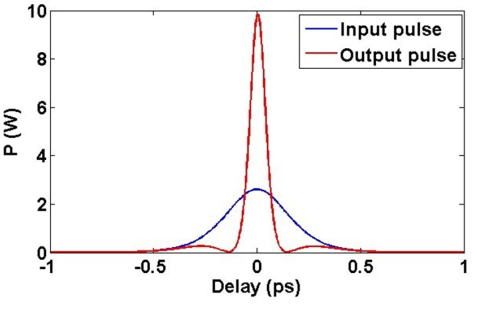

Figure 1. Dispersion variation with wavelength

For BZBP We have solved the nonlinear Schrodinger equation from equation (2.16). We have designed silica based pcf for different diameters as

Similarly, I have tried filling Barium Zinc Borate glass doped with Praseodymium (BZBP) and clad with radius of core as 1.1 and the diameter of clad as 1.4μm(blue)

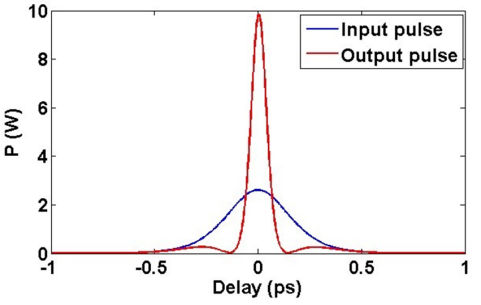

Figure 2. Figure 3.5Pulse propogation in silica

and pitch is 2.2 resulted as normal dispersion) from the wavelength 1nm to 1.8 nm in the temperature 25° C as shown in figure 3.2.

Figure 3.2: dispersion curve for Barium Zinc Borate glass doped with Praseodymium (BZBP) based pcf explained in the above section. Now we solve the nonlinear Schrodinger equation for each diameter and plot power versus wavelength graphs and Intensity plots. For that we set some initial preliminary values to optimize the output generation. From our dispersion curves, we have chosen our reference wavelength for d2 to be 1550 nm. The peak input power in watts is chosen to be 1000W which is far lower than a normal laser input. The duration of input pulse is another important parameter denoted by 0=0.35254ps. The most challenging aspect of our proposed PCF is its fibre length. The length has to be chosen with the manufacturing process of a silica filled PCF in mind. We can't carelessly choose an large arbitrary length. Here we have chosen the best suited of length of 2m. Using these parameters, we find the Intensity and Output spectral width. The figure 4.2and figure 4.3 shows the Result plots. Figure 3.3 shows the splitting of the pulse as wave propagates. Near 0.43m of propagation through the PCF the single pulse splits into smaller pulses and it leads to spectral broadening and supercontinuum generation through modulation instability. We can also see the compression of the pulse.

Conclusion

Through this project I have created Pcf for materials like Barium Zinc Borate glass doped with Praseodymium (BZBP) based photonic crystal fiber and silica. And I have found that comprssion factor is more in silica based pcf than Barium Zinc Borate glass doped with Praseodymium (BZBP) based photonic crystal fiber. But silica based pcf need more power than like Barium Zinc Borate glass doped with Praseodymium (BZBP) based photonic crystal fiber. And also found that silica needs less fiber length (0.2m) but like Barium Zinc Borate glass doped with Praseodymium (BZBP) based photonic crystal fiber needs more fibre length(2m).

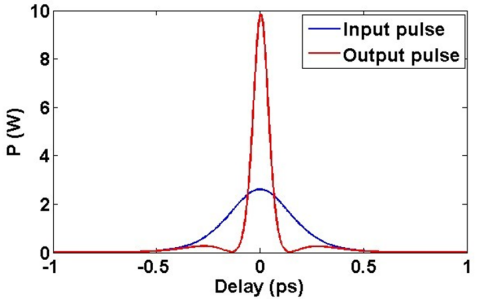

Figure 3. Figure 3.2: dispersion curve for Barium Zinc Borate glass doped with Praseodymium (BZBP) based pcf

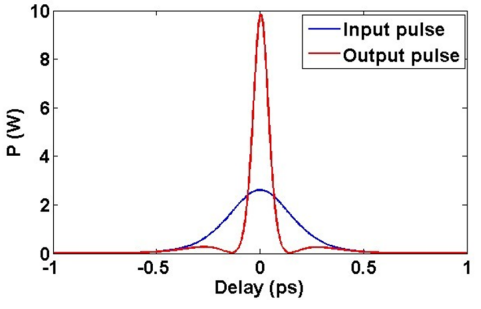

Figure 4. Figure4.2 pulse propogation in Barium Zinc Borate glass doped with Praseodymium (BZBP) based pcf.

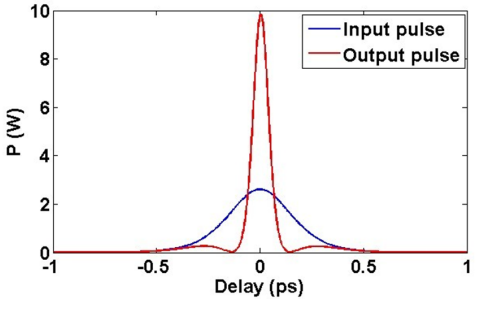

Figure 5. Figure4.3 Power vs delay graph for for silica based pcf

Reference

[1] J. S. Russell, "Report on waves", in Report of the 14th meeting of the British Association for the Advancement of Science, p. 331 (1844)

[2] V. E. Zakharov and A. B. Shabat, "Exact theory of two-dimensional self-focusing and one-dimensional self-modulation of waves in nonlinear media", Sov. Phys. JETP 34, 62 (1972)

[3] A. Hasegawa and F. Tappert, "Transmission of stationary nonlinear optical pulses in dispersive dielectric fibers. I. Anomalous dispersion", Appl. Phys. Lett. 23, 142 (1973); https://doi.org/10.1063/1.1654836

[4] L. F. Mollenauer, R. H. Stolen, and J. P. Gordon, "Experimental observation of picosecond pulse narrowing and solitons in optical fibers", Phys. Rev. Lett. 45 (13), 1095 (1980); https://doi.org/10.1103/PhysRevLett.45.1095

[5] F. M. Mitschke and L. F. Mollenauer, "Discovery of the soliton self-frequency shift", Opt. Lett. 11 (10), 659 (1986); https://doi.org/10.1364/OL.11.000659

[6] J. P. Gordon, "Theory of the soliton self-frequency shift", Opt. Lett. 11 (10), 662 (1986); https://doi.org/10.1364/OL.11.000662

[7] L. F. Mollenauer et al., "Soliton propagation in long fibers with periodically compensated loss", IEEE J. Quantum Electron. 22 (1), 157 (1986); https://doi.org/10.1109/JQE.1

[8] B. A. Malomed and S. Wabnitz, "Soliton annihilation and fusion from resonant inelastic collisions in birefringent optical fibers", Opt. Lett. 16 (18), 1388 (1991); https://doi.org/10.1364/OL.16.001388

[9] N. N. Akhmediev et al., "Stable soliton pairs in optical transmission lines and fiber lasers", J. Opt. Soc. Am. B 15 (2), 515 (1998); https://doi.org/10.1364/JOSAB.15.000515

[10] V. N. Serkin and A. Hasegawa, "Novel soliton solutions of the nonlinear Schrödinger equation model", Phys. Rev. Lett. 85 (21), 4502

[11] X. Liu et al., "Soliton self-frequency shift in a short-tapered air–silica microstructure fiber", Opt. Lett. 26 (6), 358 (2001); https://doi.org/10.1364/OL.26.000358

[12] N. Nishizawa and T. Goto, "Widely wavelength-tunable ultrashort pulse generation using polarization maintaining optical fibers", J. Sel. Top. Quantum Electron. 7 (4), 518 (2001); https://doi.org/10.1109/2944.974222

[13] J. Santhanam and G. P. Agrawal, "Raman-induced spectral shifts in optical fibers: general theory based on the moment method", Opt. Commun. 222, 413 (2003); https://doi.org/10.1016/S0030-4018(03)01561-X

[14] K. S. Abedin and F. Kubota, "Widely tunable femtosecond soliton pulse generation at a 10-GHz repetition rate by use of the soliton self-frequency shift in photonic crystal fiber", Opt. Lett. 28 (19), 1760 (2003); https://doi.org/10.1364/OL.28.001760

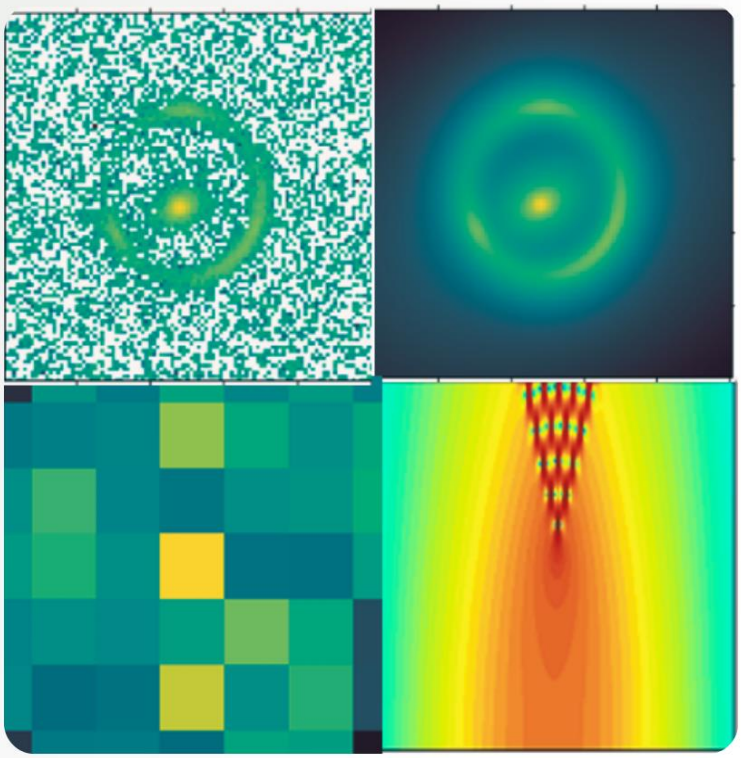

PG DEPARTMENT OF PHYSICS

SULLAMUSSALAM SCIENCE COLLEGE

AREEKODE